

FLOW VISUALIZATION OF CAVITATION

by

JEFFREY WILMS

B.S., Kansas State University, 2009

A THESIS

submitted in partial fulfillment of the requirements for the degree

MASTER OF SCIENCE

Department of Mechanical and Nuclear Engineering  
College of Engineering

KANSAS STATE UNIVERSITY  
Manhattan, Kansas

2013

Approved by:

Major Professor  
Dr. Mohammad Hosni

## **Abstract**

A typical refrigeration loop is composed of an evaporator, compressor, condenser, and an expansion valve. There are many possible refrigerants that can be used, but the physical properties of water make it ineffective in the traditional refrigeration loop. But if water could be used it would have many advantages as it is abundant, cheap, and is safe for the environment. This research focuses on a different kind of refrigeration loop using water. This new refrigeration loop utilizes water flowing through a nozzle, initiating cavitation. Cavitation is generally defined as creating vapor from liquid, not through adding heat, but by decreasing the pressure. In a converging/ diverging nozzle, as the cross sectional area is constricted, the velocity of the flow will increase, decreasing the pressure. Therefore, by flowing water through the nozzle it will cavitate. Transforming liquid into gas requires a certain amount of energy, defined as the latent heat. When a liquid is turned to vapor by an increase in the temperature, the latent heat is provided by the heat transfer to the system. As no energy is being added to the nozzle to cause the cavitation, the energy transfer to create the vapor comes from the remaining liquid, effectively causing a temperature drop.

This research focused on the flow visualization of water cavitating as it travelled through a converging/ diverging nozzle. Under different flow conditions and different nozzle geometries, the cavitation manifested itself in different formations. When gasses were entrained in the water they formed bubbles, which acted as nucleation sites as they moved through the nozzle. This was called travelling bubble cavitation. In venturi nozzles the cavitation nucleated off of the wall, forming attached wall cavitation. When water flowed out of an orifice, a turbulent mixture of liquid and vapor, orifice jet, was formed which caused vapor to form around it. This was known as shear cavitation. When the water was rotated prior to the throat of an orifice, the orifice jet expanded radially and formed swirl cavitation. In addition to studying how the cavitation was formed, the void fraction and velocity were measured for attached wall cavitation.

## Table of Contents

List of Figures .....	vi
List of Tables .....	x
Acknowledgements .....	xi
Dedication .....	xii
Chapter 1 - Introduction .....	1
1.1 Literature Review .....	3
1.2 Research Objectives .....	17
1.2.1 Development of the Measurement Techniques .....	17
1.2.2 Visualization of the Cavitation Phenomena .....	17
1.2.3 Obtaining Quantitative Results .....	17
Chapter 2 - Experimental Setup .....	18
2.1 Water Testing Rig .....	18
2.2 Nozzles .....	19
2.2.1 Initial Plastic Nozzle .....	19
2.2.2 Square Inlet and Curved Inlet Nozzles .....	20
2.2.3 Glass Nozzles .....	22
2.3 Flow Visualization .....	24
2.3.1 High Speed Camera .....	24
2.3.2 Lens .....	25
2.3.3 Lighting .....	25
2.4 Laser Induced Fluorescence .....	26
2.4.1 Yag Laser .....	26
2.4.2 Dye concentration of Rhodamine B in water .....	27
2.5 Computer processing in Matlab Code .....	28
Chapter 3 - Flow Visualization Results .....	30
3.1 Attached Wall Cavitation .....	30
3.1.1 Curved Inlet Acrylic Nozzle .....	31
3.1.2 Sudden Inlet Acrylic Nozzle .....	34

3.1.3 Nozzle 1 and Nozzle 2 .....	34
3.1.4 Nozzle 3 .....	40
3.1.5 Nozzle 4 .....	42
3.2 Shear Cavitation.....	44
3.2.1 Inverse Nozzle 2.....	44
3.2.2 Nozzle 5 .....	46
3.2.3 Nozzle 6 and Nozzle 7 .....	49
3.3 Mixed Cavitation .....	52
3.3.1 Nozzle 8 .....	52
3.3.2 Nozzle 9 .....	54
3.4 Swirl Cavitation .....	56
3.5 Travelling Bubble Cavitation.....	57
Chapter 4 - Quantitative Results of Attached Wall Cavitation.....	61
4.1 Void Fraction Measurements.....	61
4.1.1 Preliminary Testing.....	61
4.1.2 Nozzle 1 .....	65
4.1.3 Nozzle 2 .....	71
4.2 Velocity Measurements .....	74
4.2.1 Preliminary Testing.....	74
4.2.2 Nozzle 1 .....	78
4.2.3 Nozzle 2 .....	80
4.3 Flow Quality .....	81
4.3.1 Nozzle 1 .....	82
4.3.2 Nozzle 2 .....	83
Chapter 5 - Flow Visualization Summary, Conclusion, and Recommendations.....	85
5.1 Summary and Conclusions .....	85
5.2 Recommendations and Future Work .....	86
5.2.1 Cavitation .....	86
5.2.2 Measurement Method .....	87
References.....	88
Appendix A - High Speed Camera .....	89



Appendix B - Matlab Code .....	92
Appendix C - Measurement Instrument Specifications .....	96
Appendix D - Index Matching .....	97

## List of Figures

Figure 1.1 Traditional Refrigeration Cycle [1].	1
Figure 1.2 Refrigeration cycle utilizing a converging/ diverging nozzle [1].	2
Figure 1.3 Four types of Cavitation; (A) Traveling bubble cavitation, (B) Attached wall cavitation, (C) Vortex cavitation, (D) Shear cavitation [2].	4
Figure 1.4 “Microbubble in a liquid”; “Radius of equilibrium of a microbubble as a function of pressure” [2].	5
Figure 1.5 “Visualization of Leading Edge Cavitation in an Inducer of Rocket Engine for the Same Cavitation Number $\sigma_v = .011$ but with Two Different Fluids (nominal flowrate, 5 000 rpm) (courtesy of CNES/SNECMA)” [2].	6
Figure 1.6 (A) Separated laminar boundary layer, (B) Attached wall cavitation, (C) Travelling bubble cavitation, (D) Travelling bubble and attached wall cavitation [2].	7
Figure 1.7 A) “Schematic view of the Venturi profile”; B) “Photograph of the cavity” [3].	8
Figure 1.8 Experimental and predicted measurements in water; A) Void fraction vs. position, Y(m); B) Velocity measurements (m/s) vs. position, Y(m); C) $(P-P_v)/P_v$ vs. x-xi (m) [3].	9
Figure 1.9 Test nozzle of Davis [4].	10
Figure 1.10. Cavitation of water through nozzle, with the bottom image a close up [4].	10
Figure 1.11 Measurements of pressure and void fraction for water through nozzle [4].	11
Figure 1.12 Three different types of observed cavitation [5].	12
Figure 1.13 “CAD drawing of flow patterns” [6].	13
Figure 1.14 On top, cavitation in a channel leading into a wide orifice on bottom. From left to right, low flow to higher flow conditions [7].	14
Figure 1.15 Swirl cavitation flowing into a radial pump [8].	15
Figure 1.16 “Comparison of SEM (scanning electron microscopy) images of the patterned Al plates after ultrasonic treatment at 340K (on the top) and 293 K (on the bottom): (a,d) at 5 min of sonication, (b,e) at 30 min of sonication, (c,f) high magnification of the hydrophobic surface with pits at 30 min of sonication” [9].	16
Figure 2.1: Water testing rig.	18
Figure 2.2 The water loop setup. On the left there is the water tank, filters, pumps, and heaters. On the right is the test section.	19

Figure 2.3: Initial plastic nozzle.....	19
Figure 2.4: Initial plastic nozzle design (dimensions are in millimeters). ....	20
Figure 2.5: Images of cavitation in initial nozzle with strobe light. ....	20
Figure 2.6: Square Inlet (left) and Curved Inlet (right) Nozzles.....	21
Figure 2.7: Design of Square and Curved Inlet Nozzles (dimensions are in millimeters). ....	21
Figure 2.8: Nozzle 1, with Rhodamine B dye.....	22
Figure 2.9: Experimental set up with the high speed camera. ....	24
Figure 2.10 Specifications of the Infinity K-2 lens.....	25
Figure 2.11 Setup of the laser system. ....	27
Figure 2.12 Laser illuminated images on 3 millimeters tubes with air bubbles. ....	28
Figure 2.13 Process for calculating void fraction. ....	29
Figure 3.1 Curved Inlet Nozzle visualization. ....	32
Figure 3.2 Initiation of cavitation, left image 40.3 gram/s, right image 50.1 gram/s ....	33
Figure 3.3 End of cavitation distances.....	33
Figure 3.4 Square Inlet Nozzle visualization.....	34
Figure 3.5 Design of Nozzle 1 and Nozzle 2 .....	35
Figure 3.6 Nozzle 1, (A, B) 30 °C; (C, D) 30 °C Laser Induced Cavitation .....	36
Figure 3.7 Nozzle 1, sequence with frame numbers.....	37
Figure 3.8 Nozzle 1, sequence continued from Figure 3.7. ....	37
Figure 3.9 Nozzle 1, (A) 40C, (B) 50C.....	38
Figure 3.10 Nozzle 2, (A,B) With Scratch; (C, D) No scratch. ....	39
Figure 3.11 Nozzle 2, (A) 20 g/s, (B) 22 g/s, (C) 29 g/s.....	40
Figure 3.12 Design of Nozzle 3 .....	41
Figure 3.13 Nozzle 3 visualization. ....	41
Figure 3.14 Nozzle 4 visualization. ....	42
Figure 3.15 Nozzle 4 visualization, zoomed in.....	43
Figure 3.16 Inverse Nozzle 2 sequence with frame numbers. ....	45
Figure 3.17 Inverse Nozzle 2 PLIF.....	46
Figure 3.18 Design of Nozzle 5 .....	47
Figure 3.19 Nozzle 5 sequence with frame number. ....	48
Figure 3.20 Nozzle 5 PLIF images. ....	49

Figure 3.21 Design of Nozzle 6 and Nozzle 7. ....	50
Figure 3.22 Nozzle 6, gradual expansion flow visualization. ....	50
Figure 3.23 Nozzle 6, rapid expansion flow visualization. ....	51
Figure 3.24 Nozzle 7, gradual expansion flow visualization. ....	51
Figure 3.25 Nozzle 7, rapid expansion flow visualization. ....	51
Figure 3.26 Design of Nozzle 8. ....	53
Figure 3.27 Nozzle 8 flow visualization, (A,B,C) diffuse light; (D,E,F) PLIF. ....	53
Figure 3.28 Nozzle 8 with IFM, (A,B,C) diffuse light; (D,E,F) PLIF. ....	53
Figure 3.29 Nozzle 9 sequence with frame numbers. ....	55
Figure 3.30 Nozzle 5 with IFM, (A,B), diffuse light; (C,D), PLIF. ....	56
Figure 3.31 Nozzle 2 travelling bubble sequence with frame numbers. ....	58
Figure 3.32 Nozzle 2 travelling bubble sequence and wall cavitation with frame numbers. ....	59
Figure 3.33 Chart of the position of the bubble with flow image. ....	60
Figure 3.34 Chart of the velocity of the bubbles. Velocities averaged over 20 frames. ....	60
Figure 4.1 Laser orientation. ....	62
Figure 4.2 Nozzle 1, varying threshold images. ....	63
Figure 4.3 Nozzle 1, Void Fraction- 100 Threshold. ....	64
Figure 4.4 Nozzle 1, Void Fraction- Varying Threshold. ....	64
Figure 4.5 (A) Original Image, (B) Red Component, (C) Green Component, (D) Blue Component. ....	65
Figure 4.6 (A) Pure Gas, (B) Pure Liquid, (C) Cavitation, (D) Cavitation with sections. ....	65
Figure 4.7 Nozzle 1, image set 1, void fraction, Laser Induced Cavitation. ....	66
Figure 4.8 Void fraction measurements for image set 1. ....	67
Figure 4.9 Nozzle 1, Side view showing 45° angle light sheet; (A) side view of entire nozzle; (B,C,D), images with cavitation for void fraction; (E), no flow image. ....	67
Figure 4.10 Nozzle 1, void fraction of image set 1 and 45° angle light sheet. ....	68
Figure 4.11 Nozzle 1, Laser Induced Cavitation, Image Set 2. ....	68
Figure 4.12 Nozzle 1, 40° C, Image Set 2. ....	69
Figure 4.13 Nozzle 1, Image Set 1 and 2, Void Fraction. ....	69
Figure 4.14 Nozzle 1, Digital Camera, (A) Air, (B) liquid, (C,D) 40 °C, (E) 50 °C. ....	70
Figure 4.15 Nozzle 1, void fraction, results of green component and image set 2. ....	70

Figure 4.16 Nozzle 2, 48 g/s, 30 °C.....	71
Figure 4.17 Nozzle 2, 85 g/s, 30 °C.....	72
Figure 4.18 Nozzle 2, 95 g/s, 30 °C.....	72
Figure 4.19 Nozzle 2, 84 g/s, 50 °C.....	73
Figure 4.20 Nozzle 2, void fraction results.....	74
Figure 4.21 Nozzle 1; PLIF; 70,000 frames / second .....	76
Figure 4.22 Correlation coefficients of images from Figure 4.21. ....	76
Figure 4.23 (A) Cropped Images, (B) Correlation graph.....	77
Figure 4.24 (A) Further Cropped Images, (B) Correlation graph.....	77
Figure 4.25 Nozzle 1, Laser Induced Cavitation Vapor Velocity.....	78
Figure 4.26 Nozzle 1, 30 °C, PLIF .....	79
Figure 4.27 Nozzle 1, 30 °C Vapor Velocity.....	79
Figure 4.28 Nozzle 1, 40 °C Vapor Velocity.....	80
Figure 4.29 Nozzle 1, Combined Vapor Velocities.....	80
Figure 4.30 Nozzle 2, Combined Vapor Velocities.....	81
Figure 4.31 Nozzle 1, Flow Quality Results.....	83
Figure 4.32 Nozzle 2, Flow Quality Results.....	84
Figure D.1 Index Matching fluids. These images have a pyrex rod inside of a cylinder. Top Row, Left: Air; Top Row, Right: Water; Middle Row, Left: Vegetable Oil; Middle Row, Right: Baby Oil; Bottom Row: 200ml vegetable oil, 150ml baby oil. ....	98
Figure D.2 Containment for the fluid. ....	99

## **List of Tables**

Table 1 Glass Nozzle Designs .....	23
Table 2 Flow and visualization data for 3.1 Attached Wall Cavitation.....	31
Table 3 Flow and visualization data for 3.2 Shear Cavitation.....	44
Table 4 Flow and visualization data for 3.3 Mixed Cavitation.....	52
Table 5 Flow and visualization data for 3.4 Swirl Cavitation. ....	56
Table 6 Flow and visualization data for 3.5 Travelling Bubble Cavitation.....	57
Table 7 Testing Sets for Void Fraction and Velocity .....	61
Table 8 Flow Conditions for Nozzle 1.....	66
Table 9 Flow Conditions for Nozzle 2.....	71

## **Acknowledgements**

I would like to thank my family for being with me while I completed this thesis. Thanks to Dr. Beck, who guided me in the technical applications of this research. Thanks to Dr. Hosni, who gave me the motivation and the encouragement when I needed it. Thanks to Dr. Sorensen, who, being a Physics professor, provided a second way of approaching problems. Thanks to Don Tomasi, who provided the organization and the push that kept the project going. Thanks to Jim Hodgson, the KSU glassblower, who translated what I wanted into workable nozzles. Thanks to Weixin Zhao for his help with the Matlab code for finding velocity.

## **Dedication**

There is only one person that I could ever consider dedicating this thesis to: my dad, Richard N Wilms. He was the one who encouraged me to get my Masters and he supported me along the way, but he is no longer around. After an initial fight with cancer he had a few years with no signs of it returning. Then, during the summer of 2011 the first signs of its return were noticed. He spent that fall, winter, and spring going through 5 rounds of chemotherapy to fight the cancer. Initially, after the last round of chemotherapy, his health started to improve. Things were looking up. However, this initial success only made the bad news worse as the cancer came back. There would be no chemotherapy this time, the war was lost and fighting it could only buy a few more pain filled months. But, with this news my Dad still fought on, this time not to extend his life, but to help his family as much as he could while he was still on earth. But eventually his time was up, surrounded by his wife, his daughter and her husband, his mother, and me. While his last breath was on December 15<sup>th</sup>, 2012, he will always be with us all in one way or another.

And so I dedicate this to my dad. I would give the earth, the moon, or the stars to be able to call you right now and tell you this thesis is finished. I would give all I have to just have been able to complete it and have you read it before you passed away. But I know that even if I cannot talk to you about it anymore you are proud of me. I cannot focus on what I cannot have, but I must focus on the dream you had for your children: the dream to live a successful, comfortable, and happy life. And with this thesis I am one step closer to this dream.



## Chapter 1 - Introduction

A traditional refrigeration cycle uses a compressor to increase the pressure and temperature of a fluid. The condenser primarily lowers the temperature, as heat is transferred to the environment. Then, the fluid goes through an expansion valve, lowering the pressure and therefore the temperature. Finally, the fluid goes through an evaporator, taking in heat from its surroundings. Figure 1.1 shows the refrigeration cycle used in the patent that led to this research, where the working fluid is tetraflouroethane ( $\text{CH}_2\text{FCf}_3$ ), referred to as R-134. In this cycle the coefficient of performance is 2.4 [1].

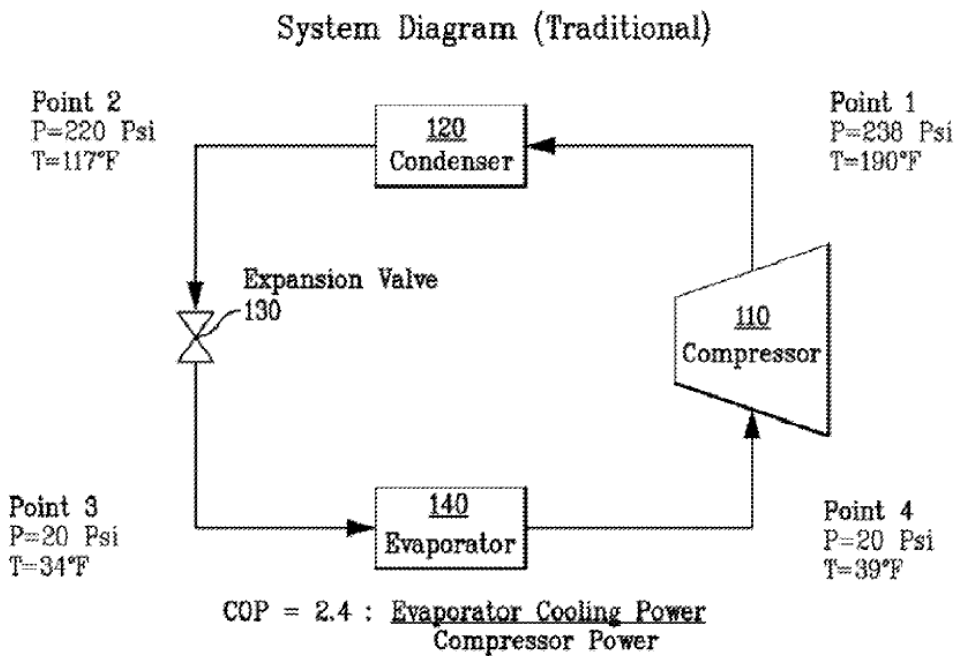


**Figure 1.1 Traditional Refrigeration Cycle [1].**

The research in this thesis is part of the work conducted by a larger group investigating the possibility of making an improved refrigeration cycle. Improving the cycle is defined in one of two ways: (1) increasing the coefficient of performance, and (2) utilizing water as a refrigerant. The advantage of increasing the coefficient is cheaper operating costs. The advantage of water is that it is cheap, abundant, and leaks from the system will not harm the environment. Instead of trying to improve the conventional vapor-compression cycle this project utilizes an alternate method of cooling. The concept from the patent is shown in Figure 1.2, and features a

converging/ diverging nozzle. In the initial concept, the fluid is driven by a piston at the top of the nozzle, although later iterations have a pump driving the fluid through the nozzle [1]. From the fluid dynamics in a nozzle, as the flow is constricted the fluid velocity increases. Then, according to Bernoulli's principle, as the velocity increases, the pressure decreases. The fluid going into the nozzle is liquid, and when the pressure decreases to the vapor pressure some of the liquid turns to vapor. This process is called cavitation and it can cause a decrease in temperature in the fluid. The overall goal of this project is to use this temperature decrease to absorb heat from the surroundings, similar to the evaporator in a traditional refrigeration cycle. The research detailed in this thesis focused on visualizing the flow of the cavitation through various nozzles. As a baseline for cavitation refrigeration development, the visualization of many different nozzles was investigated. Some of these nozzles were further analyzed by measuring the velocity and void fraction of the cavitation.

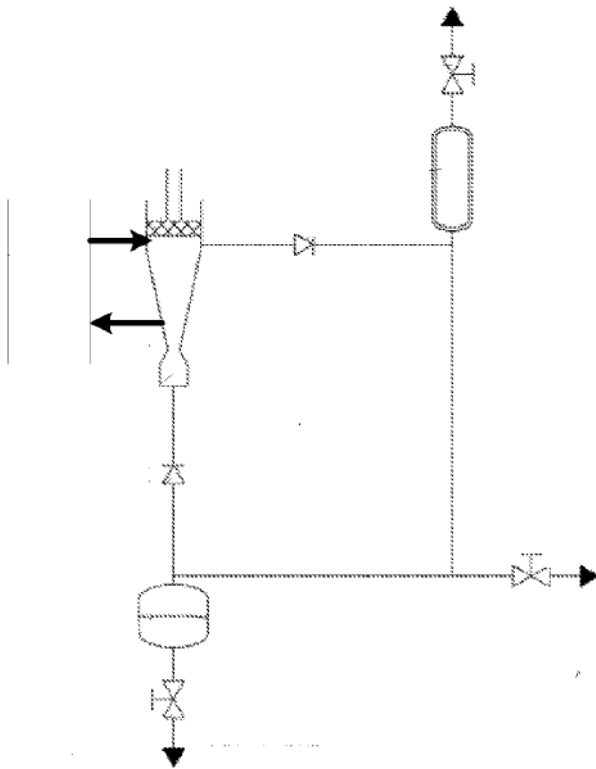


**Figure 1.2 Refrigeration cycle utilizing a converging/ diverging nozzle [1].**

## 1.1 Literature Review

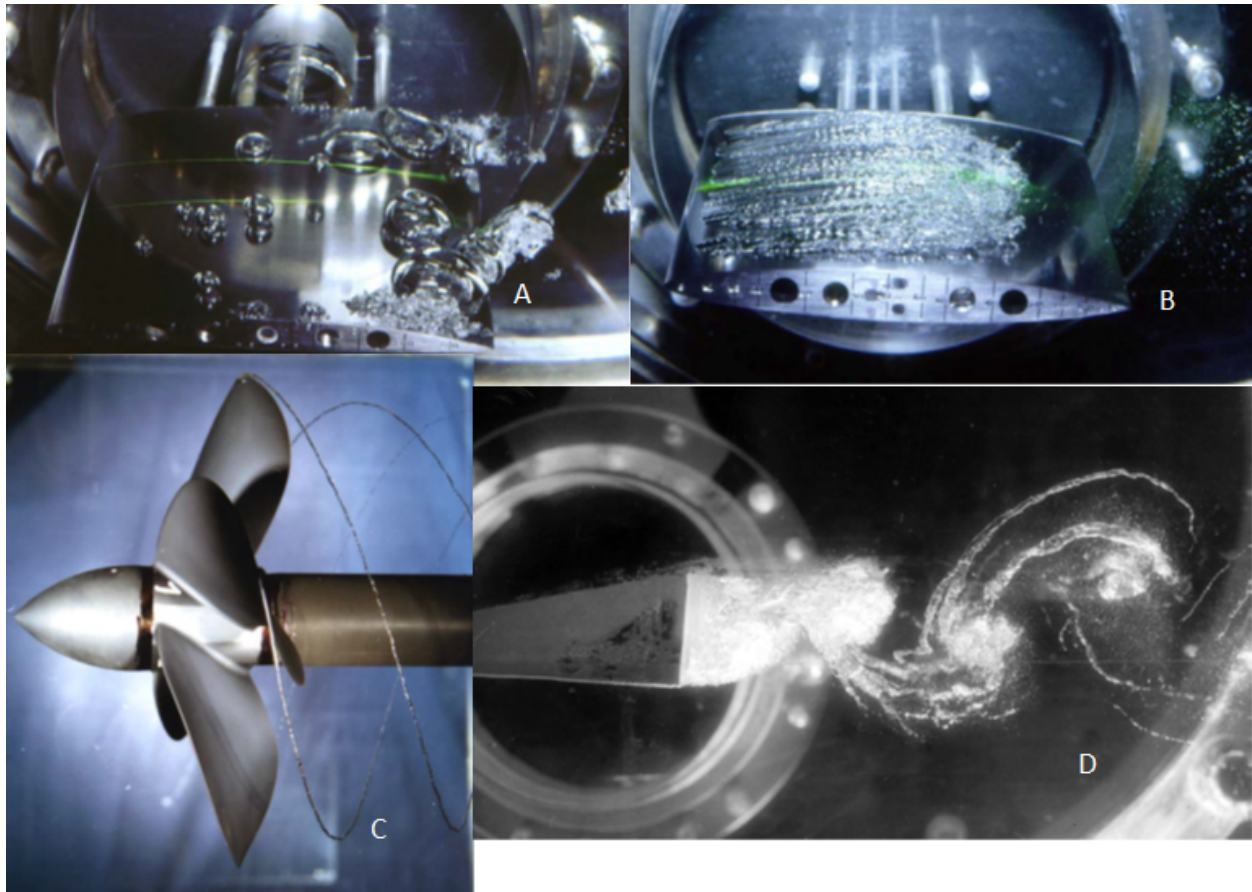
Jean-Pierre Franc published an extremely inclusive paper detailing cavitation titled “Physics and Control of Cavitation” in *Design and Analysis of High Speed Pumps* [2]. In this paper he focused on cavitation as it occurred on a hydrofoil. He goes in depth about how the cavitation is formed, the different formations of cavitation, non-dimensionalized formulas of cavitation, an analysis of cavitation nuclei and its effect on the cavitation, the thermal effects in cavitation, and also the effects of the boundary layer and nuclei content on the cavitation patterns. Cavitation is described as the process of turning a liquid into a gas, not through increasing the temperature, but by decreasing the pressure. With moving flow, this decrease in pressure is facilitated by the Bernoulli equation. In incipient cavitation, it can be predicted that the Bernoulli’s equation is still valid. However, in developed cavitation Bernoulli’s equation starts to break down as the pressure stays close to the vapor pressure, even while the velocity is increased [2].

Figure 1.3 shows the four types of cavitation as described by Franc: travelling bubble, attached, vortex, and shear cavitation [2]. In the travelling bubble cavitation, weak points in the liquid, nuclei, grow from being almost invisible microscopic bubbles to being macroscopic bubbles when the pressure drops below the vapor pressure. Once the bubbles reach a region of sufficient pressure they explosively collapse. Attached cavitation is composed of cavities that are attached to the wall in a quasi permanent manner. The attached cavitation shows variations in the flow pattern, with most of the fluctuations occurring near the end of the cavitation region. In vortex cavitation the pressure difference between the pressure side and the suction side results in a secondary flow going around the tip, which generates a vortex attached to the tip. The last form of cavitation, shear cavitation, gets its name from the shear layers of cavitation that form from an obstruction in the flow, or around submerged jets. The core of the submerged jet forms a core of low pressure where the cavitation will appear first. A non-dimensional cavitation number is defined by Franc [2]:

$$\sigma_v = \frac{p_{ref} - p_v}{\frac{1}{2}\rho V_{ref}^2} \quad (1.1)$$

In this equation  $p_{ref}$  and  $V_{ref}$  are the reference values for the pressure and velocity in the flow, with  $p_v$  being the vapor pressure and  $\rho$  being the density. The lower the cavitation number, the

higher the probability of cavitation developing. However, due to a hysteresis effect, the cavitation will vanish at a critical cavitation number higher than the inception cavitation number. In theory all cavitation will behave the same at similar cavitation numbers, although there may be some second-order differences [2].



**Figure 1.3 Four types of Cavitation; (A) Traveling bubble cavitation, (B) Attached wall cavitation, (C) Vortex cavitation, (D) Shear cavitation [2].**

Traveling bubble cavitation is spurred on by the presence of nuclei in the water. These nuclei contain non-condensable gasses, such as oxygen and nitrogen, as well as the vapor from the fluid. Figure 1.4 [2], from Franc, shows the diagram of a microbubble in a liquid. The variables  $p_g$  and  $p_v$  are the partial pressures of the gas and vapor,  $p_\infty$  is the pressure of the liquid outside,  $S$  is the surface tension, and  $R$  is the radius. The graph shows that as the outside pressure decreases, the radius of the bubble will slightly increase. Once a critical pressure has been achieved the bubble is now at a critical bubble size. Once the bubble reaches this critical size the outside pressure must increase for the bubble to remain in equilibrium. While this pressure is increased the bubble size will continue to increase. If the pressure ever drops below the critical

pressure, or if it drops below the equilibrium line once the bubble has achieved its critical radius, the bubble will grow destabilized and become a macrobubble. The difference between the pressure of vaporization and the critical pressure is a result of the surface tension [2].

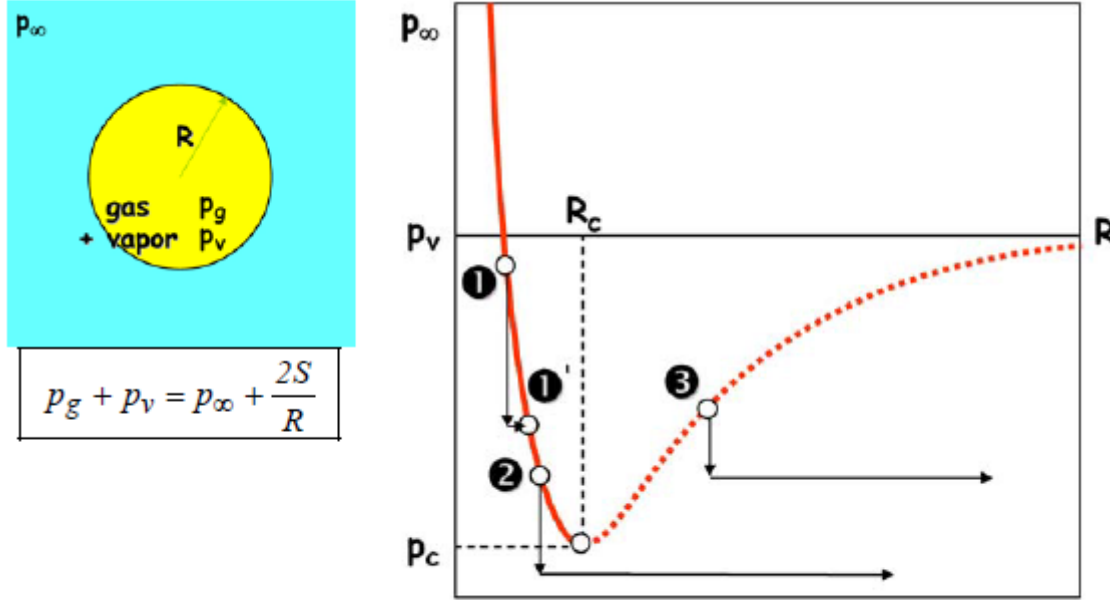


**Figure 1.4 “Microbubble in a liquid”; “Radius of equilibrium of a microbubble as a function of pressure” [2].**

During cavitation there is a change in temperature that is highly dependent on the properties of the fluid [2]. This change in temperature is due to the latent heat, the energy required to transform liquid into a vapor. In adiabatic cavitation this energy is assumed to be supplied by the liquid surrounding the vapor. The energy from vaporization is equal to the product of the vapor density, vapor volume, and the latent heat. Equation (1.2) [2] is an estimate of the temperature drop, based on the assumption that the volume of vapor will equal the volume of liquid; where  $\rho$  is the density of the vapor or liquid,  $L$  is latent heat, and  $c$  is the specific heat in the liquid.

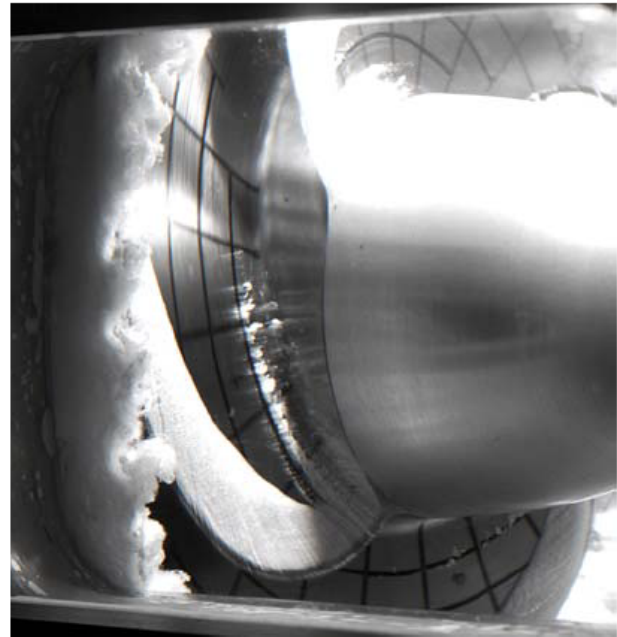
$$\Delta T^* = \frac{\rho_v L}{\rho_\ell c_{p\ell}} \quad (1.2)$$

This temperature drop is 0.01 for water at 20°C, 1.25 for Liquid Hydrogen at 22.2 K, and 2.0 for Refrigerant 114 at 40°C [2]. Figure 1.5, provided to Franc from CNES/SNECMA [2], shows the cavitation with similar cavitation numbers for water and Refrigerant 114. The cavitation forms in

the water, where the thermal effects are low. With Refrigerant 114 the temperature drop suppresses the formation of cavitation. It is suppressed due to the temperature drop lowering the vaporization pressure, which leads to a larger local cavitation number. The temperature drop has a direct relationship to the latent heat of vaporization, and an inverse relationship to the ratio of the liquid density to vapor density and the convective heat transfer coefficient [2].



**Without thermal effect  
(water at room temperature,  
 $\Delta T^* = 0.01 K$ )**



**With thermal effects  
(Refrigerant 114 at 40°C,  
 $\Delta T^* = 2.0 K$ )**

**Figure 1.5 “Visualization of Leading Edge Cavitation in an Inducer of Rocket Engine for the Same Cavitation Number  $\sigma_v = .011$  but with Two Different Fluids (nominal flowrate, 5 000 rpm) (courtesy of CNES/SNECMA)” [2].**

There are two main variables that affect cavitation, the nuclei content and the boundary layer flow. Figure 1.6, from Franc [2], shows how these variables can affect cavitation. In these images, deaerated water flowed over the hydrofoil, with a nuclei injection device adding engassed water where desired. In image A the separated laminar boundary layer is shown on a hydrofoil with a 0 degree attack angle. In the rear part of the hydrofoil an adverse pressure gradient forces a separation point. In image B the flow is run with a low nuclei count. This causes attached wall cavitation to form at the region where the flow separates from the wall. In image C the flow is run with a large nuclei count. The nuclei form travelling bubble cavitation,



which then disrupts and prevents the attached wall cavitation. In image D nuclei are concentrated further into the page. This creates two forms of cavitation, attached wall cavitation out of the page, and travelling bubble cavitation into the page [2].

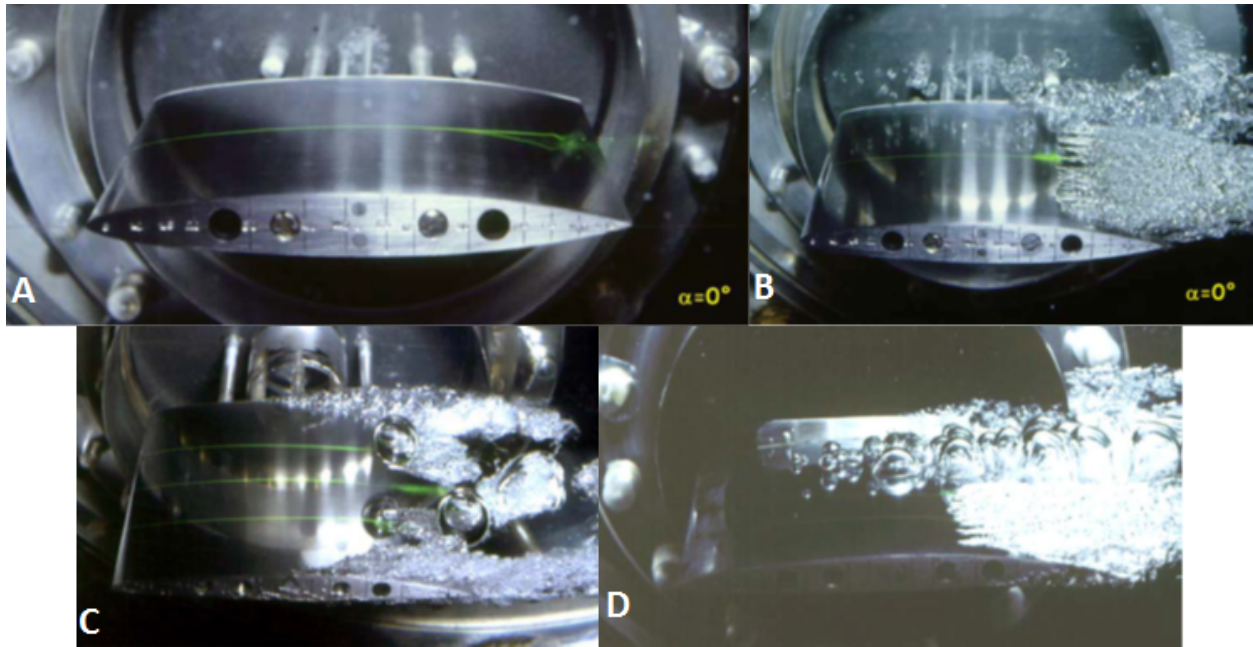


**Figure 1.6 (A) Separated laminar boundary layer, (B) Attached wall cavitation, (C) Travelling bubble cavitation, (D) Travelling bubble and attached wall cavitation [2].**

Goncalves and Patella [3] developed mathematical models to predict the cavitation in a venturi type test section that “was designed to simulate cavitating flows developing on the blades of space turbo-pump inducers.” Figure 1.7 A shows their test setup, where the cross sectional area of the throat is  $43.7 \times 44 \text{ mm}^2$ . The length of the test section was 252 mm apart and the five probing holes measure the void fraction, instantaneous local speed, and the wall pressure. In this journal article they predicted and measured water, which had low thermal effects. Figure 1.7 B shows an image taken of the cavitation. This cavitation was labeled an “attached cavitation sheet” [3], similar to the “attached wall cavitation” by Franc [2]. The results of their experimental and predicted values for water are shown in Figure 1.8. The measurements at station 1 and 2 showed that the void fraction was largest at the wall, the velocity increased further from the wall, and the predicted values were close to the measured values. In stations 3-5 a recirculation region developed. This recirculation caused low values of void fraction near the wall, negative velocities, and introduced differences between the predicted and measured values. Figure 1.7 C shows the wall pressure profile, where the five stations are the first five

experimental data points. When the vapor was attached to the wall, the pressure in the fluid was equal to the vapor pressure. Once the recirculation region developed the pressure started to rise [3].

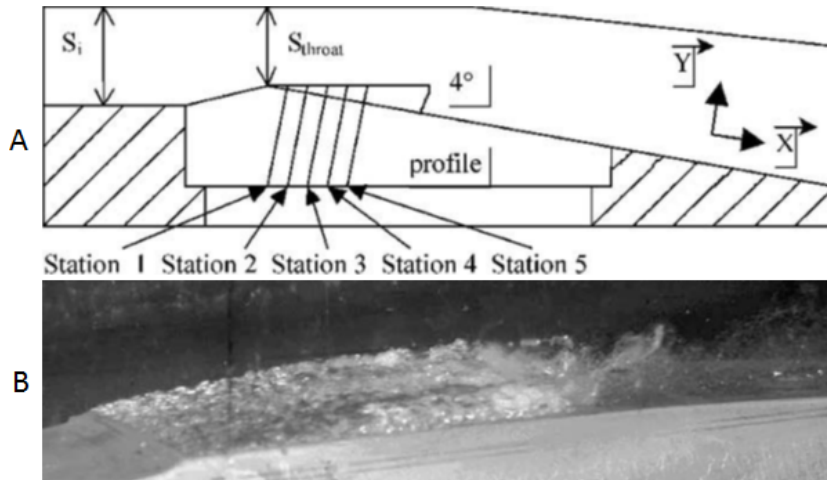


**Figure 1.7 A) “Schematic view of the Venturi profile”; B) “Photograph of the cavity” [3].**

In the research by Michael P. Davis [4], a two dimensional nozzle venturi was used. This nozzle design, shown in Figure 1.9, was formed between two walls 1.58 mm apart, with the throat area  $2.5 \text{ mm}^2$ . A blow down system was used to induce flow. The upstream tank was at atmospheric pressure while the downstream tank varied the pressure from 60 to 15 kPa. Figure 1.10 shows the visualization of the cavitating water in the nozzle when the downstream pressure was 20 kPa. The void fraction measurements are plotted on Figure 1.11, with the pressure to show the “strong correlation between the two” [4]. As the pressure decreased, bubbles started to form. There was a rapid increase in the void fraction starting at  $x/L = 0.2$ , and at  $x/L = 0.25$  the void fraction leveled out to 0.8. At  $x/L = 0.45$  there was an abrupt region of bubble collapse, quickly lowering the void fraction to 0.05.



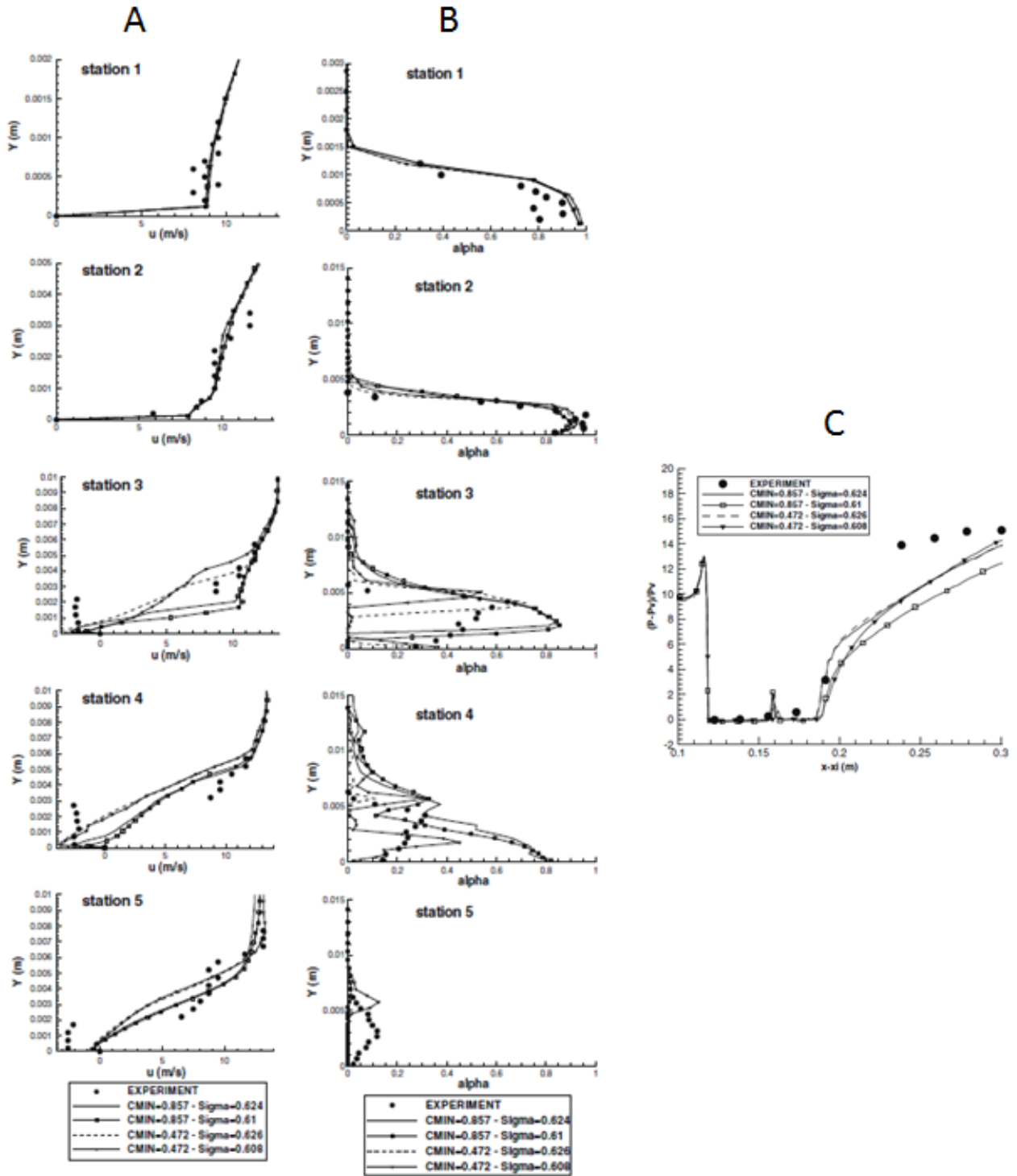
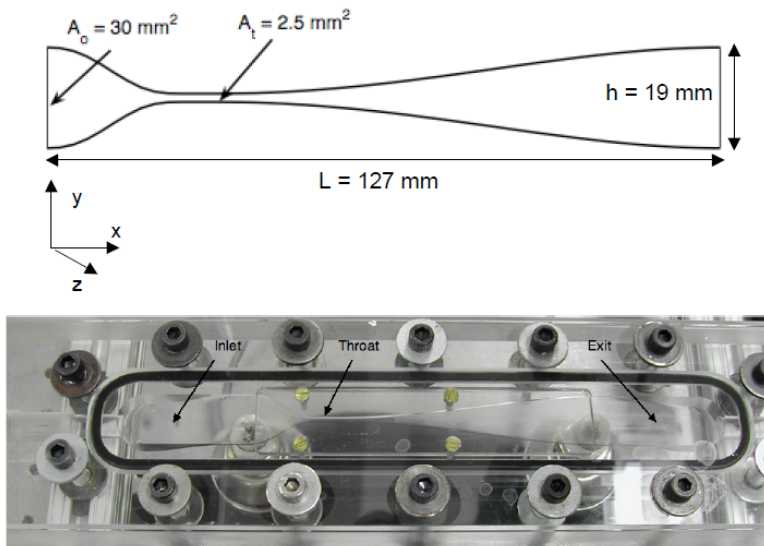
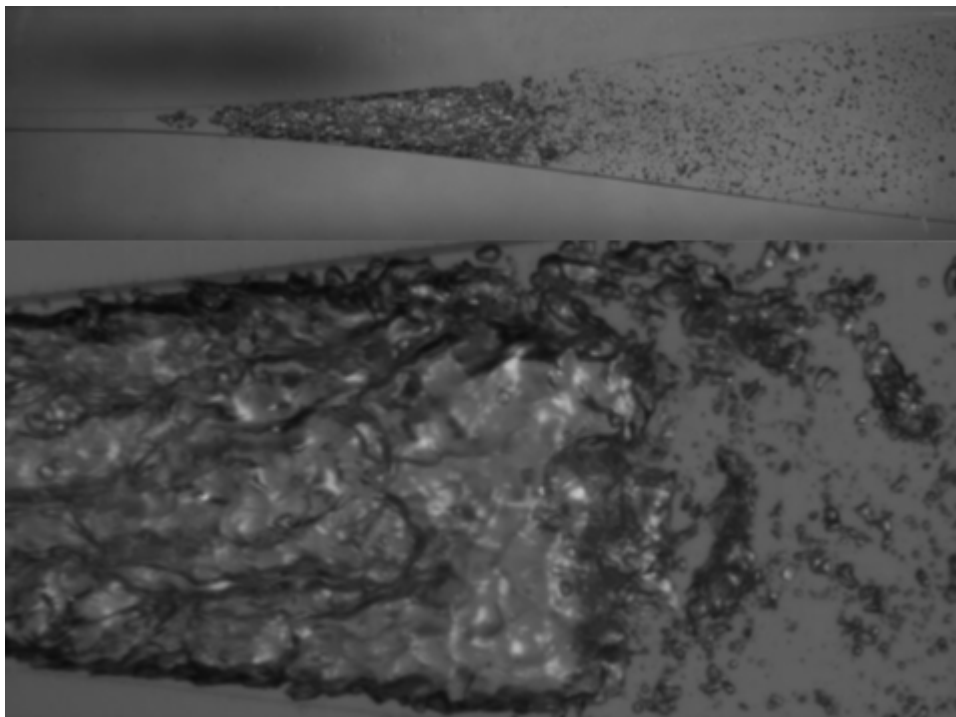


Figure 1.8 Experimental and predicted measurements in water; A) Void fraction vs. position,  $Y(m)$ ; B) Velocity measurements (m/s) vs. position,  $Y(m)$ ; C)  $(P-Pv)/Pv$  vs.  $x-xi(m)$  [3].



**Figure 1.9 Test nozzle of Davis [4].**



**Figure 1.10. Cavitation of water through nozzle, with the bottom image a close up [4].**

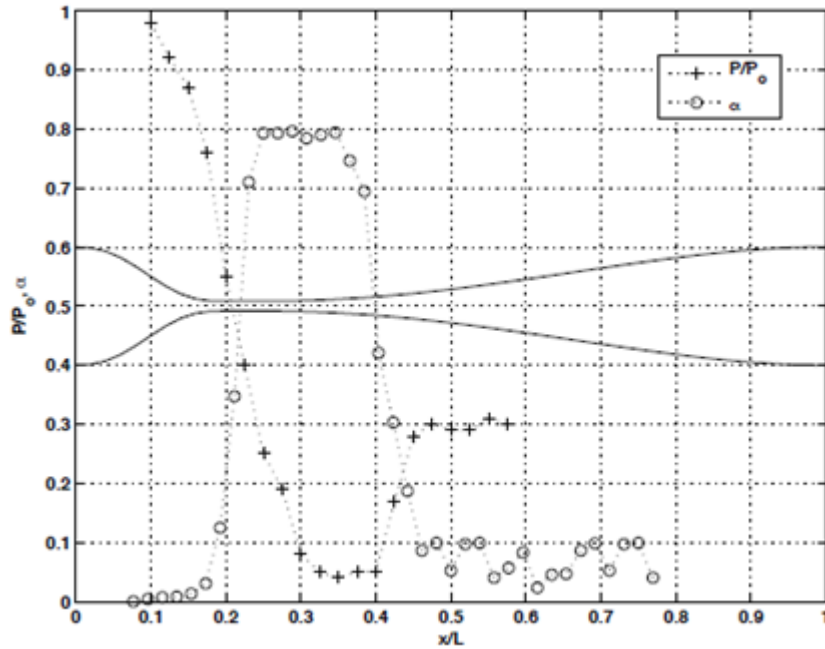


**Figure 1.11 Measurements of pressure and void fraction for water through nozzle [4].**

In a study by Sato, Hachino, and Saito [5], a glass venturi nozzle with a throat diameter of 10 mm and an exit diameter of 40 mm was used. A pump was used to flow water through the nozzle. In this study they found that there were three different forms of cavitation, as shown in Figure 1.12: traveling bubble cavitation, transition-type cavitation, and sheet cavitation. The traveling bubble cavitation was observed to have a spherical bubble characteristic that formed slightly downstream of the throat, and then at around 40 mm downstream of the throat the bubble collapsed [5]. The transition type cavitation was similar to the traveling bubble cavitation; however, as the bubble travelled downstream, cavitation remained upstream of the bubble. In the sheet cavitation the vapor nucleated around 10mm of the minimum throat area off of the wall. From the wall the vapor spread into the middle of the nozzle [5].

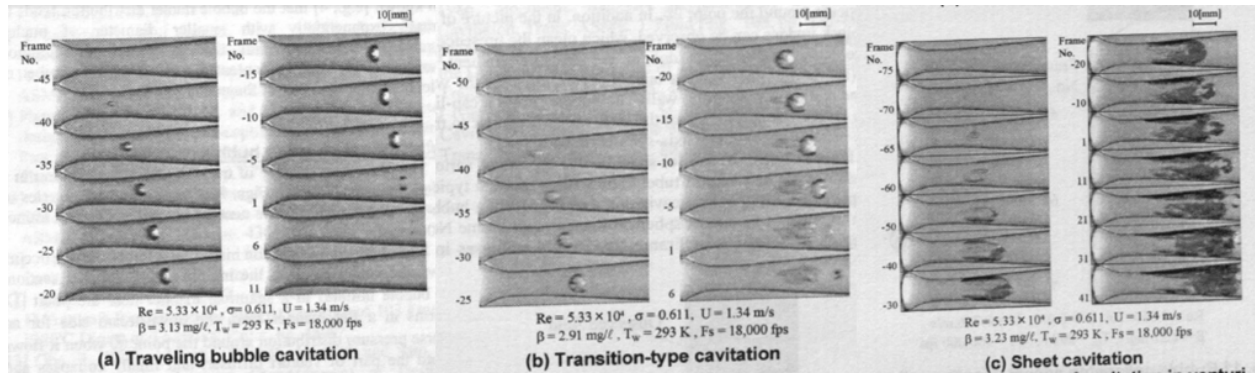
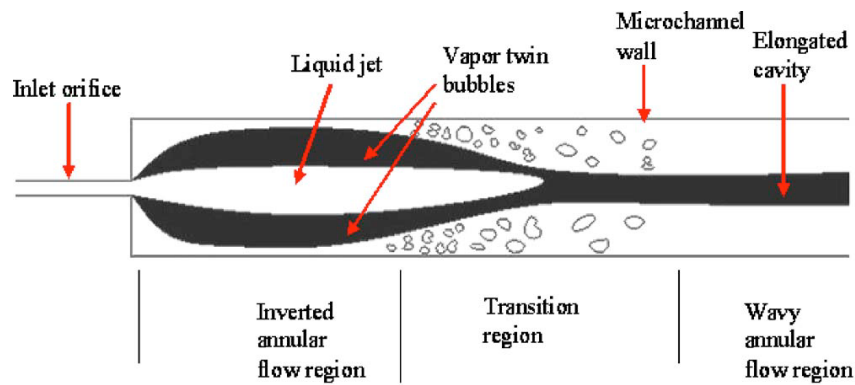
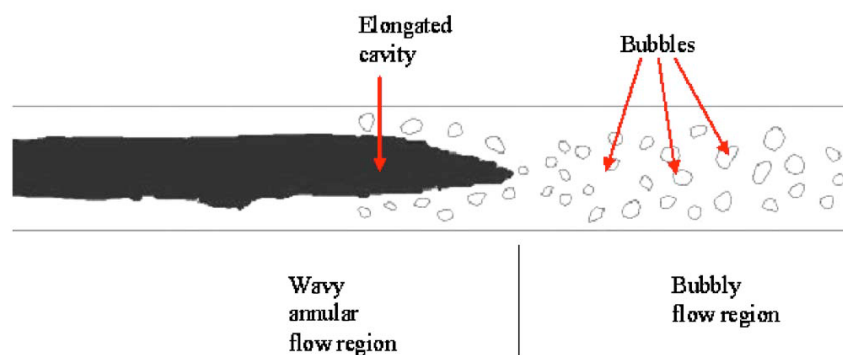


**Figure 1.12 Three different types of observed cavitation [5].**

Research by Schneider, Kosar, Kuo, Mishra, Cole, Scaringe, and Peles [6] studied the heat transfer effects of water traveling through five microchannels. These microchannels had an orifice, a 20  $\mu\text{m}$  channel flowing into a 200  $\mu\text{m}$  channel. They created a CAD drawing of the observed flow patterns at adiabatic conditions, as shown in Figure 1.13. Out of the orifice, a liquid jet formed, with twin vapor bubbles surrounding it, and liquid surrounding the vapor bubbles. In the transition region “the flow became unstable, rapid shedding of vapor slugs were detected, and the void fraction was strongly time dependent” [6]. In the wavy annular flow the vapor formed into a solitary vapor bubble that eventually broke up into smaller channels before exiting the channels. They found that cavitating flow conditions increased the rate of heat transfer by approximately 67% over noncavitating flow conditions.



(a) Microchannel inlet



(b) Collapse of elongated bubble

**Figure 1.13 “CAD drawing of flow patterns” [6].**

Research has also been done to examine the effects of cavitation in the nozzles of pressure atomizers by Sou, Hosokawa, and Tomyama [7]. The experimental setup was a pump driving water through a 4mm wide channel into a 32mm wide channel. Figure 1.14 shows the flow visualization. At low flow conditions there was no cavitation. At higher flow settings the cavitation started to develop, and then broke down, leaving no effect on the spray at the orifice. With a larger flow, the cavitation developed down most of the channel, which created a wide spray. At the final stage, the cavitation only formed on one side of the nozzle, which induced the spray to only occur on the opposite side of the cavitation [7].

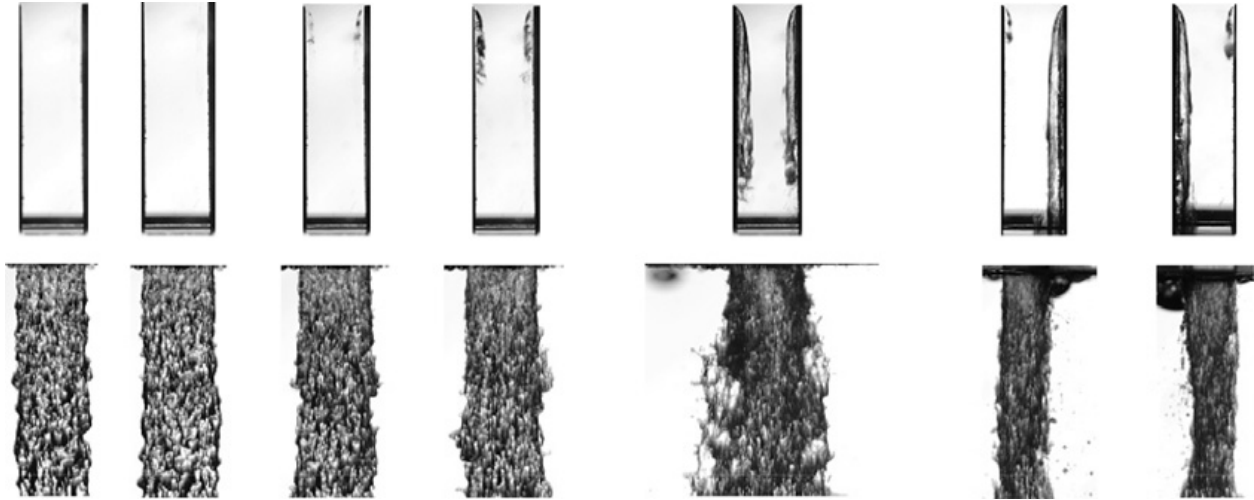


**Figure 1.14 On top, cavitation in a channel leading into a wide orifice on bottom. From left to right, low flow to higher flow conditions [7].**

Predin and Bilus [8] numerically and experimentally analyzed the effect of water rotating as it flowed into a radial pump. As shown in Figure 1.15, the rotating flow created vapor, referred to as swirl cavitation. They varied the pump operating speed as well as the pressure in the inlet water tank. It was observed that neither the pump speed nor the tank pressure had any effect on the length of the cavitation; it was “a function of the pump impeller eye geometry” [8]. By decreasing the tank pressure, the diameter of the swirl cavitation decreased.

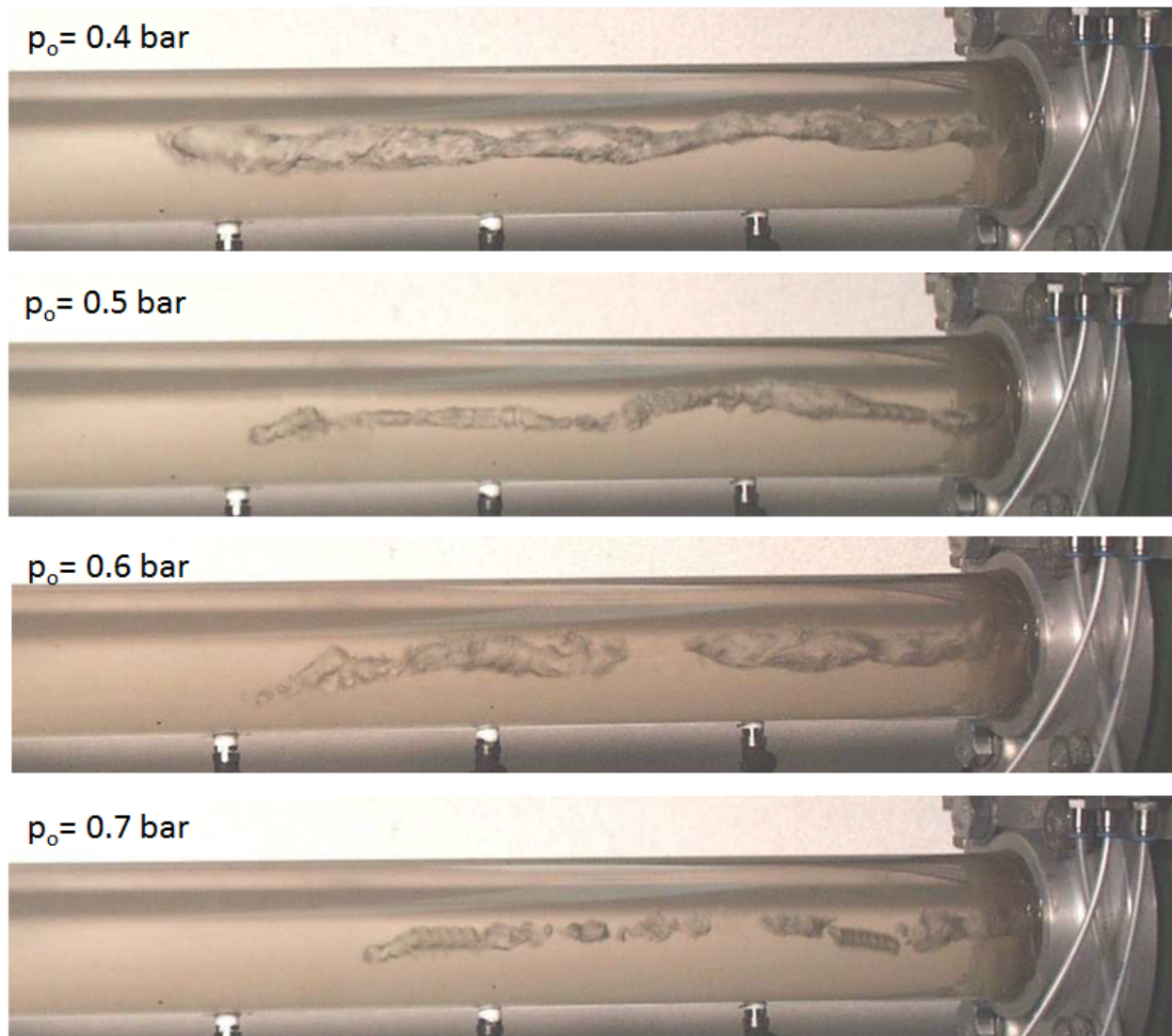


**Figure 1.15 Swirl cavitation flowing into a radial pump [8].**

All of the forms of cavitation described above were hydrodynamic cavitation. Belova, Gorin, Shchukin, and Mohwald [9] conducted research by inducing vapor through ultrasonic waves, defined as acoustic cavitation. Their research used octadecylphosphonic acid and octadecanethiol on an aluminum surface. These acids etched a hydrophobic surface on the aluminum next to unaffected aluminum that was hydrophilic. Figure 1.16 shows the effect of using different temperatures on the different surfaces. In these images, the right side is the hydrophilic surface; whereas the left side is hydrophobic. The author found that at 340 K the hydrophobic surfaces induced a greater number of cavitation sites. At 293 K there were fewer cavitation sites; however, they still occurred more often in the hydrophobic surfaces [9].



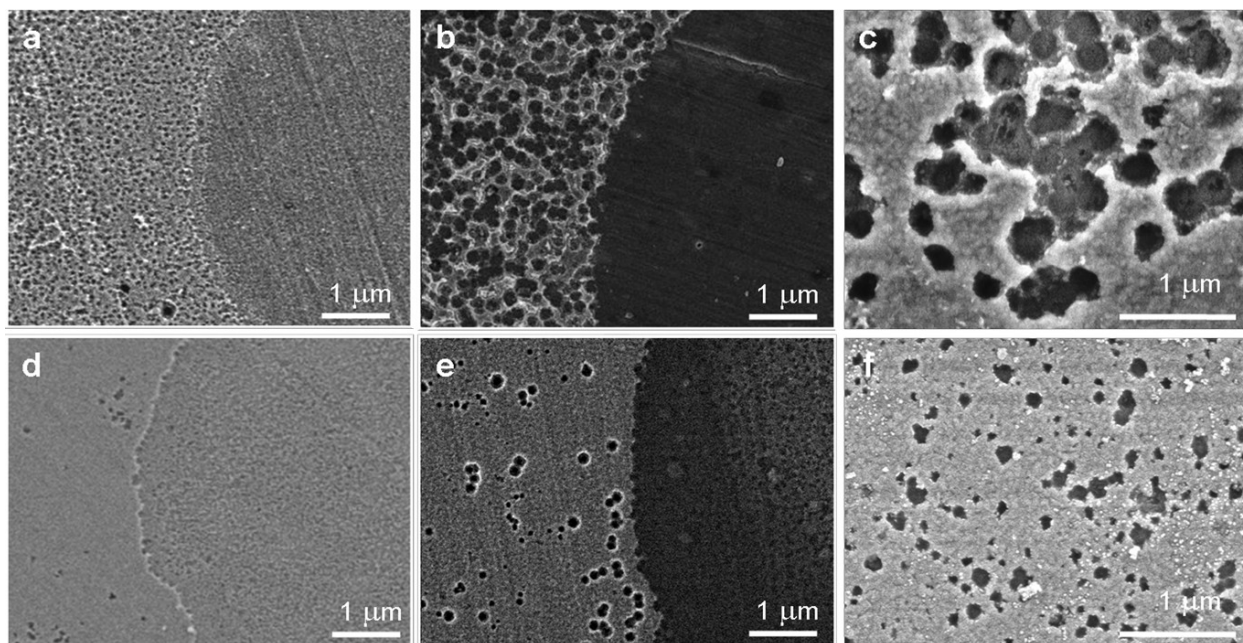


**Figure 1.16 “Comparison of SEM (scanning electron microscopy) images of the patterned Al plates after ultrasonic treatment at 340K (on the top) and 293 K (on the bottom): (a,d) at 5 min of sonication, (b,e) at 30 min of sonication, (c,f) high magnification of the hydrophobic surface with pits at 30 min of sonication” [9].**



## **1.2 Research Objectives**

### ***1.2.1 Development of the Measurement Techniques***

The first objective was to develop the techniques to measure the cavitation. This was started by constructing a water testing rig to induce cavitation, which used a centrifugal pump to flow water through a clear nozzle. Once cavitation was induced, it was necessary to develop a method for visualizing the flow. The velocity of the fluid going through the nozzle was around 30 meters per second. With a nozzle length of 50 millimeters, the fluid took around 1.6 milliseconds to get from the beginning to the end. Therefore, a standard video camera, running at 30 frames per second, was not suitable for these flows. A high speed camera, as well as new lenses and lighting, was needed to ensure quality images. Planer Laser Induced Fluorescence (PLIF) was used to obtain quantitative measurement, which required the use of a Yag laser.

### ***1.2.2 Visualization of the Cavitation Phenomena***

As shown in the literature search, cavitation can appear in several different forms: attached wall, shear, swirl, and travelling bubble cavitation. Many nozzles of varying geometries were developed and then categorized by their form of cavitation. Through this categorization, empirical predictions of the cavitation can be made based on nozzle geometry.

### ***1.2.3 Obtaining Quantitative Results***

In order to predict the potential for cooling in the cavitating water, the flow quality had to be measured. The more vapor is generated the more heat is transferred from the liquid; therefore a significant flow quality would indicate that a measurable temperature drop could occur. In order to measure the flow quality, the void fraction and vapor velocity measurements were recorded in the glass venturi nozzles. The effects of temperature and the mass flow rate on the flow quality were measured.

## Chapter 2 - Experimental Setup

### 2.1 Water Testing Rig

A diagram of the water testing rig is shown in Figure 2.1, with the images of the rig in Figure 2.2. A large water tank held the majority of the fluid in the water loop. The primary loop was the driving loop that pushed the fluid that was being studied through the nozzle. The fluid was driven by a centrifugal pump, model T51 made by MTH Pumps. The fluid then traveled through an electric heater. It was then filtered by a Shelco Micro Gaurdian filter. It then traveled through a reverse osmosis device. The mass flow, inlet pressure (P1), and inlet temperature (T1) were then measured. The fluid then flowed through the nozzle and then returned to the water tank. The secondary loop was utilized in order to regulate the temperature of the fluid. The fluid in the secondary loop was driven by another centrifugal pump. The heat exchanger cooled the fluid with tap water. The fluid was then sent through a heater and returned to the water tank.

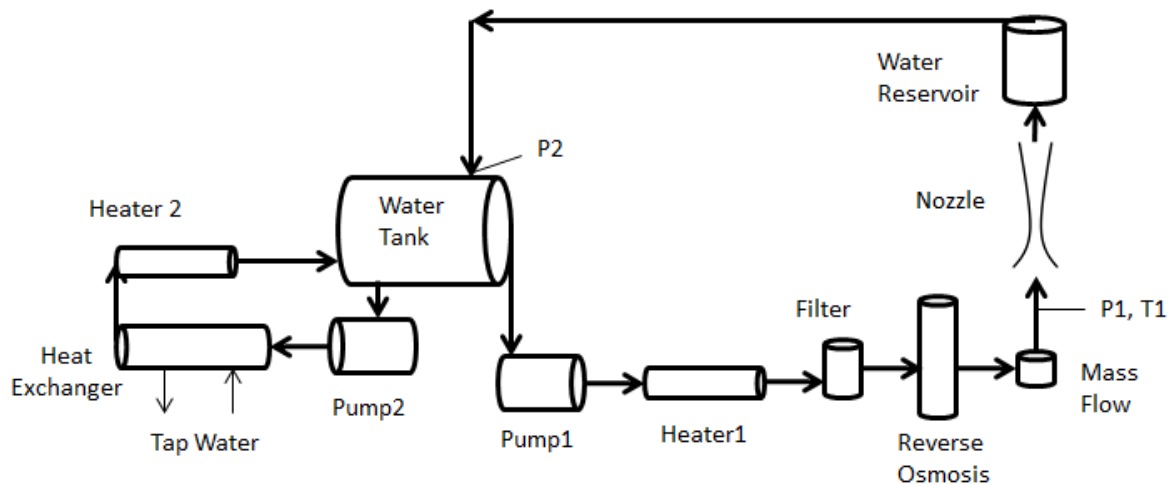


Figure 2.1: Water testing rig.



**Figure 2.2 The water loop setup. On the left there is the water tank, filters, pumps, and heaters. On the right is the test section.**

## **2.2 Nozzles**

### ***2.2.1 Initial Plastic Nozzle***

The first nozzle used is shown in Figure 2.3, with the design given in Figure 2.4. It was machined out of translucent blue PVC, made to operate with refrigerant as well as water. This nozzle was designed so that a borescope camera could visualize flow in the throat. There were several issues that arose from this method. The first issue was that the camera had a max frame rate of 30 frames/ second, resulting in a shutter speed of 0.033 seconds. This shutter speed was not fast enough and the images were blurred. The next issue was the surface finish at the end of the borescope hole was not sufficient to provide a clear view of the nozzle.

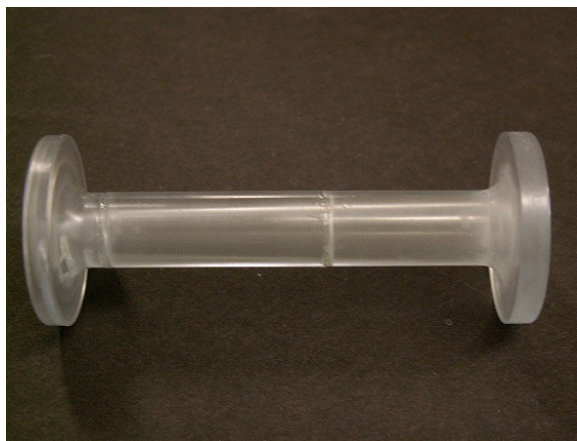


**Figure 2.3: Initial plastic nozzle.**

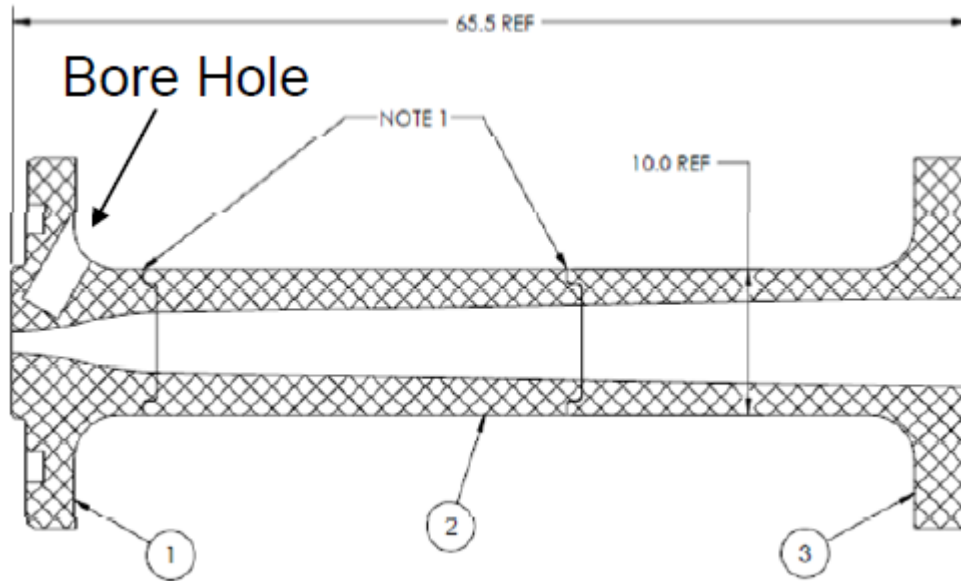


**Figure 2.4: Initial plastic nozzle design (dimensions are in millimeters).**

While using the same nozzle, a camcorder was used to capture the cavitation throughout the nozzle. With ambient light, the images were blurry; however by using a strobe light the cavitation could be visualized. Figure 2.5 shows a few of the images that were captured by using a strobe light. It shows the vapor forming a cloud a few millimeters above the throat before turning back into liquid.

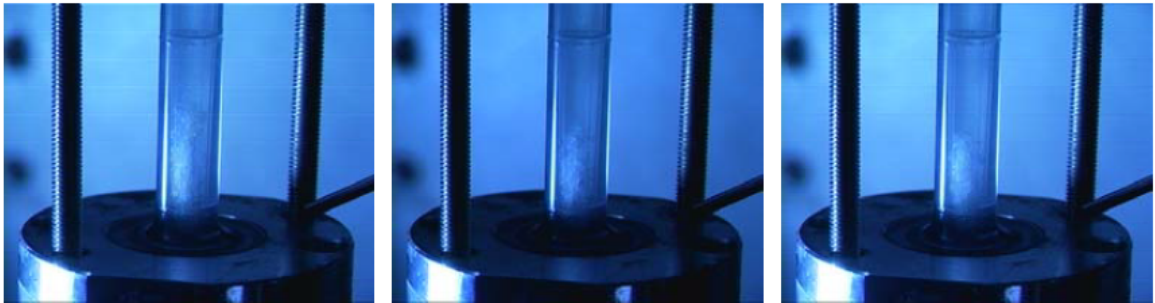


**Figure 2.5: Images of cavitation in initial nozzle with strobe light.**

### ***2.2.2 Square Inlet and Curved Inlet Nozzles***

The next iteration of nozzle design was made to improve the flow visualization. These nozzles were designed to only operate within the water loop. As a result, it was possible to have the nozzles machined out of clear Plexiglas, which was more optically clear. The new design incorporated a two degree expansion angle starting from the throat. To minimize refractive effects, four flat surfaces were added on the outer surface of the nozzle. The throat was moved

further downstream so that it would be easily visible, not covered by the end flanges. Two nozzles were made for testing, one to test a squared off inlet and the other with a gradual curved inlet. Images of the nozzles are shown below in Figure 2.6, and the designs of the nozzles are in Figure 2.7. These nozzles had a throat diameter of 2 mm, and an outlet diameter of 4.5 mm.



**Figure 2.6: Square Inlet (left) and Curved Inlet (right) Nozzles.**

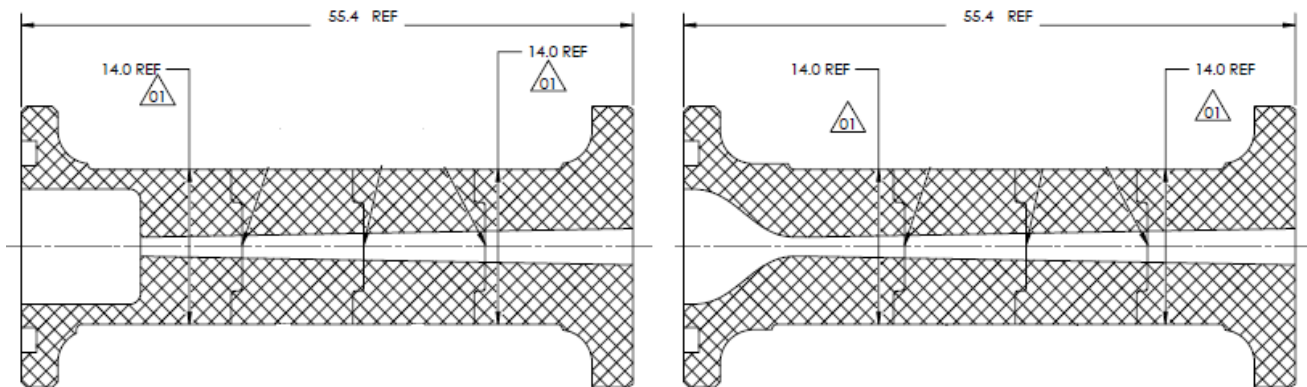


**Figure 2.7: Design of Square and Curved Inlet Nozzles (dimensions are in millimeters).**

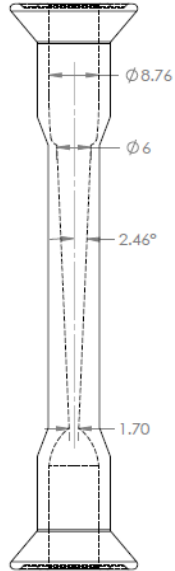
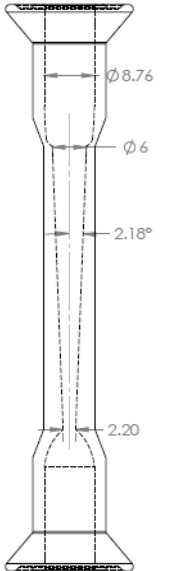
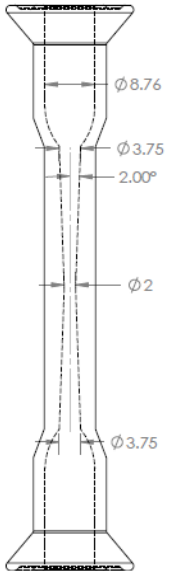
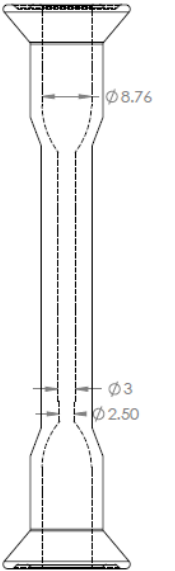
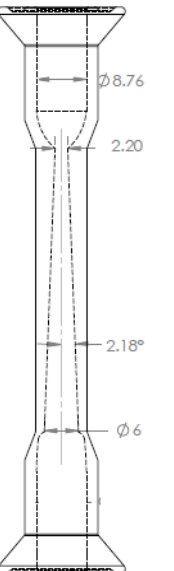
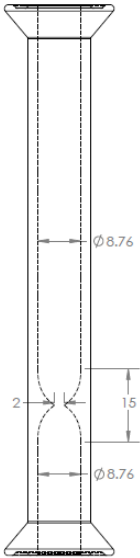
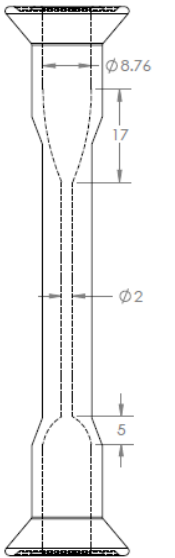
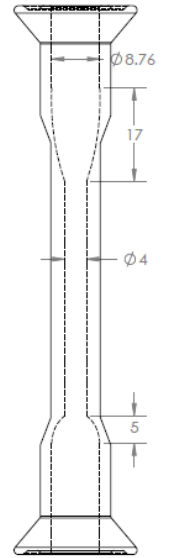
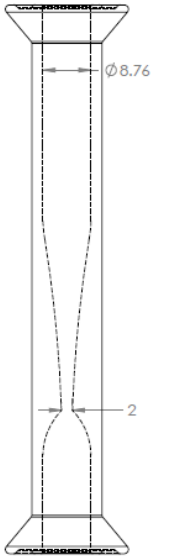
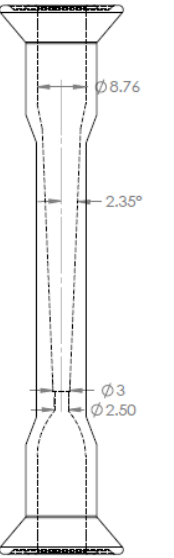


### ***2.2.3 Glass Nozzles***

After the plastic nozzles were tested, the switch was made to use glass nozzles for testing. These glass nozzles were created by Kansas State University's scientific glassblower, Jim Hodgson. The main advantages of using glass were that they took much less time create, and they cost significantly less than the acrylic nozzles. The main disadvantage was that these glass nozzles were blown by hand, meaning that they could not be machined to specific dimensions. The first nozzle made is given in Figure 2.8, shown with a mixture of Rhodamine B dye and water. The throat of the glass nozzle was similar to the curved plastic nozzle, and had a rapid decrease of the diameter leading to the inlet of the throat, with a linear expansion past the throat. Table 1 shows the designs of all the glass nozzles used.



**Figure 2.8: Nozzle 1, with Rhodamine B dye**

					
Nozzle Name	Nozzle 1	Nozzle 2	Nozzle 3	Nozzle 4	Inverse Nozzle 2
Throat Diameter (mm)	1.7	2.2	2	2.5	2.2
Converging	Bell	Bell	2° Angle	Bell	2.18°
Diverging	2.46°	2.18°	2° Angle	Bell	Bell
Section	3.1.3, 4	3.1.3, 3.5, 4	3.1.4	3.1.5	3.2.1
					
Nozzle Name	Nozzle 5	Nozzle 6	Nozzle 7	Nozzle 8	Nozzle 9
Throat Diameter (mm)	2	2	4	2	2.5
Converging	Bell	Straight	Straight	Bell	Bell
Diverging	Bell	Bell- 17 or 5 mm	Bell- 17 or 5 mm	Increasing Expansion Angle	Ogive to 2.35°
Section	3.2.2, 3.4	3.2.3	3.2.3	3.3.1	3.3.2

**Table 1 Glass Nozzle Designs**

## 2.3 Flow Visualization

In order to establish baseline knowledge of what was occurring in the nozzle, photos and video of the flow were needed. Standard video cameras film at thirty frames per second. At a minimum, the velocity in the nozzle was ten meters per second, and the observed area was ten millimeters along the nozzle. Thus the camera had to have the capability of filming at least 1000 frames per second. In addition to the need for a High Speed Camera, proper lenses, and a sufficiently intense light source were needed.

### 2.3.1 High Speed Camera

In order to provide the flexibility required for the project, a SA5 High Speed Camera was purchased from Photron. The camera had a maximum resolution of 1,024 by 1,024 pixels. The frame rate at the maximum resolution was at 7,000 frames per second. The camera could go up to 775,000 frames per second; however, the tradeoff was reducing the resolution down to 128 by 24 pixels.

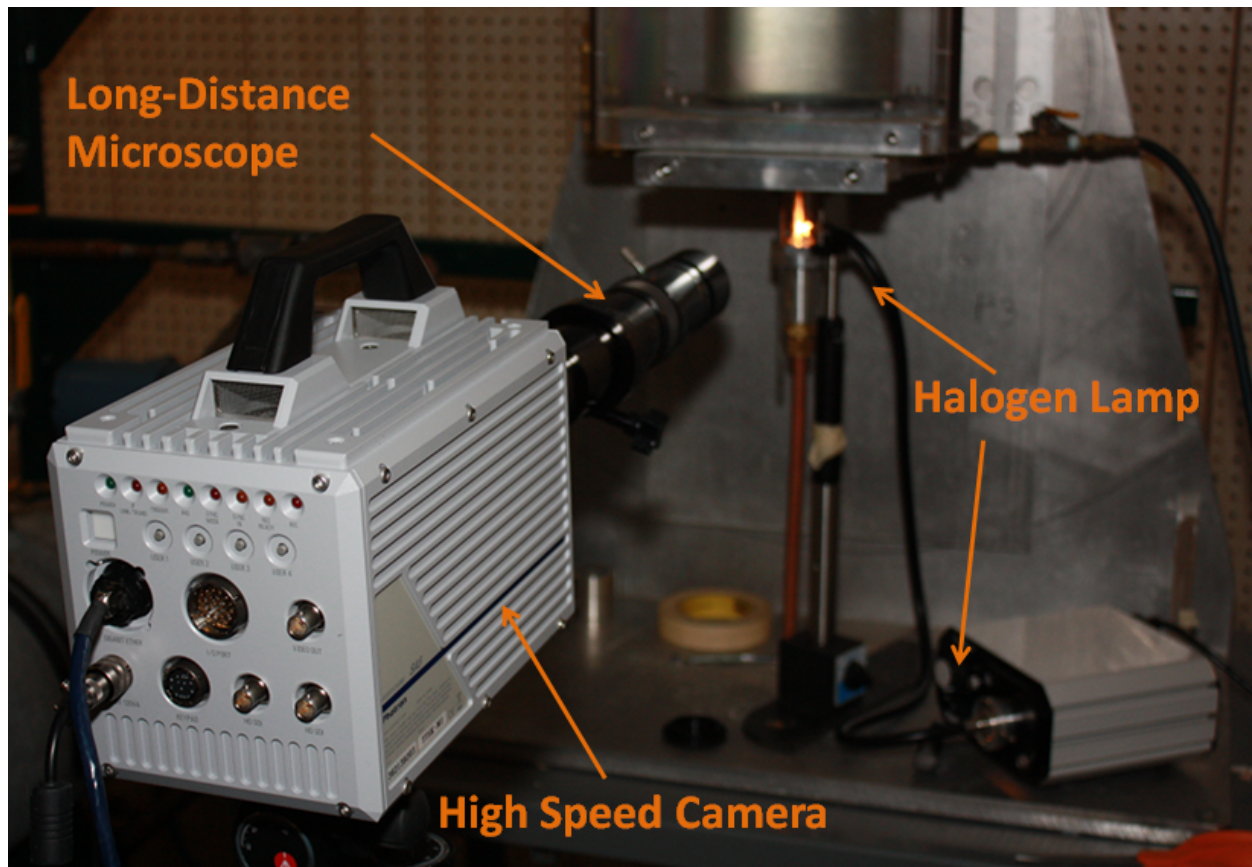


Figure 2.9: Experimental set up with the high speed camera.



Figure 2.9 shows the high speed camera while in use. The camera was connected to a computer through an Ethernet cable. The computer controlled the operation of the camera, using the Photron Fastcam Viewer (PFV) software provided by the manufacturer. The specifications are shown in Appendix A.

### 2.3.2 Lens

In order to develop close up images of the cavitation, a long-distance microscope was purchased. The long-distance microscope was an Infinity K-2 lens with a set of attachments referred to as the Close-Focus (CF) lenses. The specifications are shown in Figure 2.10. Generally all of the data was taken using the CF-1 attachment, as the other attachments had a higher magnification and lower field of view than what was desired. An AF Nikkor 60mm f/2.8D lens was used for the cases where the entire nozzle was to be captured.

K2/SC	STD w/o S Lens			CF-1			CF-1/B			CF-2			CF-3			CF-4		
	Near	Mid	Far	Near	Mid	Far	Near	Mid	Far	Near	Mid	Far	Near	Mid	Far	Near	Mid	Far
WD mm	360	510	980	265	365	580	222	290	418	138	190	205	92	105	125	55	60	63
MAG	0.95	0.64	0.31	1.28	0.86	0.52	1.4	1.07	0.71	2.29	1.52	1.36	3.05	2.56	2.06	5.33	4.74	4.27
FOV mm	6.74	10	20.5	5.0	7.4	12.2	4.6	6.00	9.0	2.80	4.20	4.7	2.10	2.50	3.1	1.20	1.35	1.50

Figure 2.10 Specifications of the Infinity K-2 lens.

### 2.3.3 Lighting

The proper lighting is important in any photography situation. The high speed camera required more light intensity than a conventional video camera. With every increase in the frame rate of the camera more light is needed. In addition to the application of adequate light, the light must be delivered in a form specialized to the type of measurement being made. When the light is delivered directly into the nozzle many of the features could be washed out. For most experiments conducted here, the light was sent through a frosted pane of glass resulting in diffuse light illumination. However, when the cavitation filled up most of the region of interest, direct light is needed to fully penetrate and illuminate the fluid flow. The continuous white lighting source used was a halogen light source from Thor Labs. Shown in Figure 2.9, the halogen light source had a fiber optic cable to deliver the light to the back of the nozzle.

## **2.4 Laser Induced Fluorescence**

To further the understanding of the cavitation, a method for visualizing and measuring the cavitation features was developed for the system. Planar Laser Induced Fluorescence (PLIF) was selected to give the quantitative measurements needed, specifically the void fraction. This method utilized a dye that emitted light in a different wavelength when laser light was directed through the liquid. The high speed camera filmed the emitted fluorescence, while the original laser light was filtered out using a band pass optical filter. The result was that the liquid regions, containing the dye, would absorb directed laser light and fluoresce, while the vapor in the mixture was essentially transparent and hence would not fluoresce. The dark areas were thus identified as vapor, while the light emitting areas were liquid. While this method was developed for measuring the void fraction, it also provided the surface features for estimating the velocity of the cavitating fluid.

### ***2.4.1 Yag Laser***

For implementing PLIF, pulse Yag Lasers emitting a 532 nm laser beam were used. The first laser that was used was a MINILASE 30 Hz Yag Laser from New Wave Research. This laser, used with the High Speed Camera, provided an image every 30 hz, with a pulse duration of about 5 nanoseconds. These images were useful for void fraction visualization and measurements. However, as the laser only flashed every 0.033 seconds, this laser was not suitable for velocity measurements. The next laser used was a Gemini- 15 hz Dual Yag laser from New Wave Research. This laser provided two laser flashes every 0.067 seconds. However, the spacing between the two laser flashes could be finely adjusted, enabling a pair of images to be used for measuring the velocity. For the best results the laser pulses had to be formed into a thin sheet. The entire optical setup is shown in Figure 2.11. A TSI light arm was used to direct the laser beam from the optical table to the test section. At the end of the light arm a -15 mm cylindrical lens formed the light into a diverging sheet, and a 200 mm spherical lens focused the thickness of the light sheet. In addition, a positive cylindrical lens focused the light vertically to reduce the widening of the light sheet. By being focused in the matter, the stray reflections of the light in the glass were minimized, cutting down on scattering of light and keeping the light intensity at a more uniform level. Another method of obtaining measurements was to orient, i.e. tilt, the light sheet at an angle, thereby enabling visualization of the void cross sectional area.

However, while this method provided a view of the cross-sectional distribution of the void fraction, it also increased the depth of the measurement field, blurring the images.

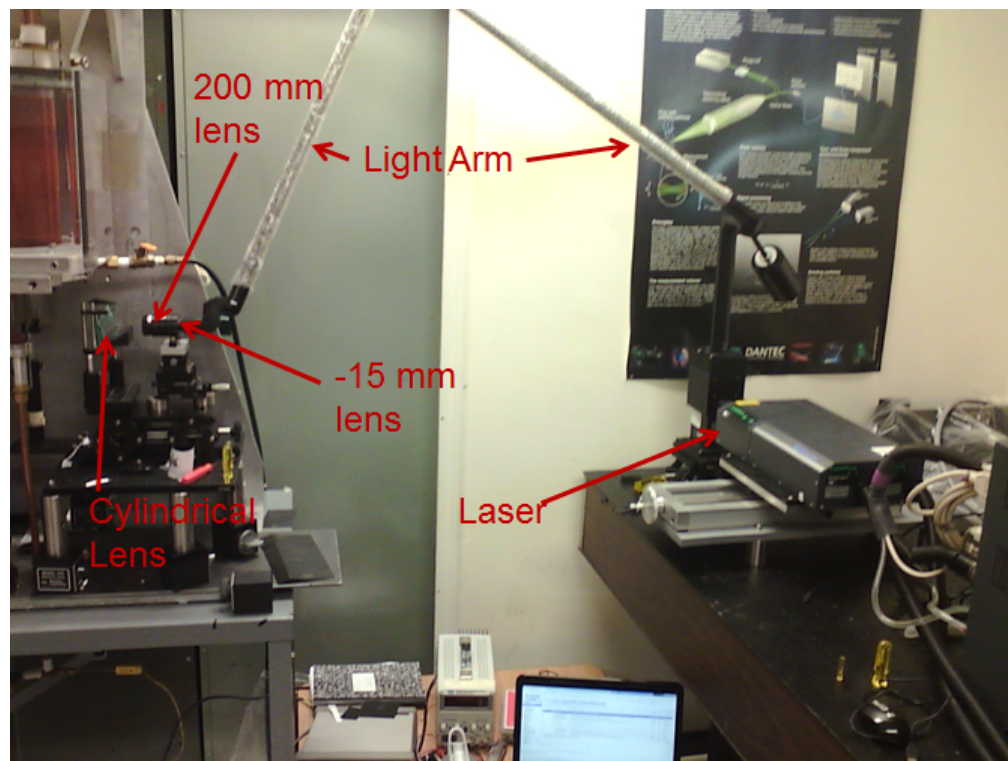


**Figure 2.11 Setup of the laser system.**

#### ***2.4.2 Dye concentration of Rhodamine B in water***

Rhodamine B dye was selected due to its fluorescing properties. With the dye present, the liquid absorbed the 532 nm light from the Yag Laser and shifted the wavelength of the emitted light to a nominal wavelength near 630 nm. The proper concentration of the dye had to be determined before filling up the water loop. To test for the concentration, glass tubes with an outer diameter of 3 mm were filled with various concentrations. Figure 2.12 shows the results of using varying concentrations of Rhodamine B dye in water. The concentrations are labeled as the weight of the dye per the volume of water. The laser light sheet was used at the same intensity setting for these images. At 7 mg/ 1000 L the laser light permeated through the entire volume of water and the air bubbles are dark. However, the intensity of the light emitted from the liquid was low. At 7 mg/ 10 L the intensity of the light in the liquid was high, but the laser light was not capable of penetrating throughout the liquid. 7 mg/ 100 L was a good compromise between the

two, obtaining a high emitted light intensity while allowing the light to penetrate throughout the liquid.

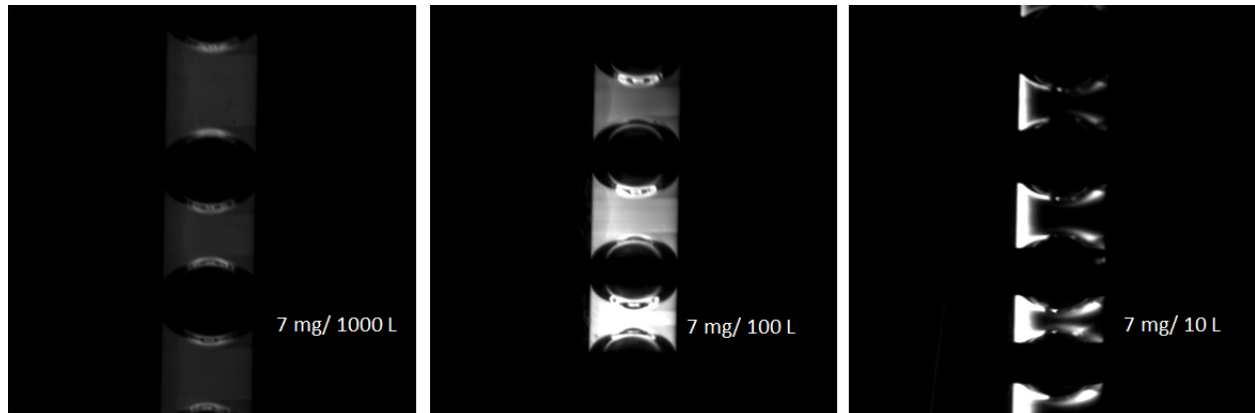


**Figure 2.12 Laser illuminated images on 3 millimeters tubes with air bubbles.**

## **2.5 Computer processing in Matlab Code**

Matlab was utilized to run the computer processing of the velocities and void fractions. The process for calculating the void fraction is shown in Figure 2.13. The laser illuminated image of the flow and no flow were loaded into the code. A threshold level filtering of these images was taken, replacing these images in 8 bit gray scale to binary black and white. The code then counted the number of pixels and compared the number of white pixels in the flow to the white pixels in the no flow image. This gave the liquid fraction, which could be inverted to give the void fraction. The void fraction code was modified so that a batch of images could be loaded as well as breaking down the images into multiple sections. The velocity code loaded two sequential images and used a correlation algorithm to determine the vertical pixel shift between the two images. This pixel shift was converted into a velocity, using the ratio of pixels to millimeters and the time between the images. Both of the Matlab codes are found in Appendix B.

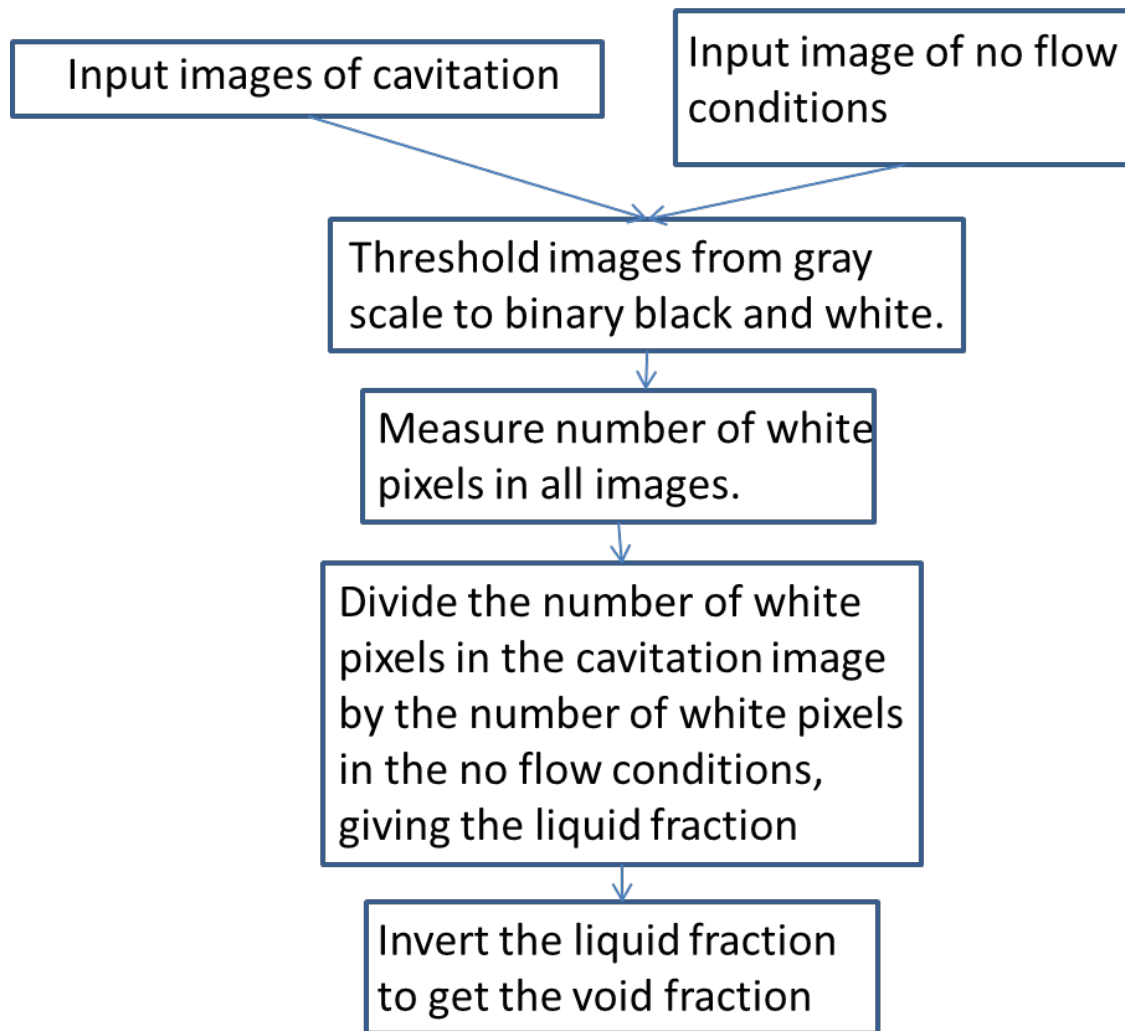


**Figure 2.13 Process for calculating void fraction.**

## **Chapter 3 - Flow Visualization Results**

The intention of this section is to explore what cavitation will result from various nozzle geometries and various test conditions. Cavitation manifested in several different ways in the nozzle: attached wall cavitation, shear cavitation, swirl cavitation, and travelling bubble cavitation. The attached wall cavitation was typically found in venturi nozzles and featured a vapor column initiating off of the walls. Shear cavitation was found in nozzles with a rapid expansion, an orifice. When the fluid flowed out of the orifice it turned into a jet, referred to as an orifice jet, composed of liquid and vapor. The shear forces from the orifice jet caused vapor to form around it. Swirl cavitation was found in nozzles with a rapid expansion and an Internal Flow Modifier (IFM). The IFM rotated the flow prior to the inlet of the nozzle, and after the throat the orifice jet expanded radially, causing a large vapor region. Certain nozzle geometries caused the flow to start as attached cavitation, but then transition into shear cavitation. Travelling bubble cavitation was found when there were dissolved gases in the water. These gases separated from the water at low pressures. These gas bubbles formed nucleation sites which initiated cavitation. Most of the time these gas bubbles disrupted other forms of cavitation, but it was possible for these types of cavitation to be present at the same time. Travelling bubble cavitation can induce or disrupt attached wall cavitation. In some cases a bubble was capable of moving past the attached wall cavitation, displacing the fluid around it, but leaving its initiation unchanged.

### **3.1 Attached Wall Cavitation**

Similar to the hydrofoil in Figure 1.6 B [2], attached wall cavitation occurs in venturi nozzles. A venturi nozzle is a nozzle that converges to a minimum area throat and then diverges without any sudden changes in the diameter. In the case of the nozzles used for this research, there was a reduction in area from nine millimeters to approximately 2 mm in the converging section. After the minimum area cross section, the throat, the cross sectional area increased at a very gradual rate, ranging between zero to five degree expansion. In these venturi nozzles the attached wall cavitation initiated a few millimeters downstream of the minimum area of the throat. This location was most likely caused by a separation region. Table 2 contains the flow and visualization data for the images in this section.

Figure #	Nozzle	Flow Rate (g/s)	Inlet Temp (°C)	Frame Rate (Frames/Second)	Light Source	Lens
3.1	Curved Inlet	38	30	20,000	Diffuse	Microscope
3.2	Curved Inlet	40-50	30	10,000	Diffuse	Microscope
3.4	Square Inlet	37	30	20,000	Diffuse	Microscope
3.6 A	Nozzle 1	45	30	6,000	Diffuse	60 mm
3.6 B	Nozzle 1	45	30	20,000	PLIF	Microscope
3.6 C	Nozzle 1	39	30	20,000	PLIF	Microscope
3.6 D	Nozzle 1	39	30	6,000	Diffuse	60 mm
3.7	Nozzle 1	39-45	30	6,000	Diffuse	60 mm
3.8	Nozzle 1	39-45	30	6,000	Diffuse	60 mm
3.9 A	Nozzle 1	42	40	20,000	Diffuse	60 mm
3.9 B	Nozzle 1	42	50	20,000	Diffuse	60 mm
3.10 A	Nozzle 2	48	30	35,000	Diffuse	60 mm
3.10 B	Nozzle 2	48	30	10,000	Diffuse	Microscope
3.10 C	Nozzle 2	48	30	25,000	Diffuse	60 mm
3.10 D	Nozzle 2	48	30	10,000	Diffuse	Microscope
3.11	Nozzle 2	22-29	30	20,000	Diffuse	60 mm
3.13	Nozzle 3	39	30	15,000	Diffuse	60 mm
3.14 B, C	Nozzle 4	37	30	20,000	Diffuse	60 mm
3.14 D, E	Nozzle 4	119	30	20,000	Diffuse	60 mm
3.15 A, B	Nozzle 4	37	30	20,000	Diffuse	60 mm
3.15 C, D	Nozzle 4	37	30	20,000	PLIF	60 mm
3.15 E, F	Nozzle 4	119	30	20,000	Diffuse	60 mm
3.15 G, H	Nozzle 4	119	30	20,000	PLIF	60 mm

**Table 2 Flow and visualization data for 3.1 Attached Wall Cavitation.**

### ***3.1.1 Curved Inlet Acrylic Nozzle***

Referred to in section 2.2.2, the Curved Inlet Acrylic Nozzle was the first nozzle that utilized the high speed camera. Shown in Figure 2.6, this nozzle had a gradual inlet, followed by a two degree, linear, expansion. Section A shows the initiation of the attached wall cavitation. The initiation of the nucleation occurred at approximately two millimeters downstream of the throat, most likely at the separation region. In this plastic nozzle there were typically three vapor columns of attached wall cavitation, roughly equidistant from each other. These vapor columns moved around the circumference of the nozzle, occasionally dissipating or splitting into two

separate columns. In the first third of section B, the vapor streams split off from the wall and as this transition occurred the stream became turbulent. From that point where it became turbulent, more light was scattered, resulting in less light reaching the camera.

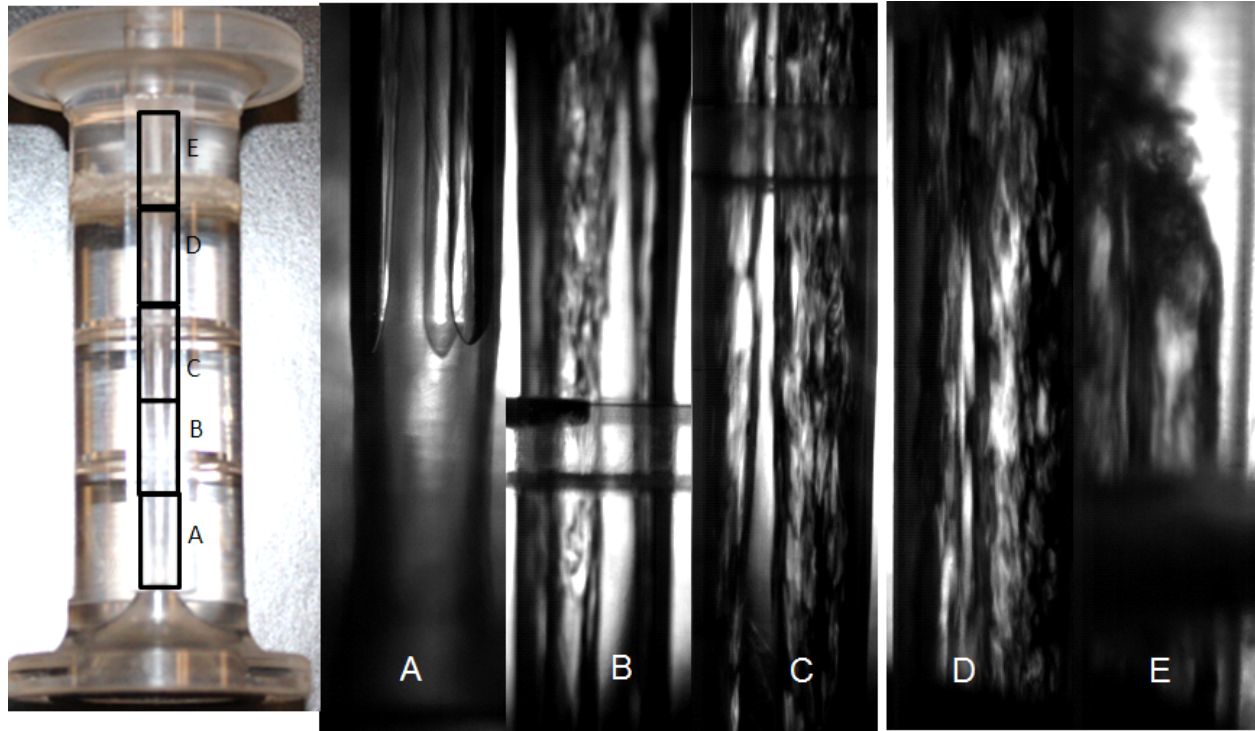


**Figure 3.1 Curved Inlet Nozzle visualization.**

In Figure 3.2 the images show the initiation of the cavitation at mass flow rates of 40.3 and 50.1 grams per second. The horizontal bars are to show the distance from the bottom of the viewing area. As can be seen in the picture, there was very little deviation of the initiation site at different flow rates. It is also important to note that the initiation point was constantly moving laterally around the inside wall. In both cases the initiation was in the region 4- 4.5 mm for the majority of the time, with some time also spent in the 4.5-5mm region. Changing the mass flow rate did not affect the initiation of the cavitation, however it did affect the length of the cavitation region. Figure 3.3 shows the distance the cavitation travelled before shocking back to liquid. At very low mass flow rates there was no inception of cavitation. There was a range of mass flow rates where the cavitation may or may not initiate. This region is shown in the red boxes, and are from around 35 to 40 grams per second. From 40 grams per second and higher the cavitation was always present. This data showed a positive linear relationship between the mass flow and the length over which the cavitation formed.



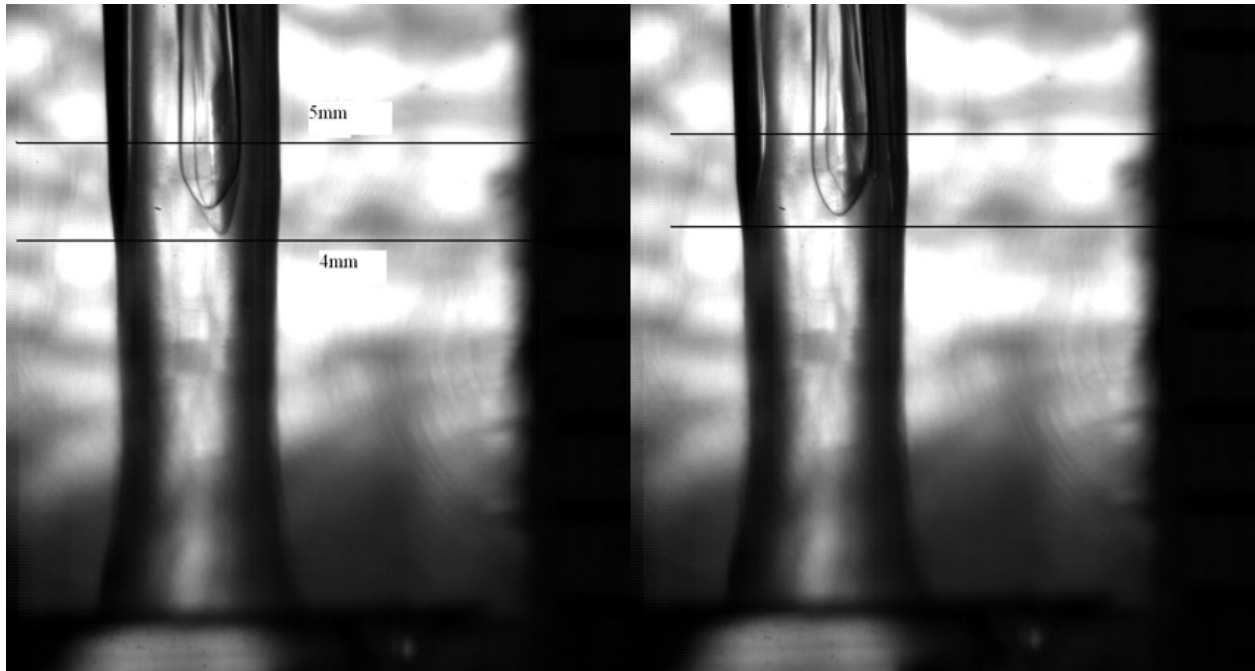


Figure 3.2 Initiation of cavitation, left image 40.3 gram/s, right image 50.1 gram/s

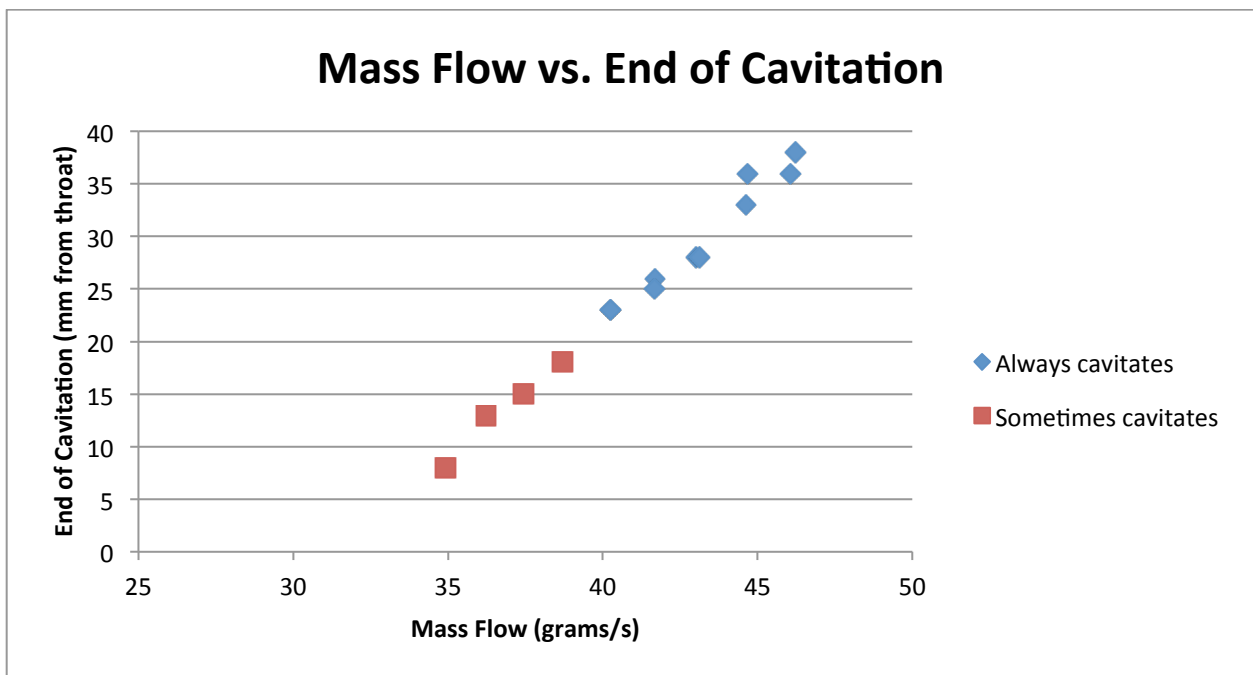
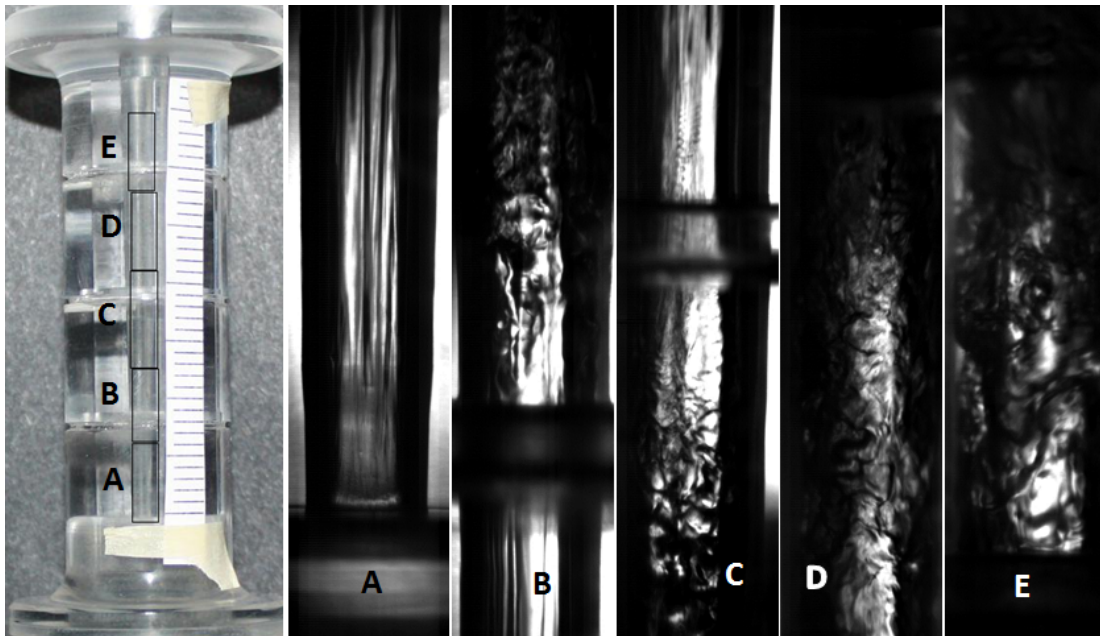


Figure 3.3 End of cavitation distances

### ***3.1.2 Sudden Inlet Acrylic Nozzle***

The Sudden Inlet Acrylic Nozzle is shown in Figure 2.6. The images of the flow are shown in Figure 3.4. As shown in section A, the cavitation initiated at throat. Unlike the curved inlet, instead of 3-4 vapor columns that moved around, attached wall cavitation formed around the perimeter. This cavitation switched from laminar to turbulent in section B. From that point on, the cavitation was similar to that in the other acrylic nozzle. The cavitation spread out and became more turbulent until starting to break apart in section E.



**Figure 3.4 Square Inlet Nozzle visualization.**

### ***3.1.3 Nozzle 1 and Nozzle 2***

The first glass nozzles used for the current research had a design similar to that of the plastic nozzle. The design was changed to account for these nozzles being hand crafted by the scientific glassblower. These nozzles were very similar, with a very sudden decline in diameter into a throat, both had a gradual, linear, expansion for about 50 mm. At the end of the linear expansion the diameter expanded out to 9 mm. For the first nozzle, Nozzle 1, the minimum throat diameter was around 1.7 mm, while the throat diameter of the second nozzle, Nozzle 2, was around 2.2 mm. This change resulted in an expansion angle of 2.46 degrees for the first nozzle and 2.18 degrees for the second nozzle.

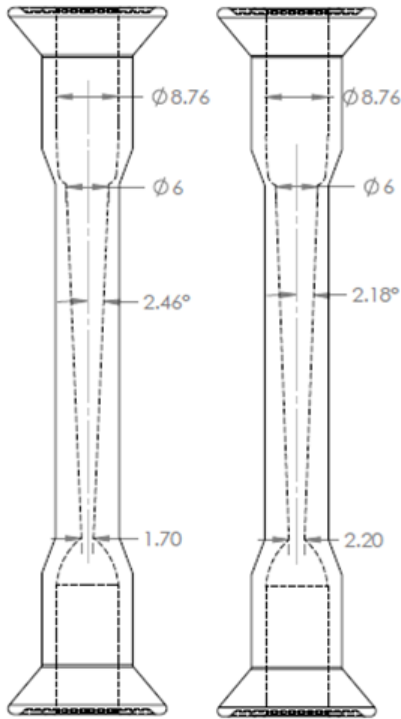


**Figure 3.5 Design of Nozzle 1 and Nozzle 2**

Unlike the Curved Inlet Acrylic Nozzle, the flow conditions for Nozzle 1 did affect the initiation of cavitation. The first two flow conditions are shown in Figure 3.6. The cavitation shown in Figure 3.6 A and B had water flowing through the nozzle with an inlet temperature of 30 °C and a mass flow rate of 45 g/s. There was a discontinuity on the inner surface of the glass that was a nucleation site for the cavitation. In order to take void fraction measurements, the yag laser illuminated the nozzle. During this process the cavitation location changed, with the changes shown in Figure 3.6 C and D. The cavitation moved to the left side and was much closer to the minimum area throat. While the pump power remained constant the mass flow rate shifted from 45 to 39 g/s. This was the only nozzle and the only flow condition in which the laser affected the cavitation.

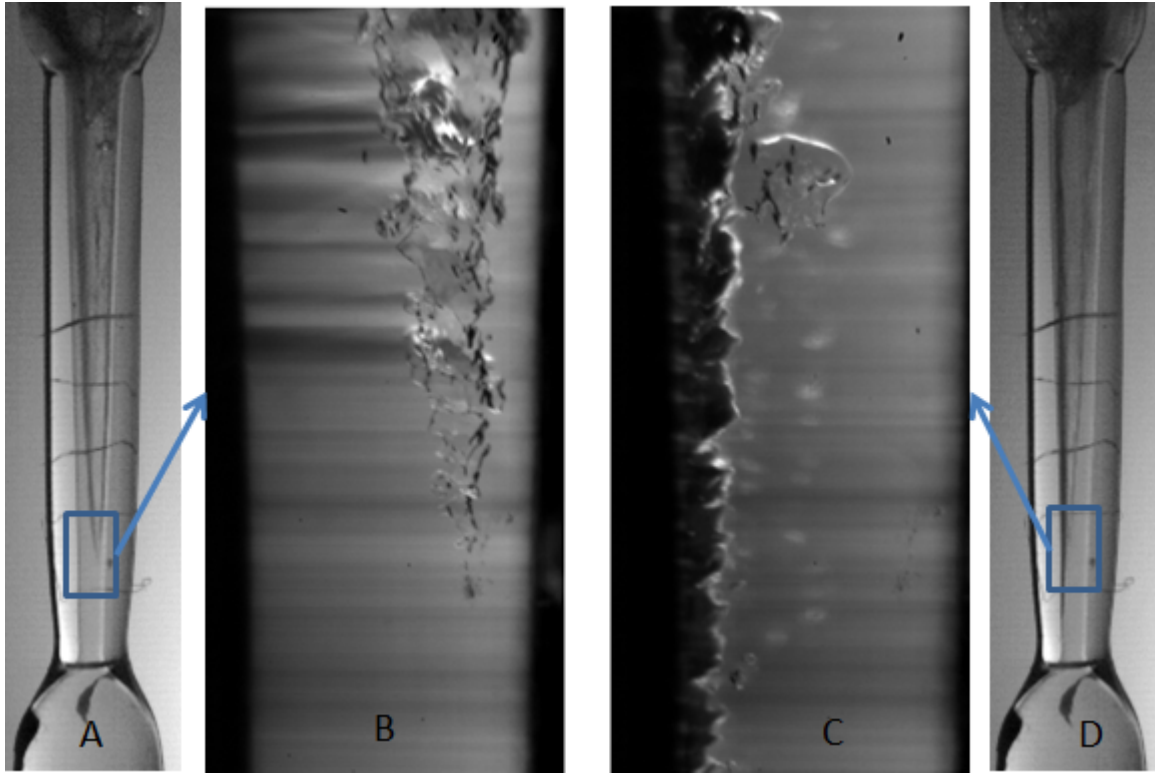


**Figure 3.6 Nozzle 1, (A, B) 30 °C; (C, D) 30 °C Laser Induced Cavitation**

Figure 3.7 shows how the laser affected the cavitation. In the first image the cavitation was nucleating off of the discontinuity. In the next frame the laser illuminated the nozzle. Immediately after the laser flash a small bubble appeared upstream of the original nucleation zone. The downstream section of this bubble expanded and merged with the established cavitation. As the downstream section of the bubble expanded, the upstream edge of the bubble established a nucleation site just below the discontinuity. The images in Figure 3.8 continue after the sequence in Figure 3.7. In frame 119 the cavitation stopped nucleating off of the wall. In frame 278 the cavitation started to nucleate near the throat, although its location shifted around. In frame 399 the laser flashed again, and from that point on the cavitation nucleated on the left side, a few millimeters downstream of the minimum area throat. To distinguish the two flow conditions this new flow is referred to as laser induced cavitation.

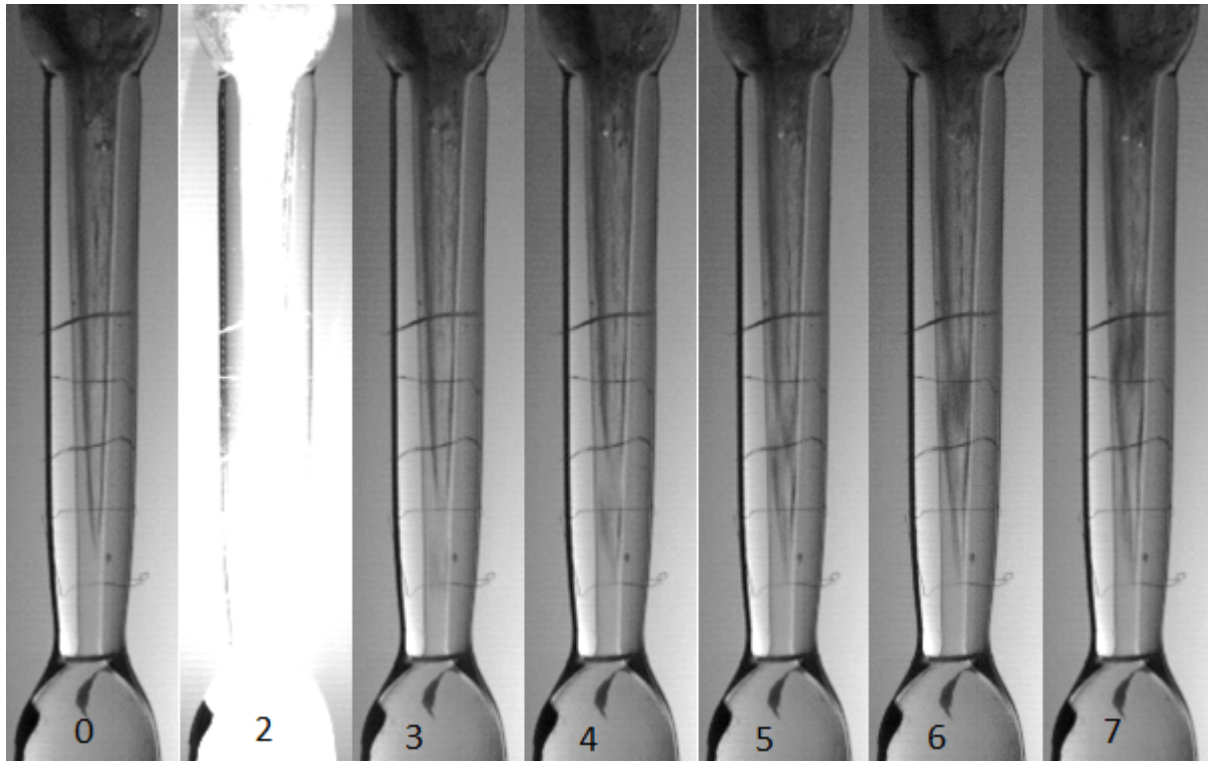


**Figure 3.7 Nozzle 1, sequence with frame numbers.**

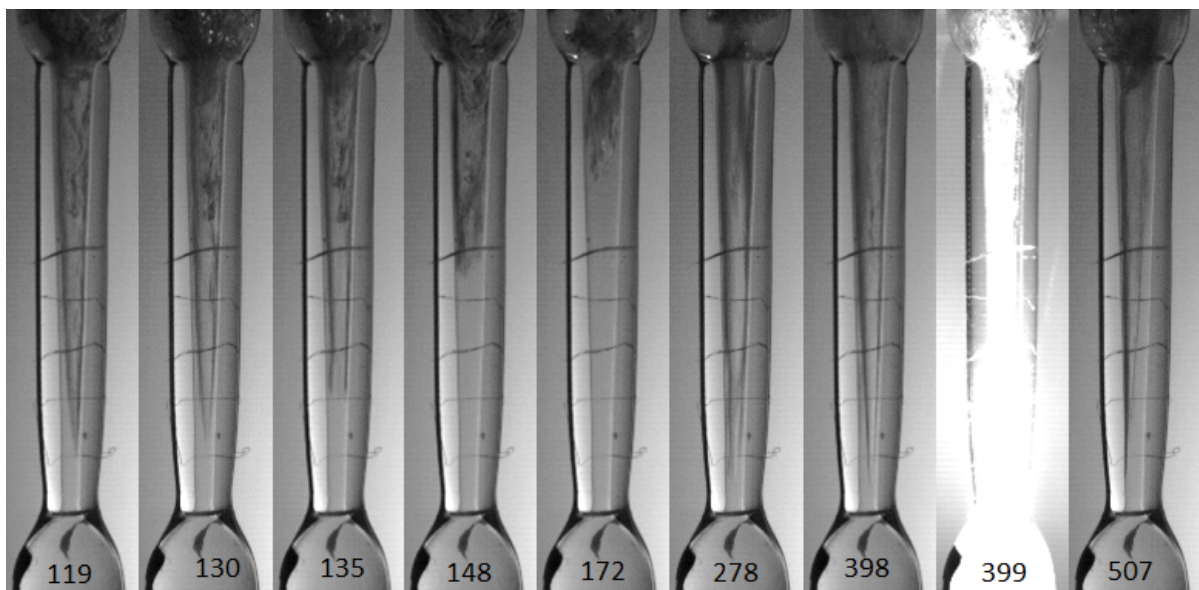


**Figure 3.8 Nozzle 1, sequence continued from Figure 3.7.**

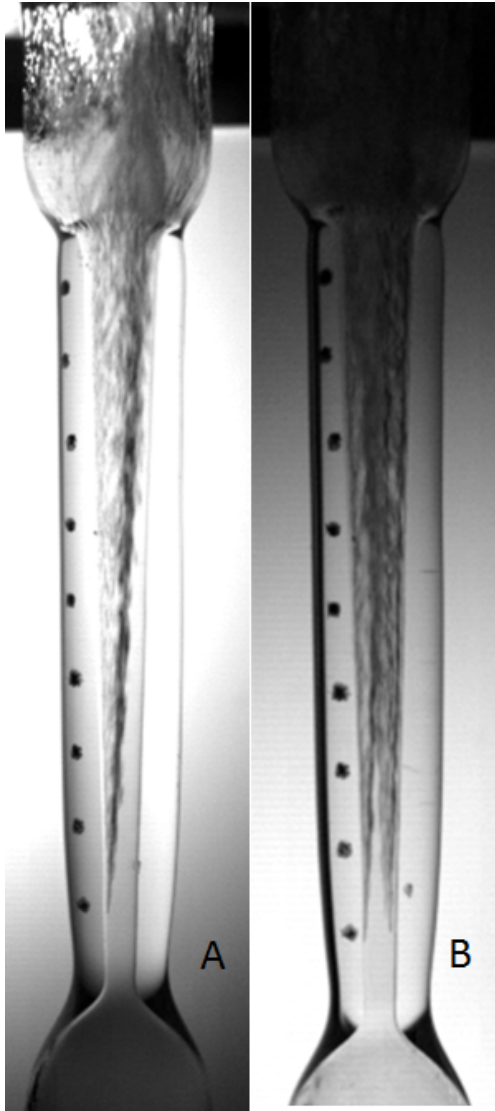


**Figure 3.9 Nozzle 1, (A) 40C, (B) 50C.**

In addition to the change in the nucleation site from laser flashes, different inlet temperatures also changed the nucleation site. As seen in Figure 3.9, at 40 °C the cavitation nucleated at the same approximate location as the laser induced cavitation. When the temperature was increased to 50 °C, the cavitation still nucleated on the left wall, however, two additional vapor columns developed.

Nozzle 2 also showed that a discontinuity on the wall created a nucleation site. The discontinuity was a small scratch that acted as a nucleation site and was located approximately one mm from the throat. Unlike Nozzle 1, neither an increase in temperature, nor flashes from the laser changed the nucleation site. The nozzle was heat treated, which removed this discontinuity. Figure 3.10 shows the cavitation in Nozzle 2 before and after the heat treatment.

After the heat treatment, the nucleation was similar to that found in the plastic nozzles. Like the plastic nozzles, the nucleation site moved around the circumference. This nucleation also formed into a column of attached wall cavitation. However, in the glass nozzle there was only one column of attached wall cavitation, with a few small columns occasionally splitting off. This main stream predominantly favored one side of the nozzle. This was due to a slight asymmetry, where the cavitation favored the side that expanded at a slightly larger rate. Changes in the mass flow rate, as seen in Figure 3.11, did not change the nucleation site. Raising the mass flow rate increased the distance that the vapor travelled before turning back into liquid.

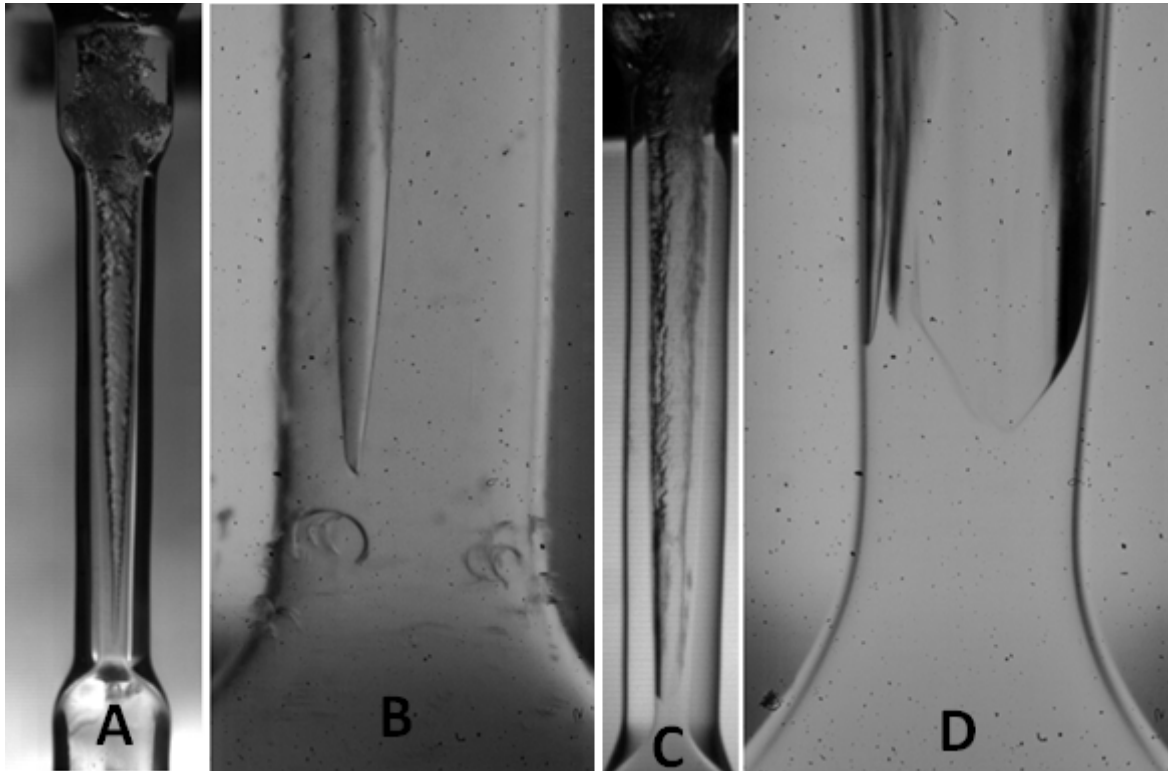


**Figure 3.10 Nozzle 2, (A,B) With Scratch; (C, D) No scratch.**



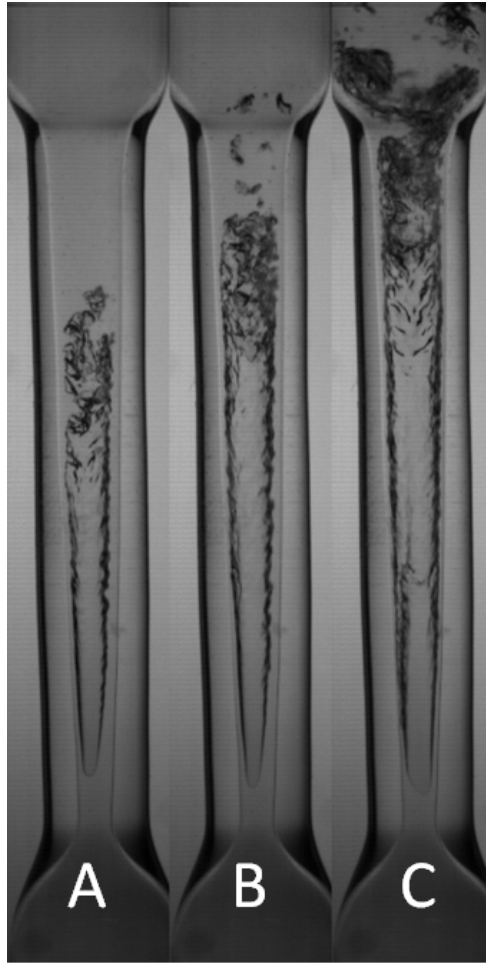


**Figure 3.11 Nozzle 2, (A) 20 g/s, (B) 22 g/s, (C) 29 g/s.**

#### ***3.1.4 Nozzle 3***

In order to test the effect of the inlet geometry, Nozzle 3 was created to have the inlet geometry mirror the outlet geometry. As Figure 3.12 shows, on both sides of the throat there was a 2 degree expansion angle, with a throat diameter of 2 mm. As seen in Figure 3.13, with a mass flow rate of 39 g/s and an inlet temperature of 30 °C, the results for Nozzle 3 mirrored those found in Nozzle 2. There was a single column of vapor that formed a few millimeters from the throat. After the vapor traveled down the nozzle it expanded. The cavitation did favor one side of the nozzle, once again due to a slight asymmetry in the nozzle.



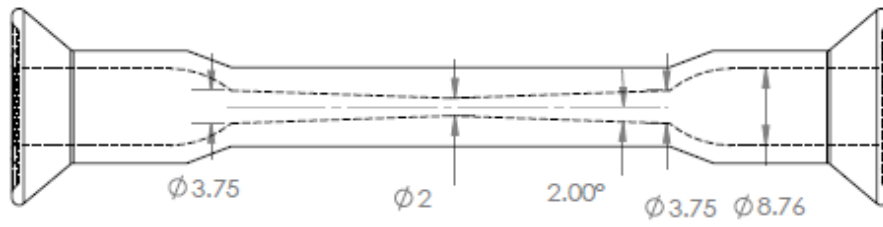


**Figure 3.12 Design of Nozzle 3**

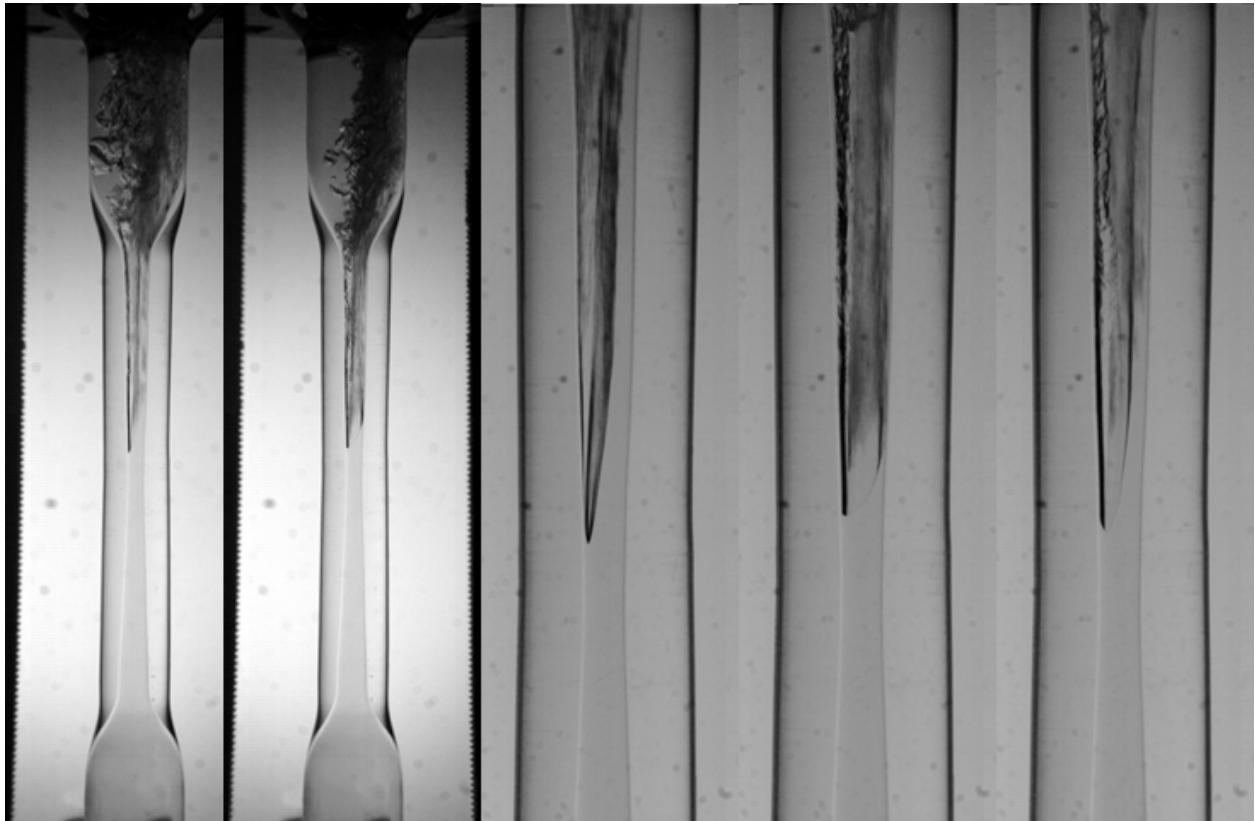


**Figure 3.13 Nozzle 3 visualization.**

### 3.1.5 Nozzle 4

Nozzle 4 featured an ogive expansion, which is defined as a sudden increase in the diameter. This nozzle, with the design in Figure 3.14 A, had a bell inlet into the throat. At the throat there was a rapid increase in the diameter; from 2.5 mm to 3 mm. After the ogive, the nozzle had a constant diameter of 3 mm. Figure 3.14 shows the cavitation throughout the entire nozzle, while Figure 3.15 shows the close up view. This nozzle was tested with mass flow rate of 37 g/s and 119 g/s.

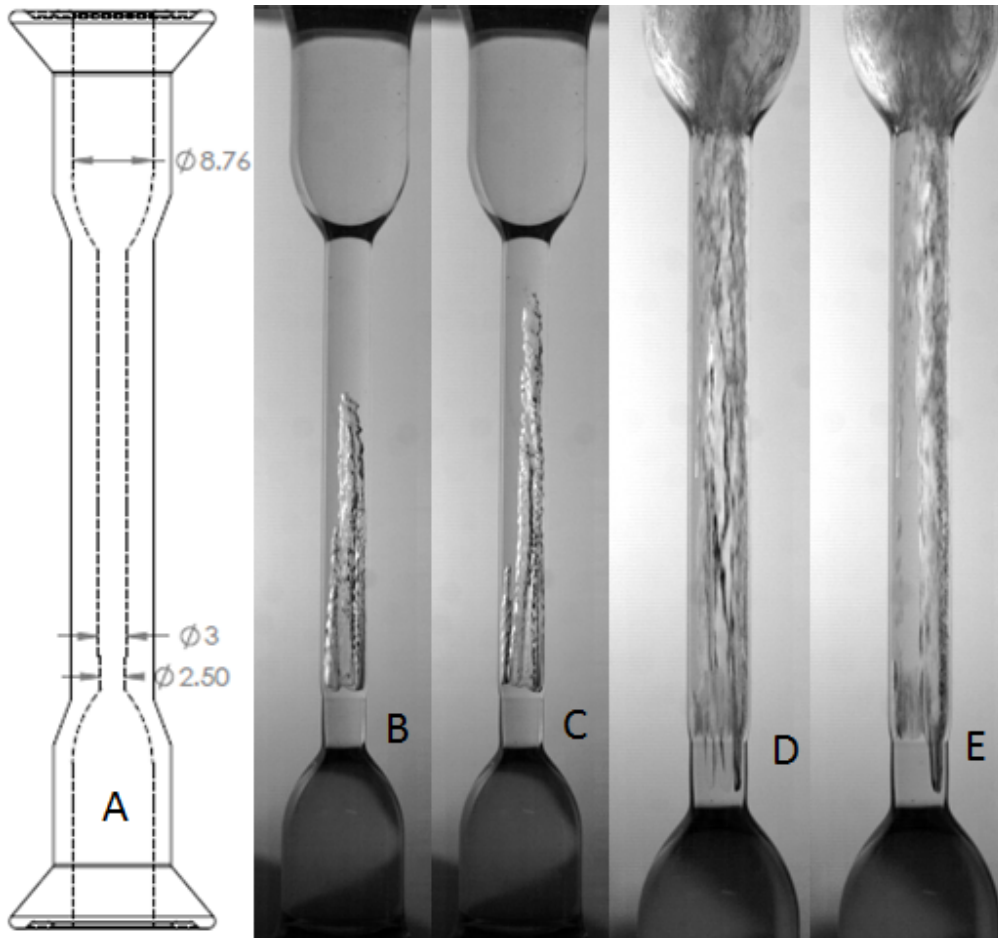


**Figure 3.14 Nozzle 4 visualization.**

At 37 g/s attached wall cavitation nucleated slightly above the ogive expansion, with multiple streams nucleating around the circumference. Like the previous cases, the stream transitioned from laminar to turbulent as it separated from the wall. The cavitation columns continued downstream and shocked back into liquid, with the position of the shock back fluctuating between the two positions shown in Figure 3.14 B and C. There was a small

discontinuity on the left side of the nozzle, midway through the straight section. This discontinuity prevented the attached wall cavitation from forming around it. At 119 g/s the cavitation nucleated below the ogive expansion, and the cavitation extended throughout the nozzle. The discontinuity on the left side of the nozzle prevented the attached wall cavitation from the throat from forming, however, at this mass flow rate it acted as a nucleation site. The cavitation found in the straight ogive was the same as the venturi nozzles. There was attached wall cavitation that, as it separated from the wall, became turbulent. The change in the flow rate primarily changed how far down the nozzle the vapor traveled before turning back to liquid. Unlike the previous venturi nozzles, the higher flow rate did change the location of the nucleation.

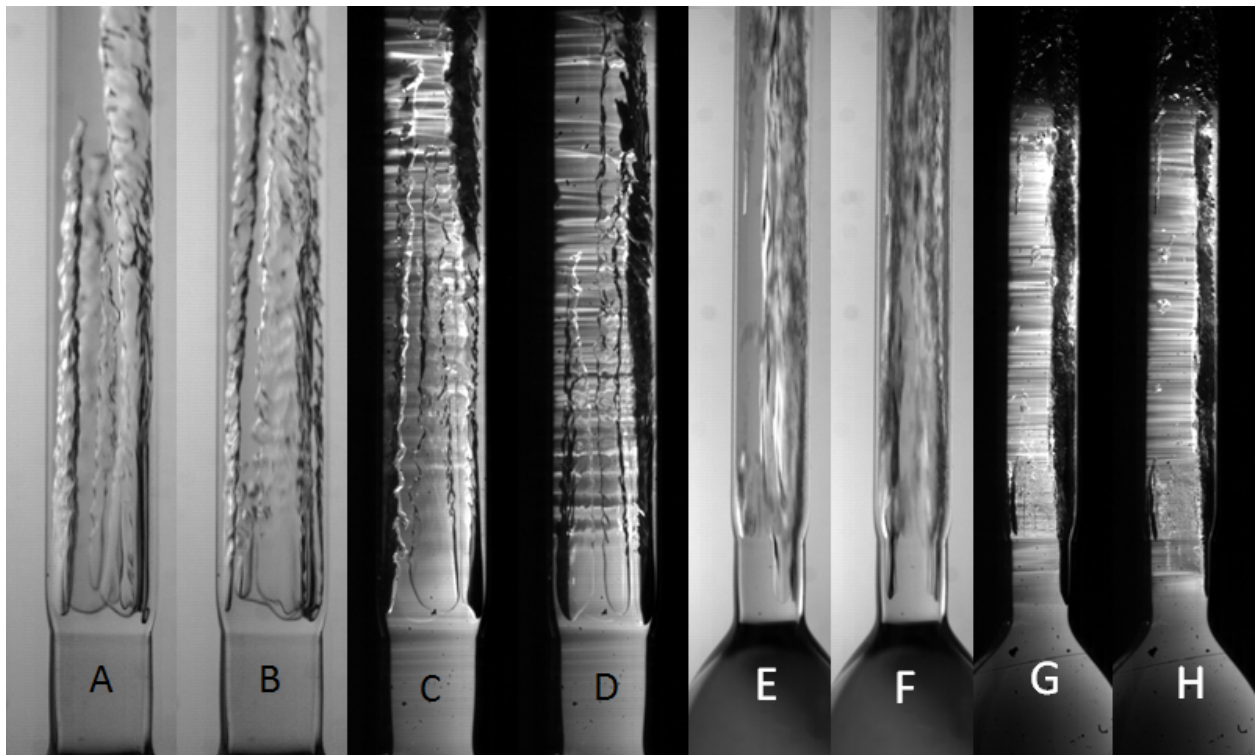


**Figure 3.15 Nozzle 4 visualization, zoomed in.**

## 3.2 Shear Cavitation

Shear cavitation was found in nozzles with a rapid expansion, an orifice. When the fluid flowed out of the orifice it turned into a jet, referred to as an orifice jet, composed of a turbulent mixture of liquid and vapor. The shear forces from the orifice jet created a vapor cloud that formed around the jet. In the orifice nozzle the inlet geometry affected the flow. When the inlet to the orifice converged, a cyclical bursting flow pattern emerged. In this cyclical pattern the shear cavitation caused a vapor cloud to grow around the turbulent liquid region, and then the vapor cloud collapsed from the top down leaving only the turbulent core. For nozzles with a constant diameter inlet into the throat there was still a turbulent core; however, these nozzles did not exhibit the cyclical pattern. Shear cavitation permanently formed a vapor cloud around the orifice jet, and there was a thin film of water on the surface of the nozzle. Table 2 contains the flow and visualization data for the images in this section.

Figure #	Nozzle	Flow Rate (g/s)	Inlet Temp (°C)	Frame Rate (Frames/Second)	Light Source	Lens
3.16	Inverse Nozzle 2	44	30	10,000	Diffuse	60 mm
3.17	Inverse Nozzle 2	44	30	30,000	PLIF	60 mm
3.19	Nozzle 5	69	30	15,000	Diffuse	60 mm
3.20	Nozzle 5	69	30	15,000	PLIF	60 mm
3.22	Nozzle 6	80	30	15,000	Diffuse	60 mm
3.23	Nozzle 6	80	30	15,000	Diffuse	60 mm
3.24	Nozzle 7	174	30	15,000	Diffuse	60 mm
3.25	Nozzle 7	174	30	15,000	Diffuse	60 mm

**Table 3 Flow and visualization data for 3.2 Shear Cavitation.**

### 3.2.1 Inverse Nozzle 2

For this section of testing, Nozzle 2 was turned around in the testing setup. It had a 2 degree converging inlet, leading into a rapid expansion. As shown in Figure 3.16, this flow was cyclical, although not entirely periodic. Using the first image as a reference, the flow initially showed a few bursts, composed of a highly turbulent combination of liquid and vapor. These bursts formed into a centralized, turbulent core, the orifice jet. Shear cavitation caused a vapor cloud to form around the orifice jet. The features on the outside of the vapor cloud in frame 210 showed no vertical movement, although they rotated around the core. The area outside of the vapor cloud was liquid with tiny bubbles suspended in it. These bubbles showed little movement

overall. Eventually the vapor cloud started to contract. It contracted from the top on down to the bottom. Once the vapor core collapsed the bursting motion started the cycle over again. In the images shown in Figure 3.16 it took about 0.0415 seconds for a complete cycle. The time for each cycle was not entirely periodic, since each time the cycle started it took a seemingly random amount of time to complete. Changing the mass flow did not have any visible effect. Most likely this cyclical pattern was caused by the vapor cloud causing the velocity in the turbulent core to decrease. Once the velocity of the core decreased, the pressure rose above the vapor pressure, and the cloud would then collapse downward. At this point the turbulent core fluctuated, decreasing the cavitation into small fluctuations. Since cavitation constricts the flow, when that cavitation was removed the mass flow rate increased. This mass flow rate increase then caused the velocity to increase, starting the process over again.

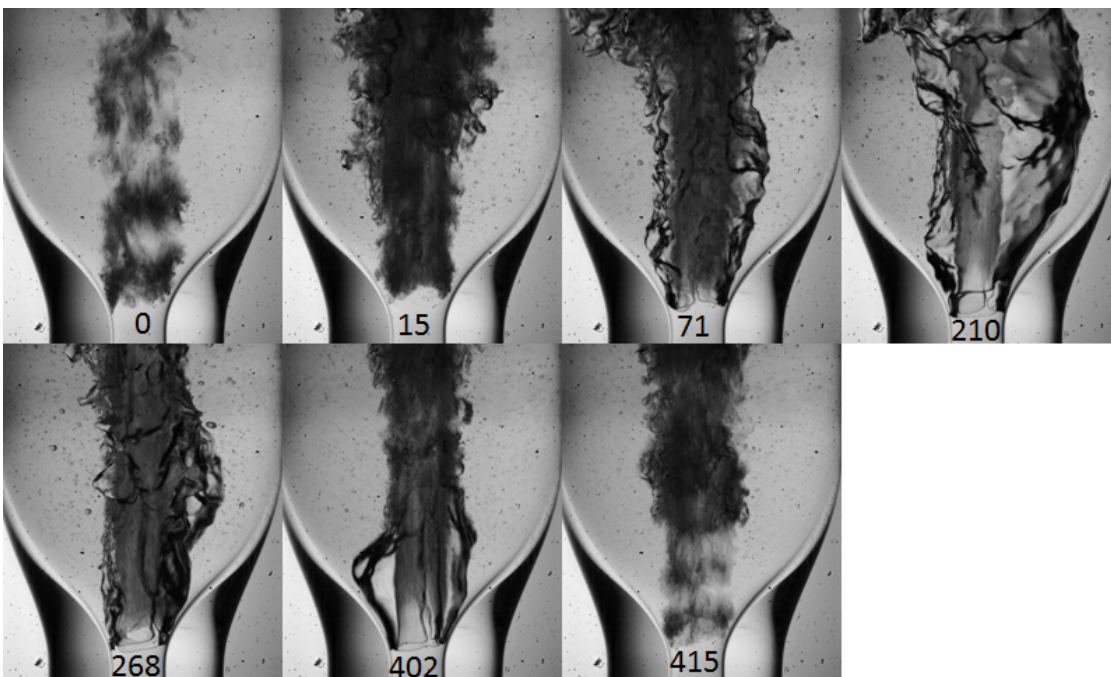


**Figure 3.16 Inverse Nozzle 2 sequence with frame numbers.**

Figure 3.17 shows the flow while using PLIF for visualization. The right side is where the laser plane enters, at first illuminating the liquid. It then intersected the vapor, the darkened area. The core was very bright due to the turbulent nature of the flow; the light being scattered (refracted and reflected) in every direction. Some of this scattered light travelled in the direction of the camera, travelling through the liquid regions. Thus, there was a higher light intensity

observed in the core than in the pure liquid regions, where the illumination was from diffuse light. Since the light was scattered at the core there was a very low intensity of light on the left side of the image.

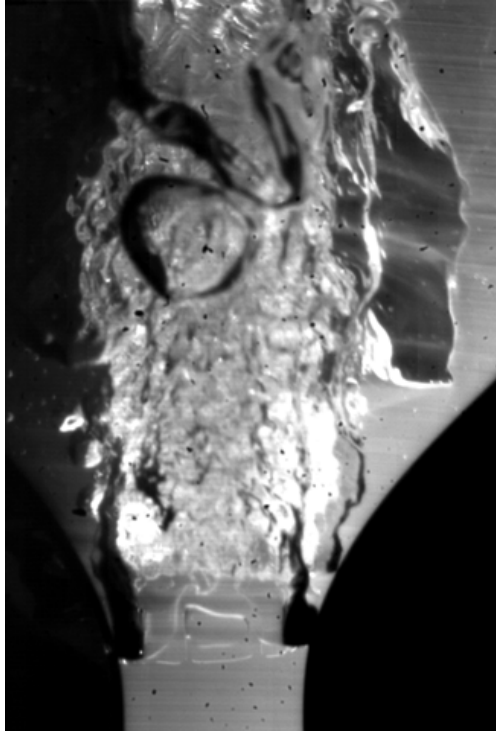


**Figure 3.17 Inverse Nozzle 2 PLIF.**

### ***3.2.2 Nozzle 5***

Nozzle 5, shown in Figure 3.18, had a similar outlet to the previous nozzle, although the outlet was longer. The inlet featured a bell inlet into the throat. The cyclical nature of the flow is shown in Figure 3.19. The first image shows the orifice jet. Shear cavitation created a region of stagnant vapor on the outside of the orifice jet. Between the vapor cloud and the wall was liquid. In the next image, frame 40, the orifice jet at the bottom is seen starting to expand. In the next sequential images the orifice jet expanded into the vapor region, leaving smaller vapor clouds around it. On frame 305 the orifice jet contracted back to the size of the throat, and afterwards the disorganized vapor clouds start to merge together. On frame 601 the vapor region formed into a single vapor cloud around the orifice jet. Once the vapor cloud coalesced, the cloud started forming closer to the throat, until frame 1929, when it started forming at the throat. It was also at

this point that the vapor cloud started to collapse. This collapse resulted in the shrinking of the top region's vapor core. Once the core had shrunk, the turbulent liquid core started to expand. This was a similar effect to that observed in Nozzle 2 inverse. The main difference is that since the outlet was so long, some vapor was always present around the core.

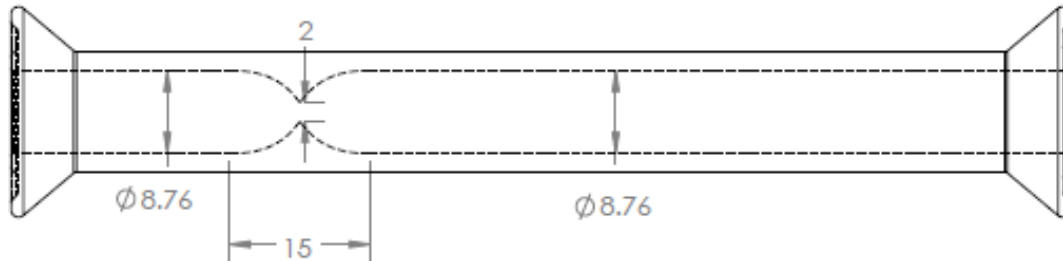


**Figure 3.18 Design of Nozzle 5**

Figure 3.20 shows the PLIF visualization of Nozzle 5. The first image shows the flow as the vapor cloud around the orifice jet is first descending, similar to frame 2120 in Figure 3.19. This image shows a liquid boundary next to the wall. The dark region was the vapor cloud. The bright middle was from the light scattered by the orifice jet. The second image shows the flow as the orifice jet was expanding into the vapor regions, similar to frame 158. The third image shows the orifice jet as the vapor started to form around it, similar to frame 25.



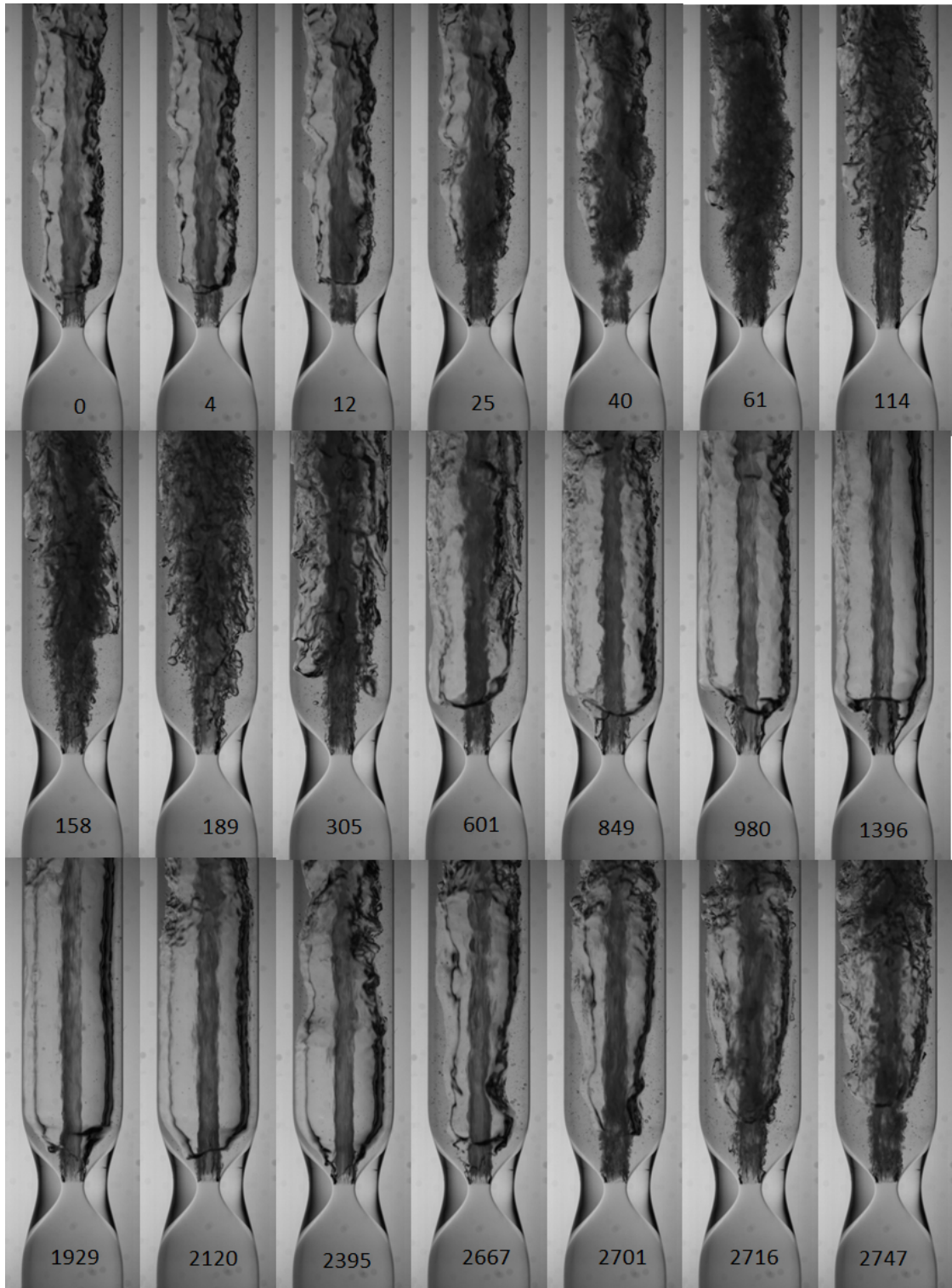


**Figure 3.19 Nozzle 5 sequence with frame number.**





**Figure 3.20 Nozzle 5 PLIF images.**

### ***3.2.3 Nozzle 6 and Nozzle 7***

Two nozzles, shown in Figure 3.21, were made that had a 50 mm straight section in between the two ends, one with a throat diameter of 2 mm and the other with a throat diameter of 4 mm. On each side of the straight section there was a bell. However, the bells had different geometries. On one side the bell expanded rapidly from the straight diameter, either 2 mm or 4 mm, to the 8.76 mm diameter in 5 mm. On the other side the bell had a more gradual expansion, taking 17 mm to expand.

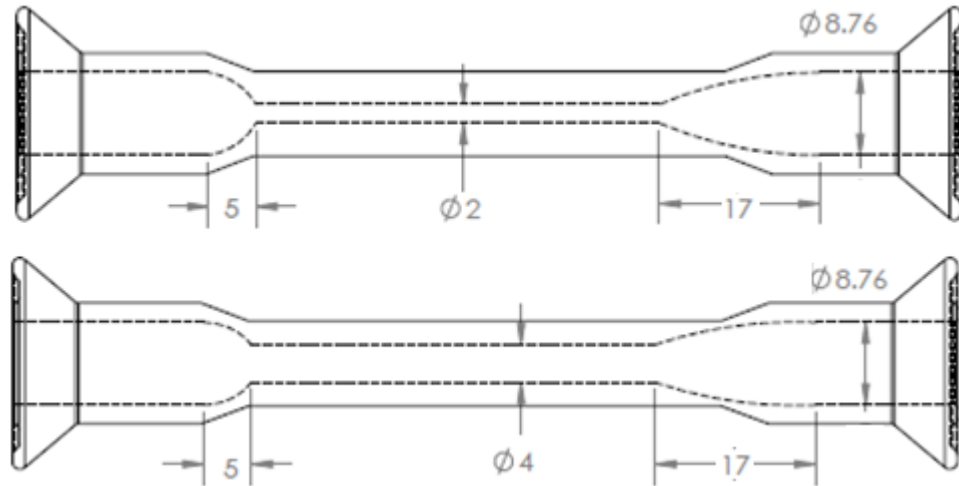


**Figure 3.21 Design of Nozzle 6 and Nozzle 7.**

Nozzle 6, with the gradual and rapid outlets is shown in Figure 3.22 and Figure 3.23, respectively. There was very little difference in the observed flow characteristics for the two nozzles. There was the orifice jet in the middle of the nozzle, surrounded by vapor, and with a thin layer of liquid on the wall. The turbulent liquid core was approximately the same diameter as the throat. The results for Nozzle 7 are shown in Figure 3.24 and Figure 3.25. The results were essentially the same as Nozzle 6. As opposed to the previous nozzles that had a converging inlet, there was no cyclical behavior in the flow. The only change is the turbulent liquid core moved around, up to a 10 degree tilt angle from vertical.

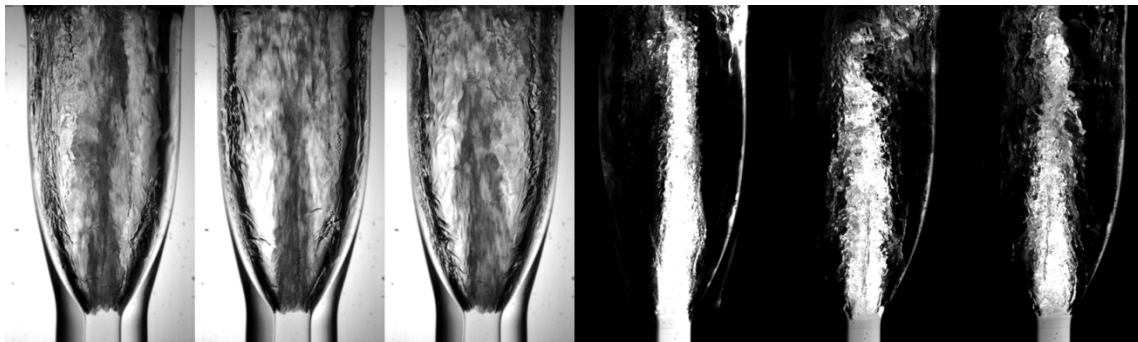


**Figure 3.22 Nozzle 6, gradual expansion flow visualization.**

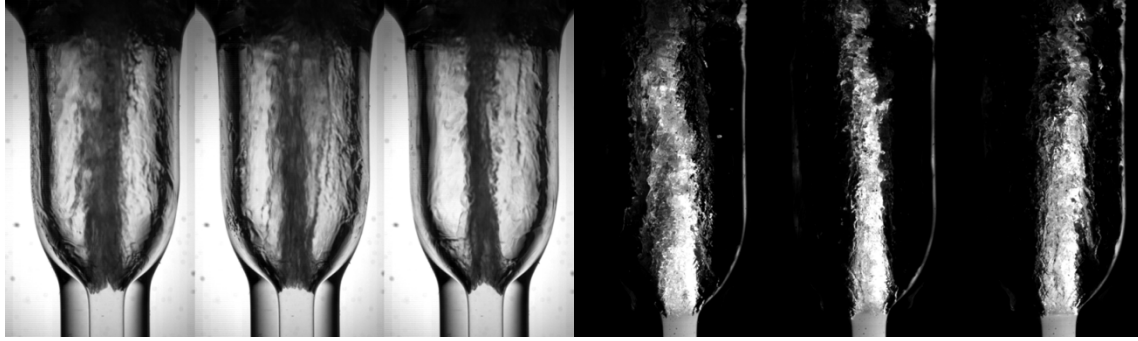


**Figure 3.23 Nozzle 6, rapid expansion flow visualization.**

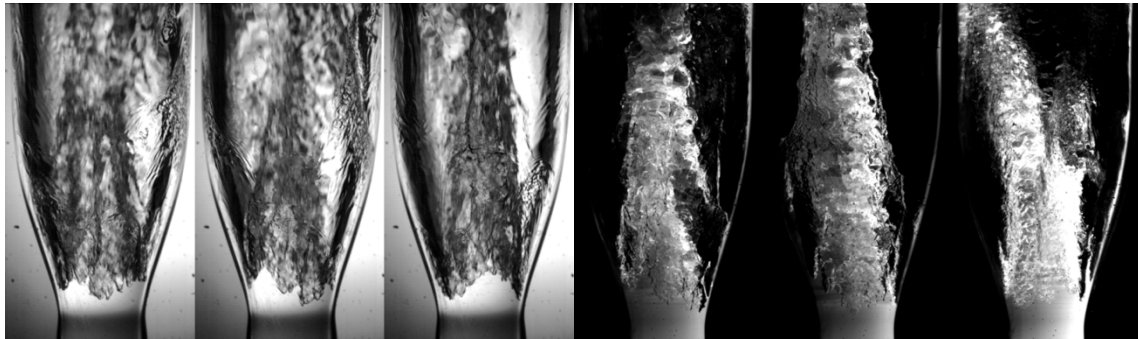


**Figure 3.24 Nozzle 7, gradual expansion flow visualization.**

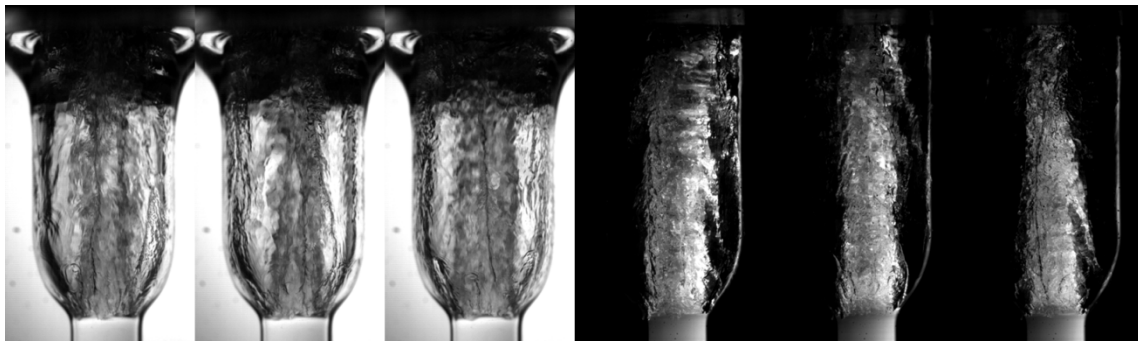


**Figure 3.25 Nozzle 7, rapid expansion flow visualization.**

### 3.3 Mixed Cavitation

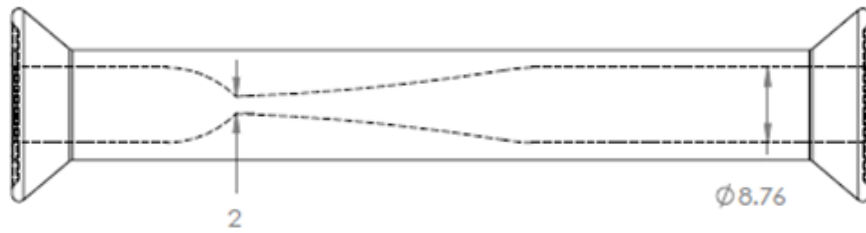
Mixed cavitation was a mixture of attached wall cavitation and shear cavitation. This flow was typified by an initial region that had attached wall cavitation, with a low expansion angle. Once the expansion angle was sufficiently large, the flow switched from attached wall cavitation to shear cavitation. A turbulent core formed in the midst of the attached wall cavitation. The attached wall cavitation flowed into the vapor cloud surrounding the turbulent core. This vapor cloud followed the cyclical pattern of collapsing from the top down, and then reforming around the core. Table 4 contains the flow and visualization data for the images in this section.

Figure #	Nozzle	Flow Rate (g/s)	Inlet Temp (°C)	Frame Rate (Frames/Second)	Light Source	Lens
3.27	Nozzle 8	42	30	15,000	Both	60 mm
3.28	Nozzle 8, IFM	68	30	15,000	Both	60 mm
3.29	Nozzle 9	38	30	20,000	Diffuse	60 mm

**Table 4 Flow and visualization data for 3.3 Mixed Cavitation.**

#### 3.3.1 Nozzle 8

Nozzle 8, with the variable expansion angle shown in Figure 3.26, was designed to feature the largest expansion angle in the middle of the expansion. The resulting flow is shown in Figure 3.27. Similar to the venturi nozzle, attached wall cavitation was initiated downstream of the throat. Once the nozzle expansion angle reached around 10 degrees the cavitation switched from attached wall to shear cavitation. At this point, just like the orifice flow there was a turbulent core. Around the core was a solid cloud of vapor, and there was a thin water film on the wall. There was the same cyclical flow pattern that was observed for the orifice nozzle with a converging inlet. The outer vapor cloud collapsed downwards. As it fell down to the venturi/orifice interface, the orifice jet then expanded, filling up the regions that had held vapor with the turbulent mixture of liquid and vapor. Figure 3.28 shows the flow characteristics for Nozzle 8 using the Internal Flow Modifier. The attached wall cavitation was still present in the initial region after the throat, although it can be seen curving around, no longer in a vertical column. The flow downstream of the attached cavitation was observed to form a highly turbulent mixture of liquid and vapor.



**Figure 3.26 Design of Nozzle 8.**

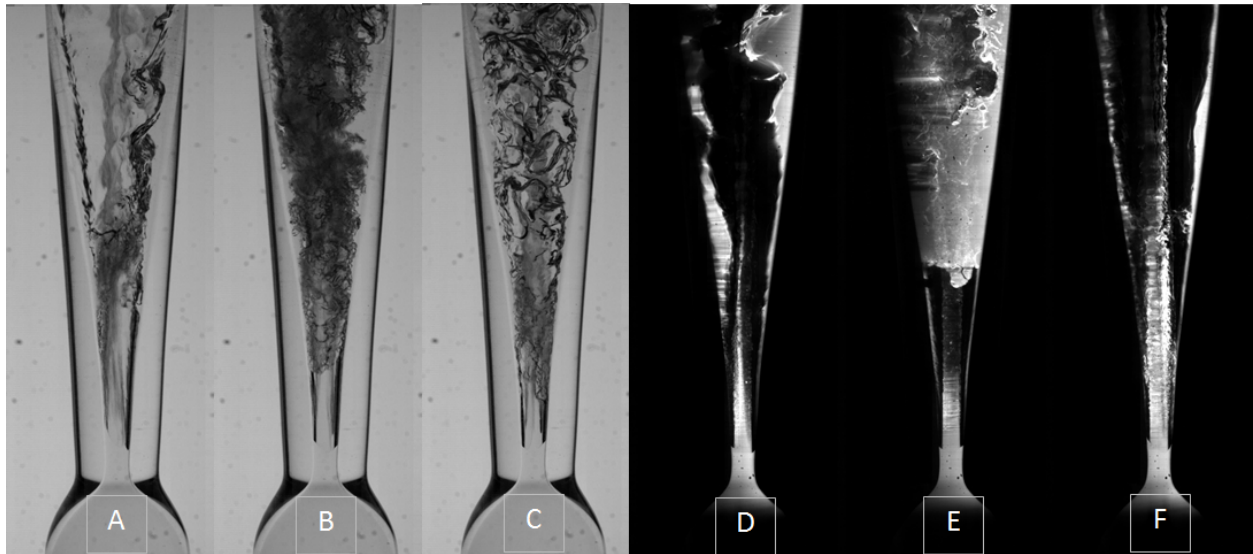


**Figure 3.27 Nozzle 8 flow visualization, (A,B,C) diffuse light; (D,E,F) PLIF.**

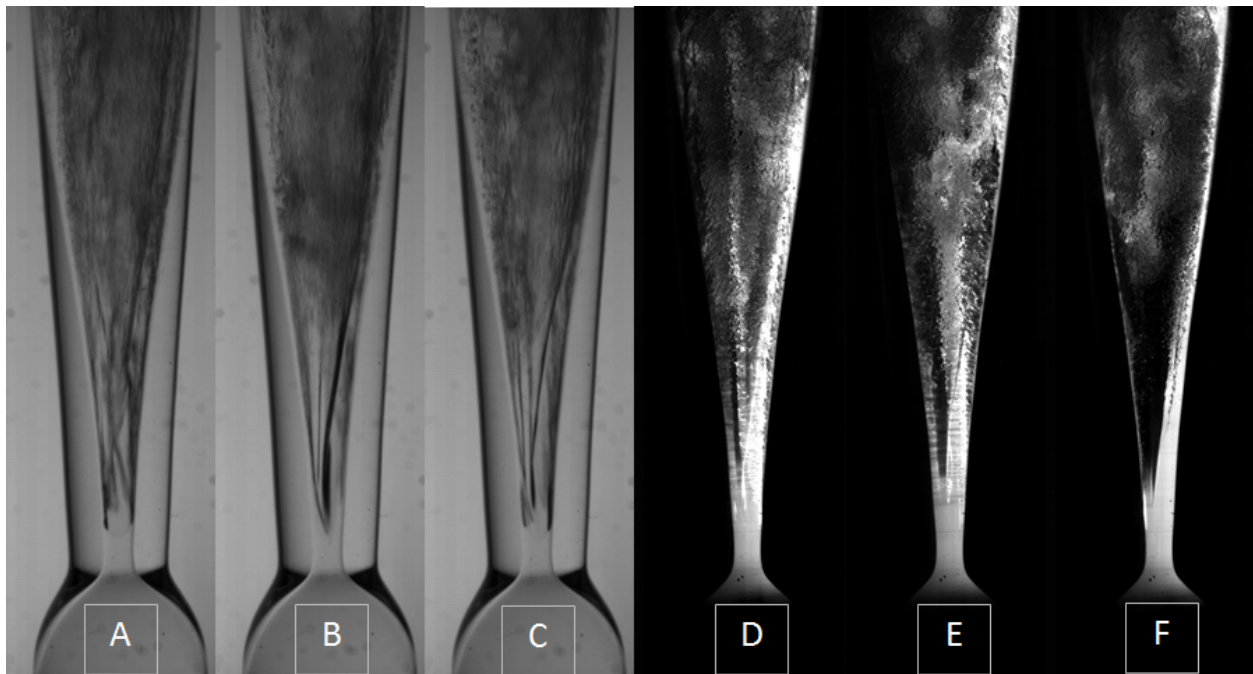


**Figure 3.28 Nozzle 8 with IFM, (A,B,C) diffuse light; (D,E,F) PLIF.**

### ***3.3.2 Nozzle 9***

Nozzle 9 featured an ogive expansion with a very sudden, small expansion, similar to the straight ogive nozzle. However, after the ogive this nozzle expanded outwards. In Figure 3.29 the images of the observed flow cycles are shown. In the first image, there was attached wall cavitation, creating a vapor cloud, starting from the location of the ogive. In this attached wall cavitation zone the orifice jet developed. The orifice jet remained approximately the size of the throat as long as it was surrounded by the vapor cloud. Once it passed the vapor cloud region it started to expand outwards, enveloping the entire nozzle cross section. In frame 60 the end of the attached wall cavitation started to descend. During that time the orifice jet expanded throughout the rest of the nozzle. In frame 205 the vapor cloud continued to descend, while the liquid and vapor left from the orifice jet coalesced into new vapor clouds. In frame 766 these vapor clouds started to descend. In frame 1363 the flow featured a mix of turbulent liquid and vapor.

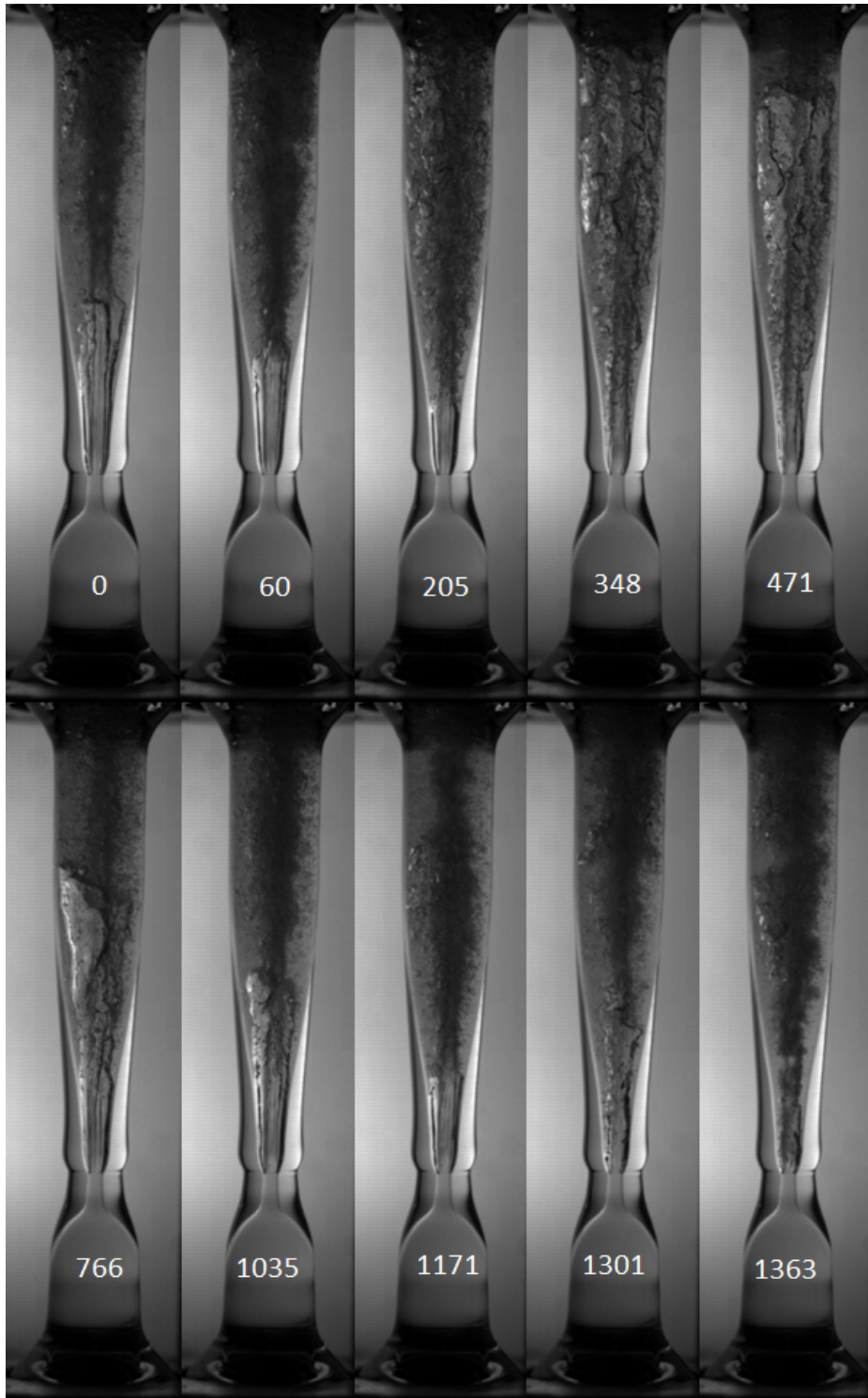


**Figure 3.29 Nozzle 9 sequence with frame numbers.**



### 3.4 Swirl Cavitation

The cavitation in this section was similar to the swirl cavitation in the radial pump inlet [8]. For this cavitation Nozzle 5 was used, as well as the Internal Flow Modifier (IFM) to rotate the flow prior to entering the nozzle. Table 5 contains the flow and visualization data for the images in this section. Using the right hand rule, the spin was positive in the direction of the flow. The results of the IFM with Nozzle 5 are shown in Figure 3.30. Directly after the throat the results were the same as without the IFM; there was the orifice jet. However, this orifice jet quickly started to expand radially. On the edges of this rotating orifice jet there was a thin water layer surrounding vapor in the bulk of the jet. Outside of the rotating jet there was a void with no liquid, most likely vapor with little to no velocity. These images indicate a very high level of void fraction.

Figure #	Nozzle	Flow Rate (g/s)	Inlet Temp (°C)	Frame Rate (Frames/Second)	Light Source	Lens
3.30	Nozzle 5 IFM	69	30	15,000	Both	60 mm

**Table 5 Flow and visualization data for 3.4 Swirl Cavitation.**

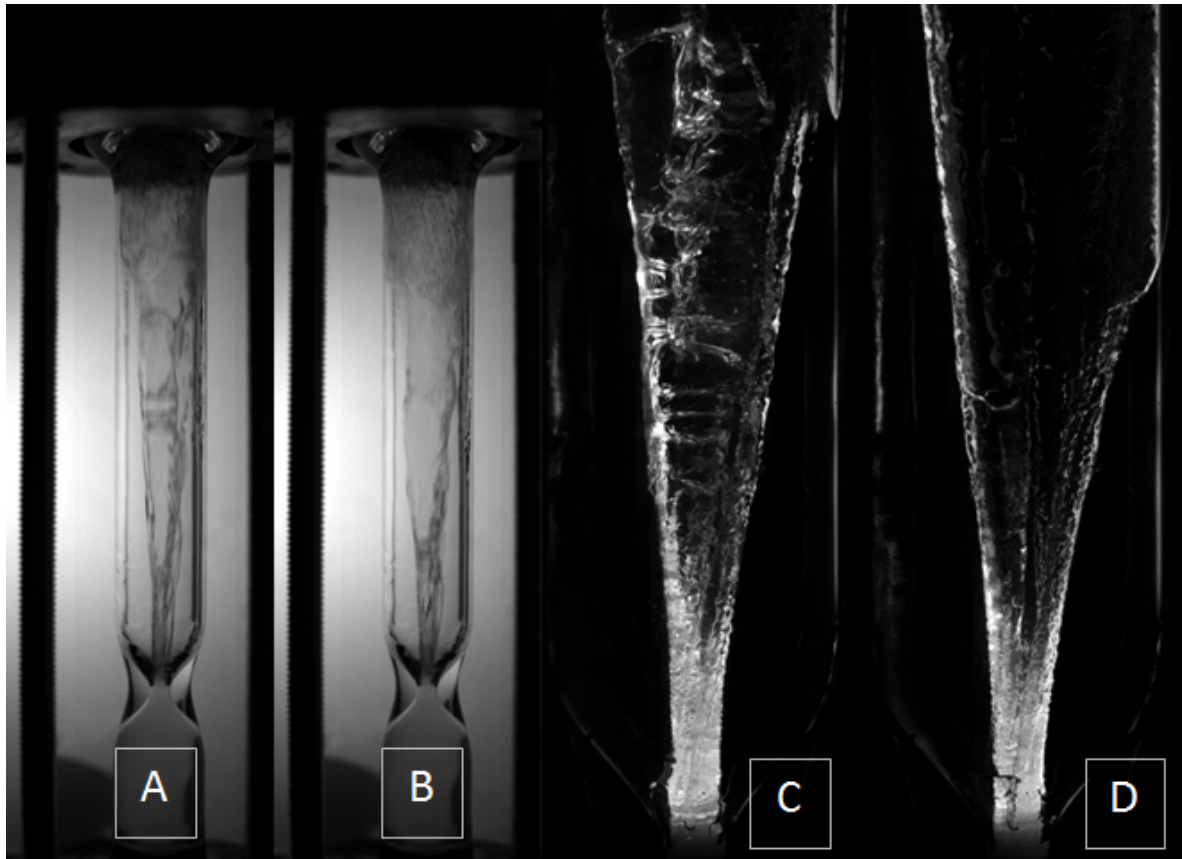


**Figure 3.30 Nozzle 5 with IFM, (A,B), diffuse light; (C,D), PLIF.**



### 3.5 Travelling Bubble Cavitation

Most of the current research was focused on the quasi-steady attached wall cavitation and shear cavitation. In order to achieve reliable and repeatable effects, it was necessary to degas the water system. This involved running the water through the osmosis filter, shown in Figure 2.1, while drawing a vacuum on the filter. However, in certain cases, before the water was degassed, observations were made of travelling bubble cavitation. These observations serve as a basis for potential future studies of travelling bubble cavitation. Table 6 contains the flow and visualization data for the images in this section.

Figure #	Nozzle	Flow Rate (g/s)	Inlet Temp (°C)	Frame Rate (Frames/Second)	Light Source	Lens
3.31	Nozzle 2	56	30	31,000	Diffuse	60 mm
3.32	Nozzle 2	56	30	31,000	Diffuse	60 mm

**Table 6 Flow and visualization data for 3.5 Travelling Bubble Cavitation.**

As discussed by Franc [2], when bubbles of gas and vapor are present in the liquid, travelling bubble cavitation occurred. In Franc's hydrofoil, the travelling bubble cavitation suppressed the attached wall cavitation. In general, this was also true for the nozzles. In the first frame of Figure 3.31, with a mass flow rate of 56 g/s, there are no observed bubbles in the inlet. In the next few images a very small bubble appeared just before the throat and started to expand. This bubble formed as the result of the decreasing pressure into the throat. The bubble continued to expand as it travelled through the nozzle; although, assuming the Bernoulli equation is valid, the pressure in the diverging portion of the nozzle was increasing. This suggests that either the bubble had reached a critical radius and was expanding explosively, or that further cavitation was occurring on the bubble. In general, travelling bubble cavitation appeared to suppress any attached wall cavitation. However, as Figure 3.32 shows, both travelling bubble cavitation and attached wall cavitation could be present at the same time. Frames 0-142 show there was a bubble slowly rising in the inlet section. This was rare, as in most cases bubbles were not seen until they were going into the throat. Once the bubble reached the throat it quickly expanded down the nozzle and induced attached wall cavitation behind it. Afterwards another bubble went through the attached wall cavitation, displacing that cavitation, but not suppressing it. In frame 571 a bubble formed that disrupted the attached wall cavitation and appeared to completely suppress it.

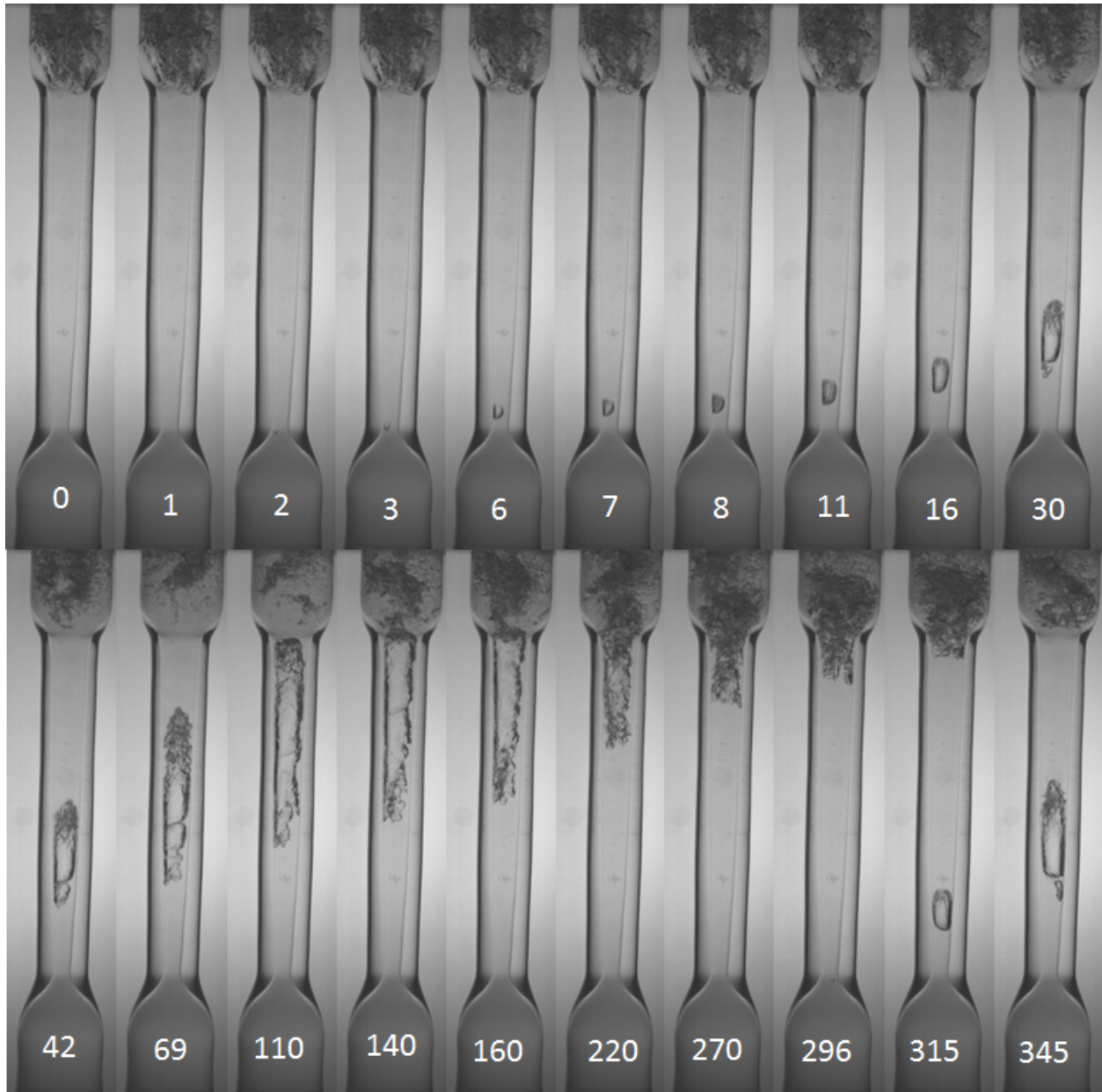


**Figure 3.31 Nozzle 2 travelling bubble sequence with frame numbers.**

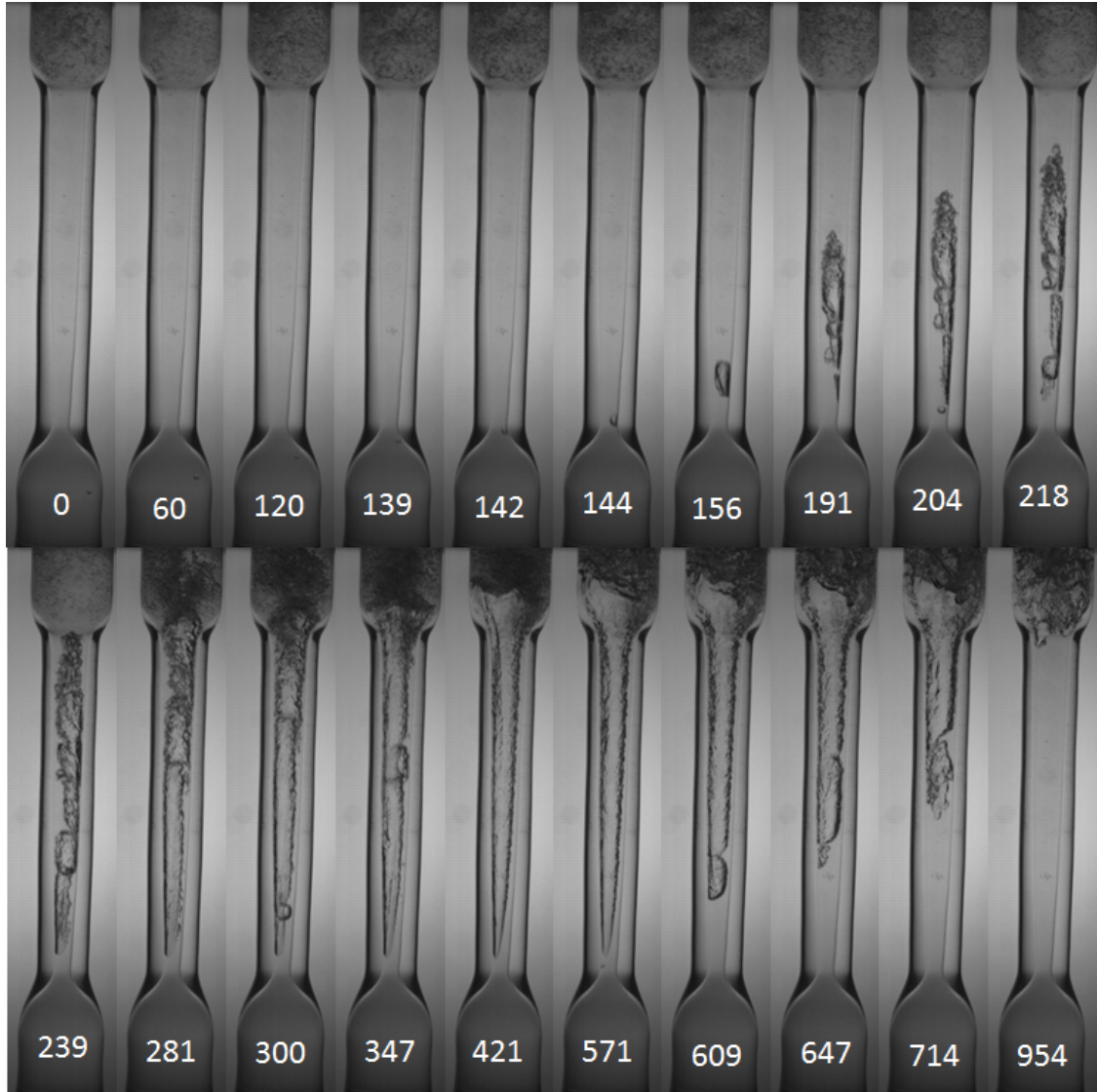


**Figure 3.32 Nozzle 2 travelling bubble sequence and wall cavitation with frame numbers.**

The positions of the bubble from Figure 3.31 were measured, and the results are plotted on Figure 3.33. The top of the bubble is defined as the upper most section of the bubble, while the bottom of the bubble is defined as the lower most section of the original bubble. The bottom of bubble 2 is the bottom of the bubble that starts to form in frame 30. The corresponding bubble velocities are plotted on Figure 3.34, where the velocities are averaged over 20 frames. At the throat the top of the bubble speeds up to nearly twice the velocity calculated from Bernoulli's equation. The velocity of the bubble then decreased as it travelled through the nozzle.

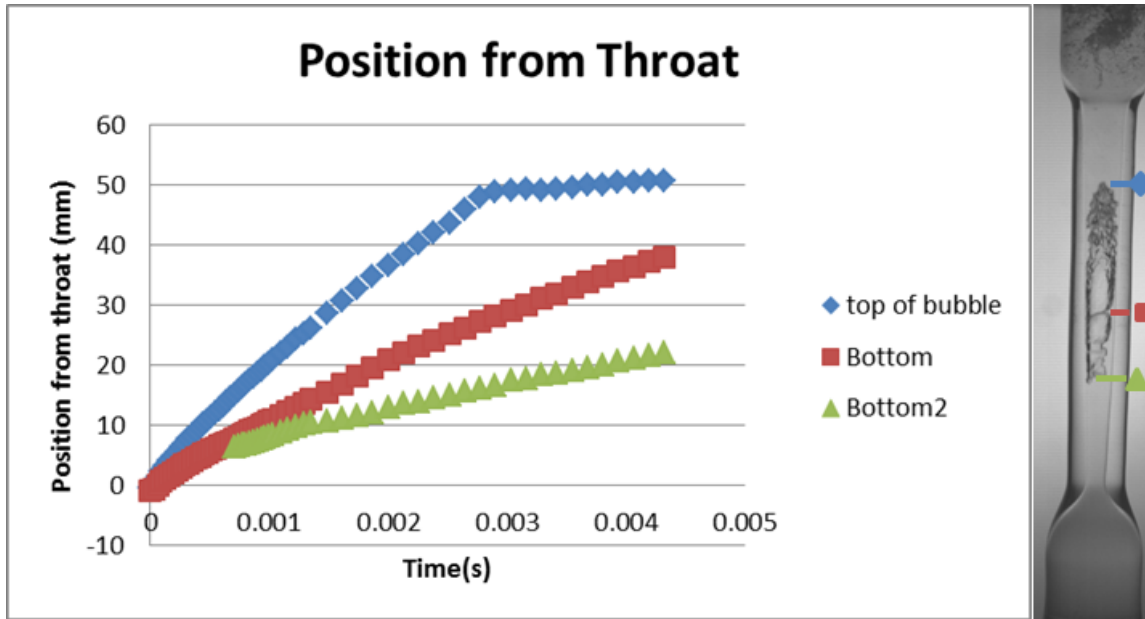


Figure 3.33 Chart of the position of the bubble with flow image.

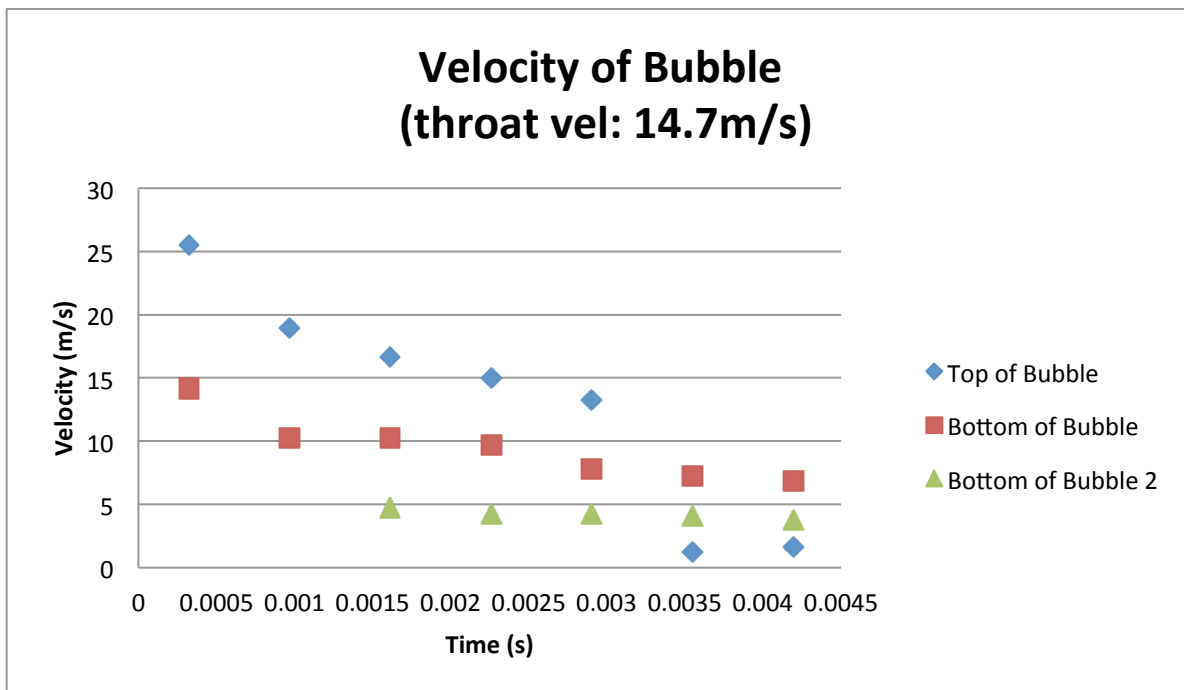


Figure 3.34 Chart of the velocity of the bubbles. Velocities averaged over 20 frames.

## Chapter 4 - Quantitative Results of Attached Wall Cavitation

In addition to qualitatively visualizing different forms of cavitation, it was necessary to be able to quantitatively describe the flow. One of the goals of the quantitative study in this thesis was to experimentally determine the void fraction and velocity to calculate flow quality. There were two nozzles, Nozzle 1 and Nozzle 2, used for these measurements. Nozzle 1 had a throat diameter of 1.7 millimeters and a divergence angle of 2.46 degrees. Nozzle 2 had a throat diameter of 2.2 millimeters and a divergence angle of 2.18 degrees. Different sets of data, with different imaging methods are described in Table 7.

Nozzle	Set Name	Tested	Lighting	Frame Rate
Nozzle 1	Image Set 1	Void	PLIF	20,000
Nozzle 1	45° Angle	Void	PLIF - 45°	40,000
Nozzle 1	Image Set 2	Void/ Velocity	PLIF	70,000
Nozzle 1	Green Component	Void	Diffuse	Still images
Nozzle 2	Nozzle 2	Void/ Velocity	PLIF	20,000

**Table 7 Testing Sets for Void Fraction and Velocity.**

### 4.1 Void Fraction Measurements

The void fraction is the cross sectional area of the vapor divided by the total cross sectional area. Three different methods were used to find the void fraction: using a vertical laser sheet through the middle of the nozzle, angling the laser sheet in a 45 degree angle, and using a fiber optic light source and measuring the attenuation of light intensity.

#### *4.1.1 Preliminary Testing*

As discussed in Section 2.4, the void fraction can be measured by seeding the liquid with Rhodamine B dye, and using a Yag laser as well as a Fluorescent filter to observe the liquid phase. Shown in Figure 4.1, there were two laser orientations: a vertical light sheet and 45° angle light sheet. The vertical light sheet cut through the middle of the nozzle. The 45° angle light sheet was oriented so that it showed the entire cross section. The advantage of the 45° angle was that it could took the void fraction of the entire cross section. The vertical light sheet provided more optically clear images and it allowed viewing over the entire length of the nozzle.

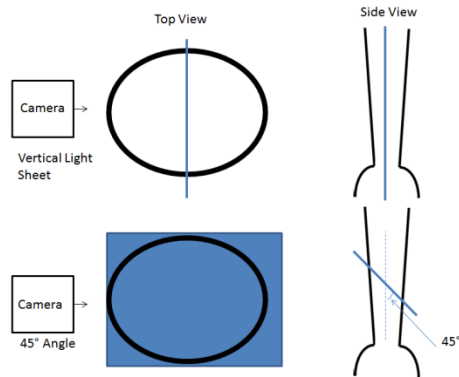


**Figure 4.1 Laser orientation.**

Once the raw images of the flow were taken they were processed using Matlab, using the method described in section 2.5, and the code given in Appendix B. Figure 4.2 shows a set of images being converted in the Matlab code. The camera had an 8 bit grayscale sensor, meaning that each pixel had a value between 0, no light, and 255, full light. These raw images were then converted to a binary value. The threshold value, shown between 60 and 140, was the cutoff point; if the pixel had a value below the threshold it became 0, black, and if it was above the threshold it became 1, white. These three images were part of a batch of 48 images. Each image was split into four sections with a threshold of 100, and the resulting void fraction measurements are shown in Figure 4.3. This shows that even in one batch of images there was a large deviation in the void fraction based on changes in flow itself. Images A, B, and C were taken with the same flow conditions, and yet they have different void fractions. These images also illustrate how the selection of the threshold value affected the measurement of the void fraction. In image A, the light sheet did not cleanly slice through the middle of the vapor cloud; therefore the vapor has a higher light intensity than the other images. As the threshold was increased, the measured vapor increased. In image B and the no flow image, the threshold did not have much of an effect until 120, where the liquid region illumination was below the threshold. In image C, the threshold value had little effect on the measured vapor. Figure 4.4 shows the average void fraction of the entire set of images while changing the threshold level. This shows that in general larger the threshold value, the larger the measured void fraction, with the exception in the case where the 140 threshold affected the no flow image.

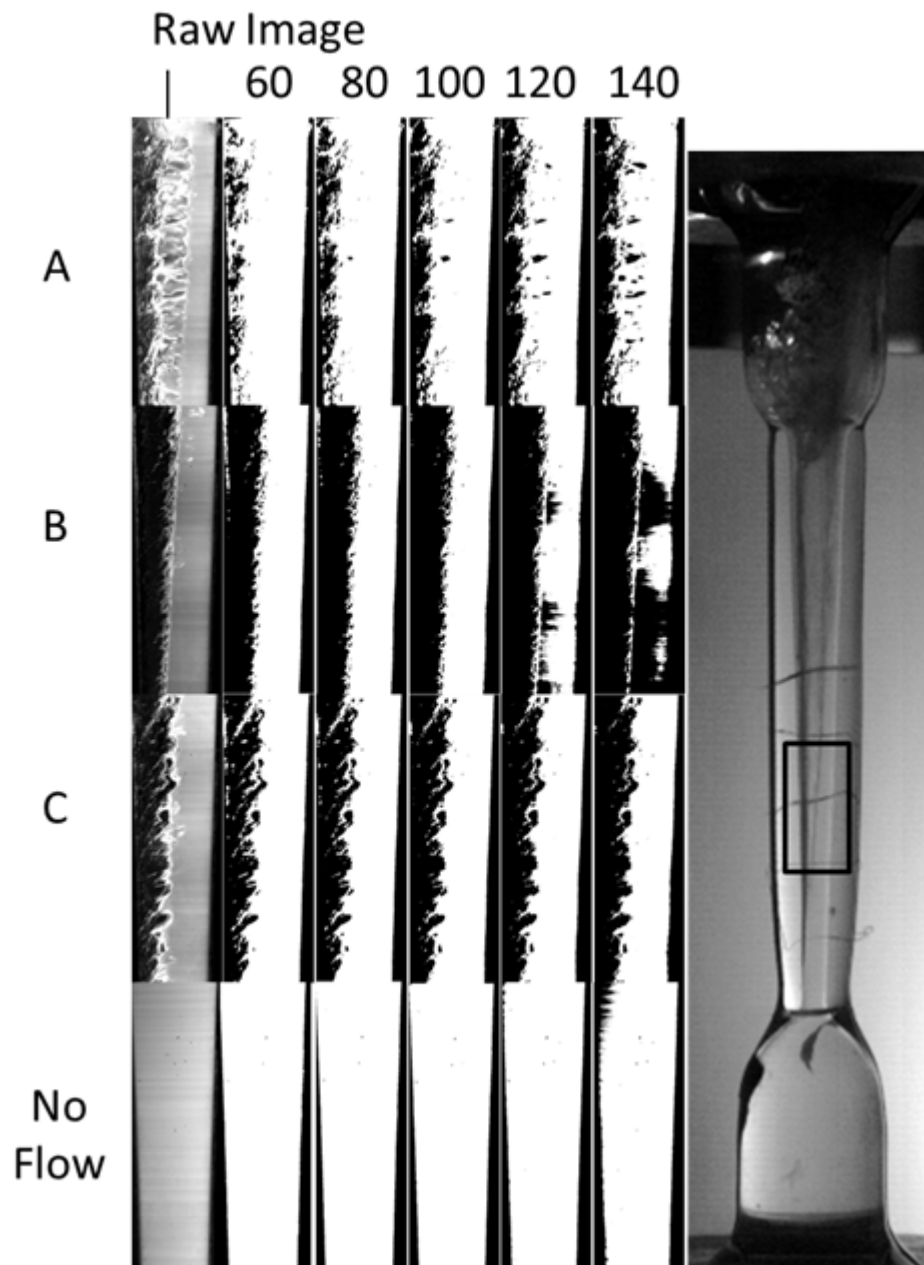
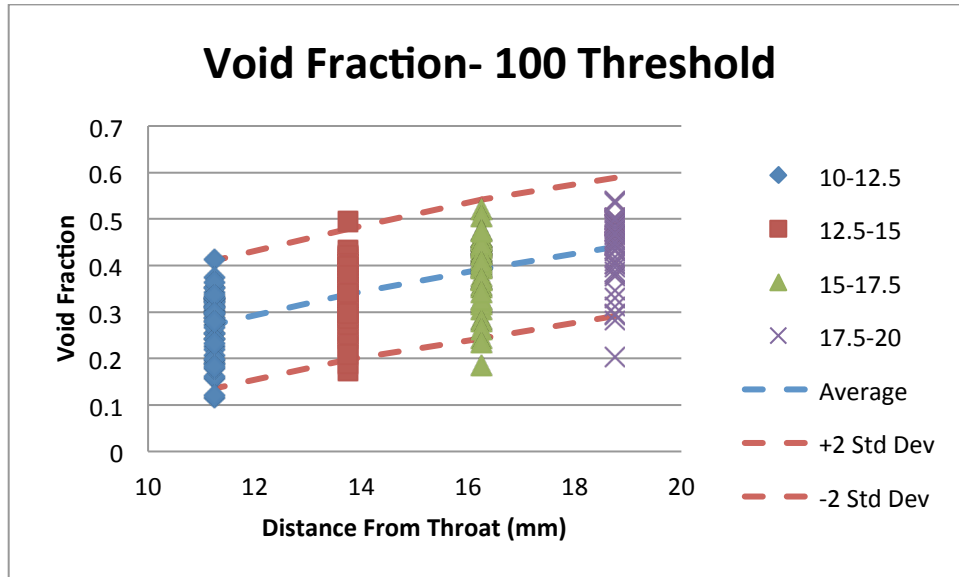
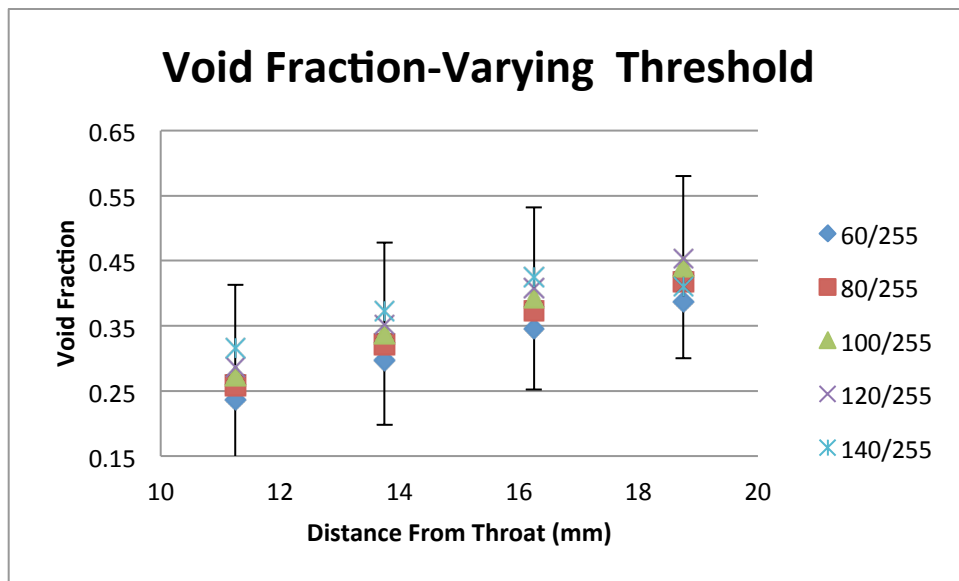


Figure 4.2 Nozzle 1, varying threshold images.



**Figure 4.3 Nozzle 1, Void Fraction- 100 Threshold.**



**Figure 4.4 Nozzle 1, Void Fraction- Varying Threshold.**

The third method involved using a diffuse fiber optic light source and a digital camera. This method was based on interpolating the light intensity of the cavitation between liquid and gas. As opposed to the high speed camera, the digital camera gave images in RGB. The red, green, and blue color values were separated into black and white images. From Figure 4.5, the water with Rhodamine B dye gets its pink color from the dye blocking out color in the green spectrum. The images with only gas in the nozzle, only liquid in the nozzle, and cavitation in the nozzle are shown in Figure 4.6. For the measurements the image was broken up into sections.



Then the void fraction was calculated as:  $\text{Void Fraction} = (\text{CavG} - \text{LiquidG}) / (\text{GasG} - \text{LiquidG})$ ; where CavG was the average green intensity value of the section with cavitation, liquidG was the green intensity value of the section with liquid, and GasG was the green intensity value of the section with gas.

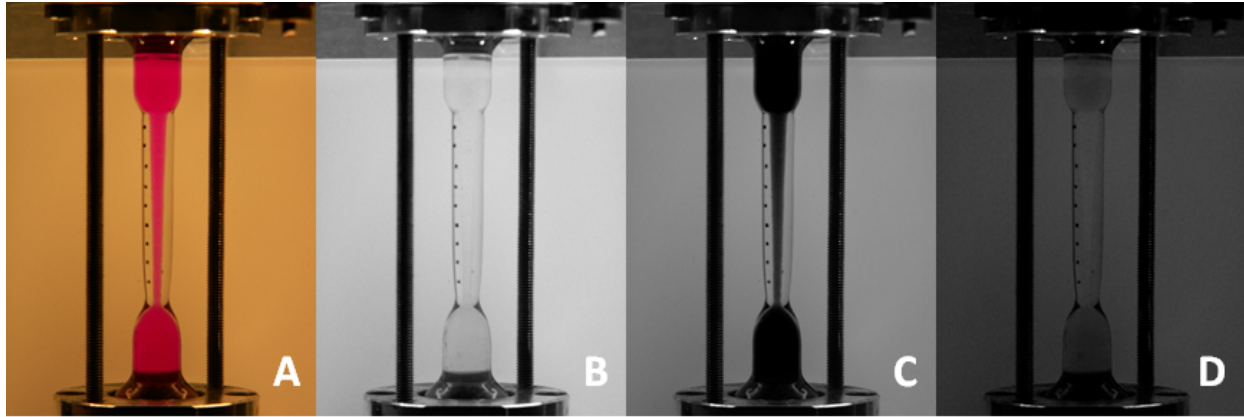


**Figure 4.5 (A) Original Image, (B) Red Component, (C) Green Component, (D) Blue Component.**

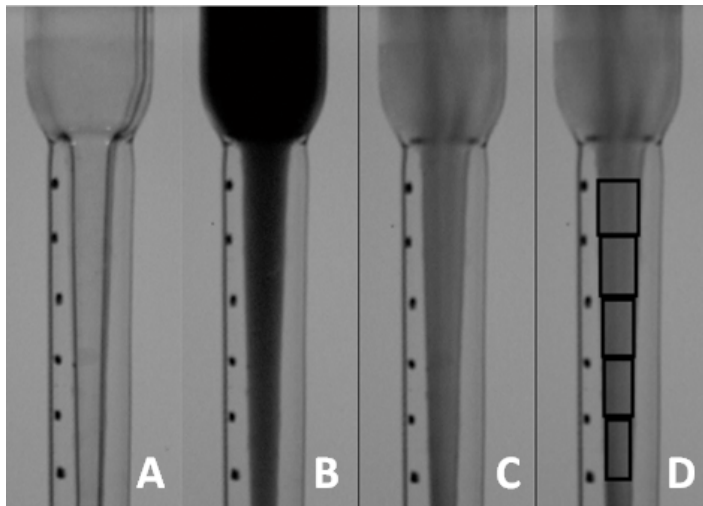


**Figure 4.6 (A) Pure Gas, (B) Pure Liquid, (C) Cavitation, (D) Cavitation with sections.**

#### ***4.1.2 Nozzle 1***

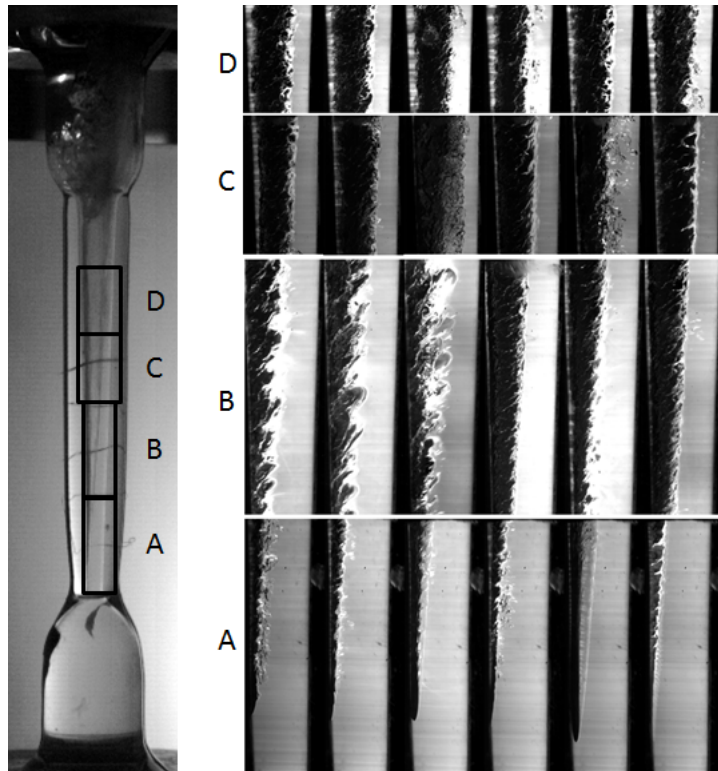
The void fraction and velocity measurements were taken in data sets with different flow conditions, shown in Table 8. The first measurements, image set 1, of the void fraction for Nozzle 1 were taken using the vertical sheet method. These measurements were taken of the laser induced cavitation, referred to in section 3.1.3, with an inlet temperature of 30°C and a

mass flow rate of 39 grams per second. There are four sections in the graph, corresponding to each of the four sets of images. The Matlab code divided each set of images into 12 subsections and each point on the graph represents the average void fraction values of those subsections.

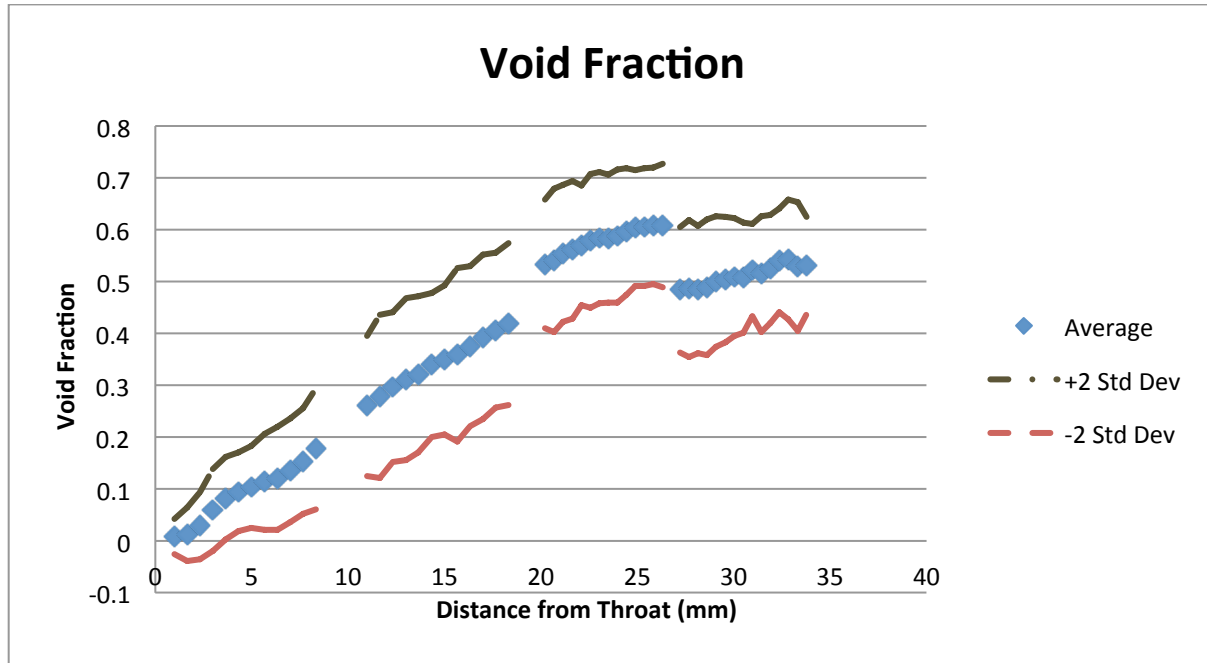
These results showed that once the cavitation initiated it would grow at an approximately linear rate of increase until 20 mm downstream of the throat. After 20 mm downstream of the throat the rate of increase of the void fraction decreased.

	Figure #	Inlet Temp (°C)	Mass Flow (g/s)	Inlet Pressure (psia)
Image Set 1	4.7	30	39	46
45° Angle	4.9	30	39	46
Image Set 2	4.11	30	39	46
Image Set 2	4.12	40	42	46
Image Set 2	4.26	30	45	45
Green Comp	4.14	40	39	40
Green Comp	4.14	50	42	47

**Table 8 Flow Conditions for Nozzle 1.**



**Figure 4.7 Nozzle 1, image set 1, void fraction, Laser Induced Cavitation.**



**Figure 4.8 Void fraction measurements for image set 1.**

The 45° angle light sheet method was used to corroborate the two-dimensional vertical plane measurements. Figure 4.9 shows some of the images using the 45 degree sheet, centered at 14 mm from the throat. Figure 4.10 graphs the results of the 45° angle light sheet images as well as image set 1. Since these results of the 45° angle light sheet images fell within two standard deviations of the averaged values of image set 1, it confirmed that the two measurement methods gave similar results.

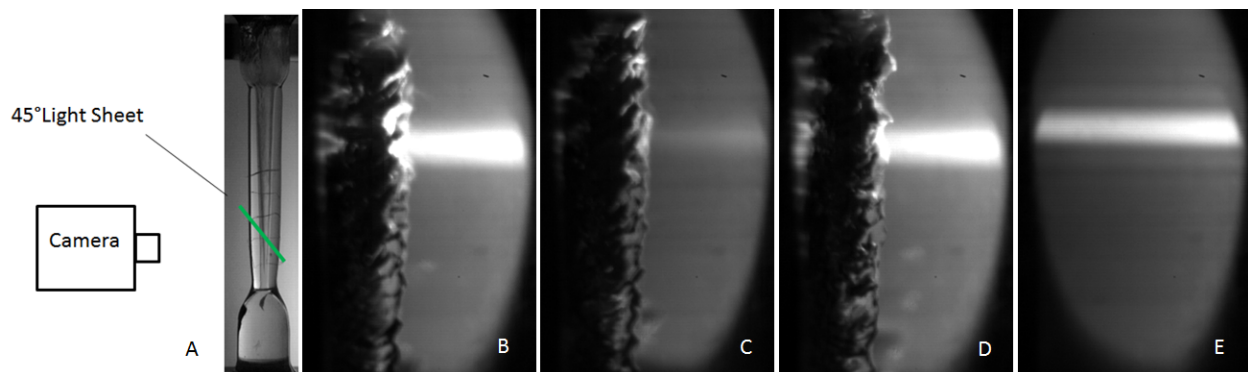


**Figure 4.9 Nozzle 1, Side view showing 45° angle light sheet; (A) side view of entire nozzle; (B,C,D), images with cavitation for void fraction; (E), no flow image.**

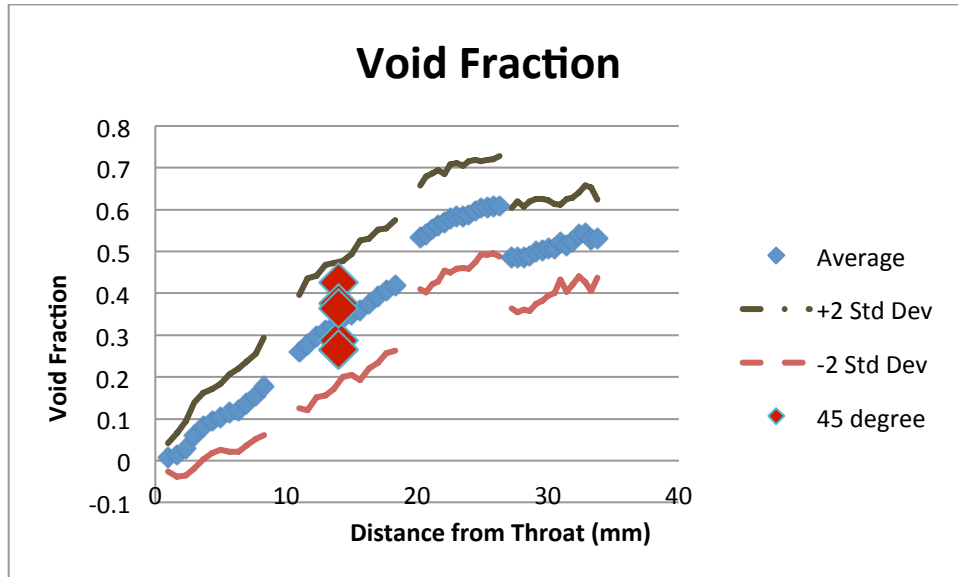


**Figure 4.10 Nozzle 1, void fraction of image set 1 and 45° angle light sheet.**

The next round of testing, image set 2, used PLIF to get both velocity and void fraction measurements. Figure 4.11 and Figure 4.12 show a sample of the set of images taken for the laser induced 30 °C and the 40 °C testing conditions. The results of image set 1 and 2 are shown in Figure 4.13. In image set 2, the void fraction measurements for the laser induced 30 °C and the 40 °C test conditions were nearly identical, except at 40 mm downstream of the throat. At this location a recirculation region developed in the laser induced flow condition. As shown in Figure 4.11, row D, the recirculation region did not appear in every image, which resulted in a large standard deviation. With the exception of 20-27 mm section in image set 1, all of the void fraction measurements were within two standard deviations of each other.

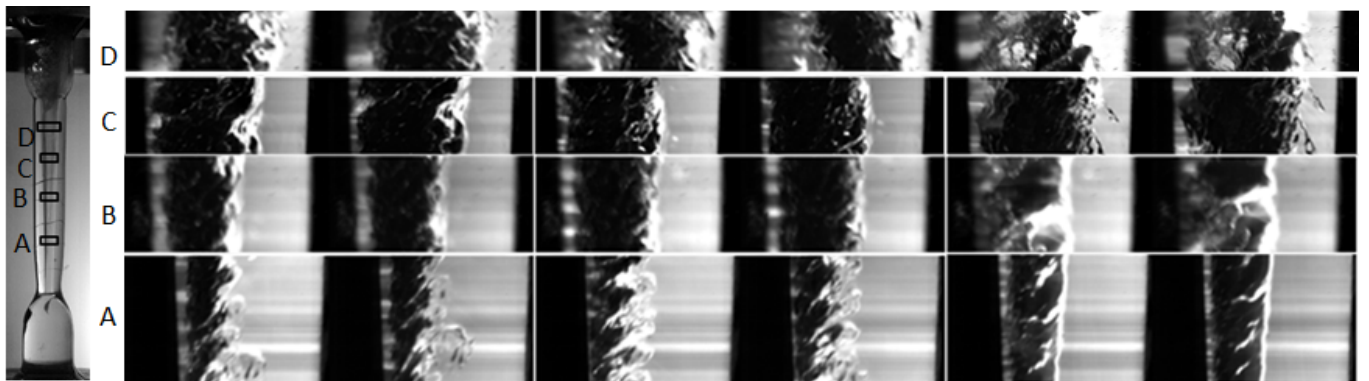


**Figure 4.11 Nozzle 1, Laser Induced Cavitation, Image Set 2.**

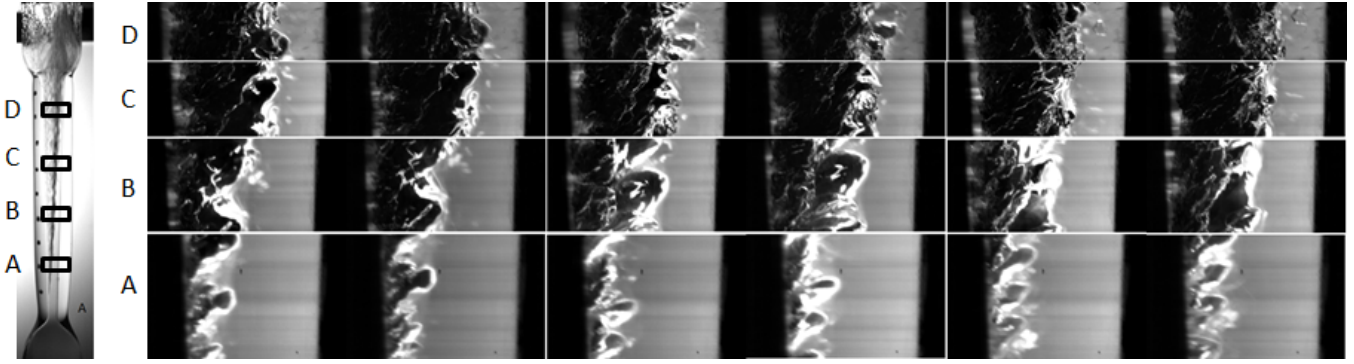


**Figure 4.12 Nozzle 1, 40° C, Image Set 2.**

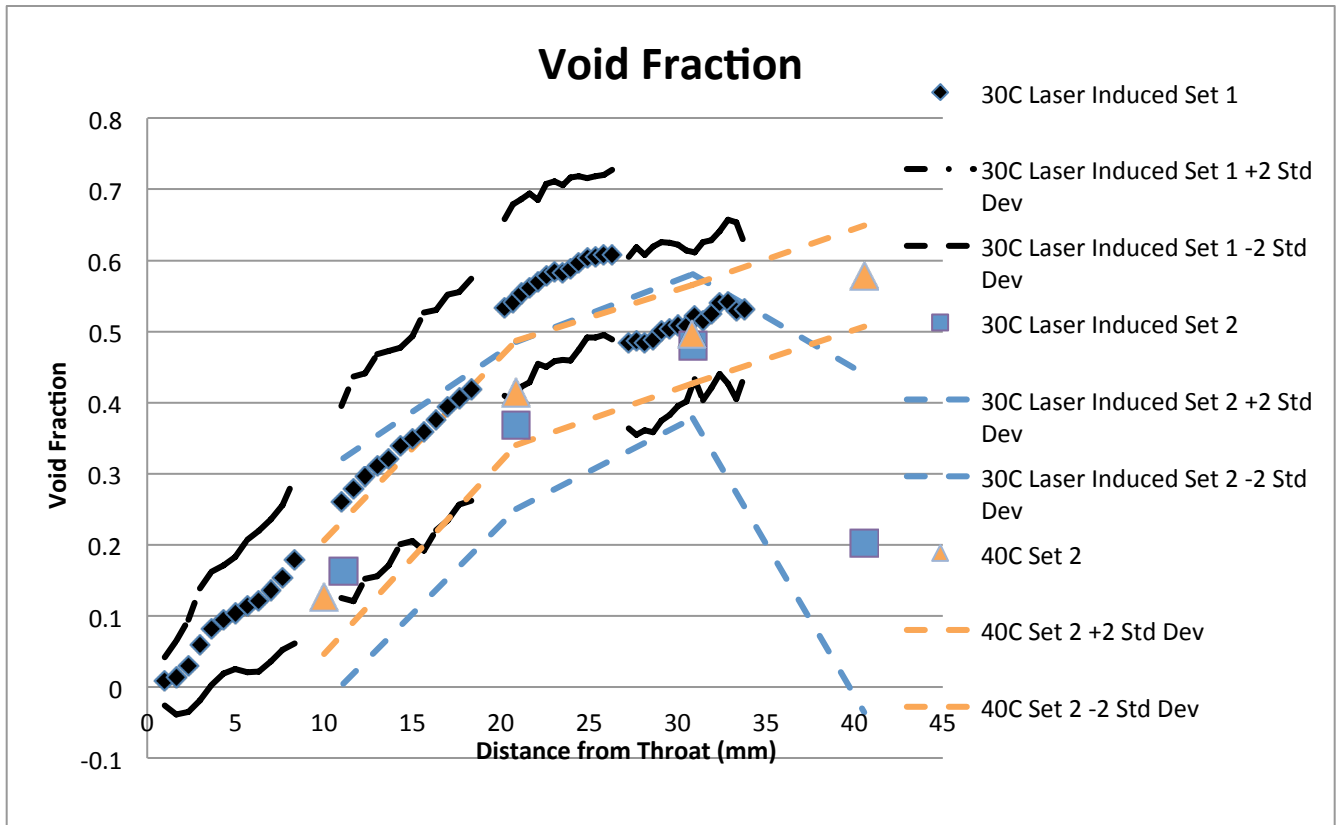


**Figure 4.13 Nozzle 1, Image Set 1 and 2, Void Fraction.**

The last method for measuring the void fraction separated the green light intensity component from images taken by a digital camera. Figure 4.14 shows the images for the three tests. Two of the tests were run at 40 °C, with the other test at 50 °C. The results of the green component tests and image set 2 are shown in Figure 4.15. The green component tests show an approximately linear expansion from the beginning. The 40 °C tests had a recirculation region similar to that found in the laser induced 30 °C from set 2. It is uncertain why at 40 °C the green component tests showed a recirculation region, where image set 2 did not.

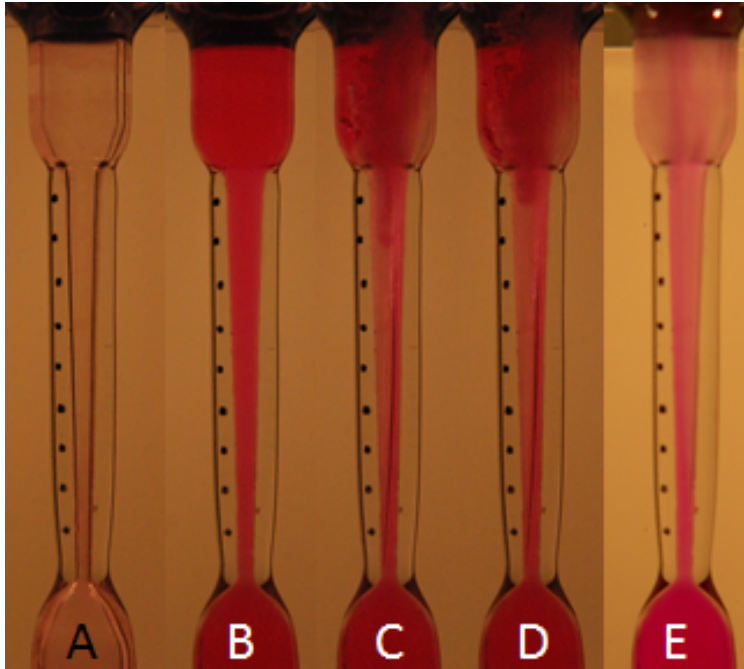


Figure 4.14 Nozzle 1, Digital Camera, (A) Air, (B) liquid, (C,D) 40 °C, (E) 50 °C.

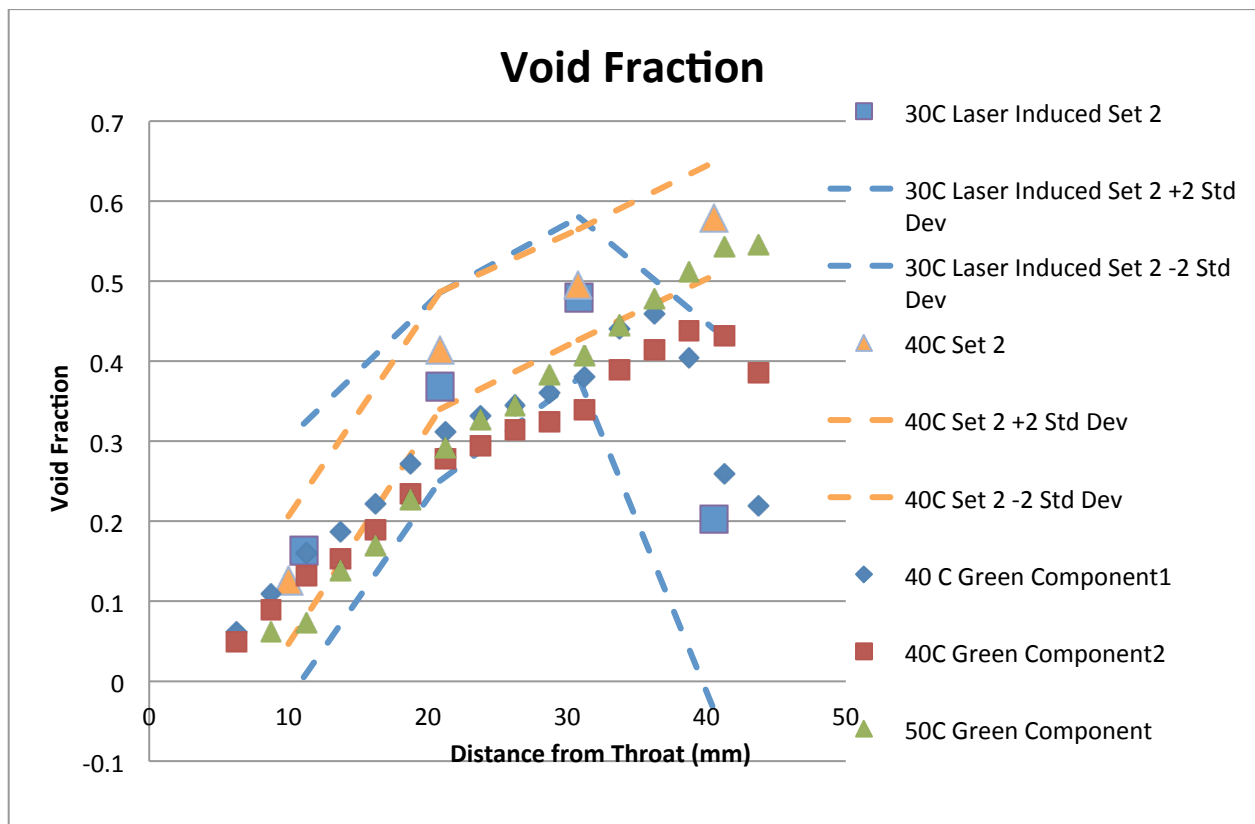


Figure 4.15 Nozzle 1, void fraction, results of green component and image set 2.

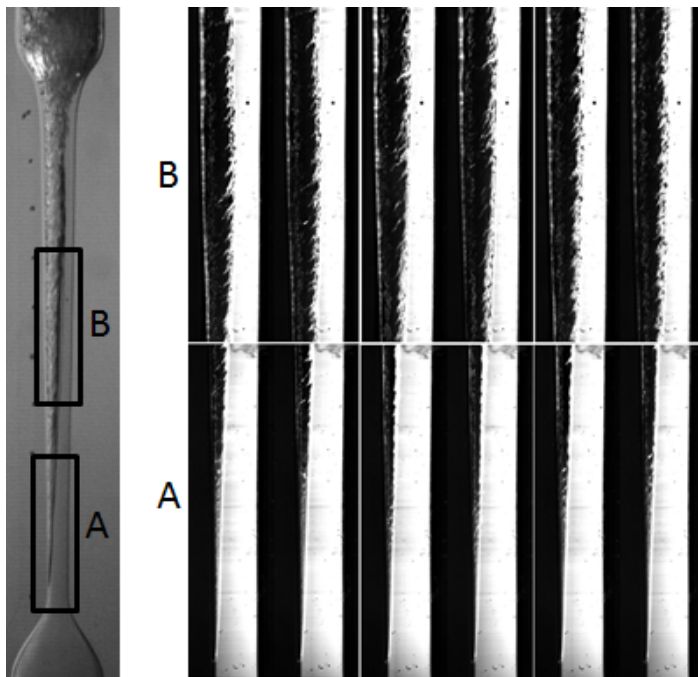


### 4.1.3 Nozzle 2

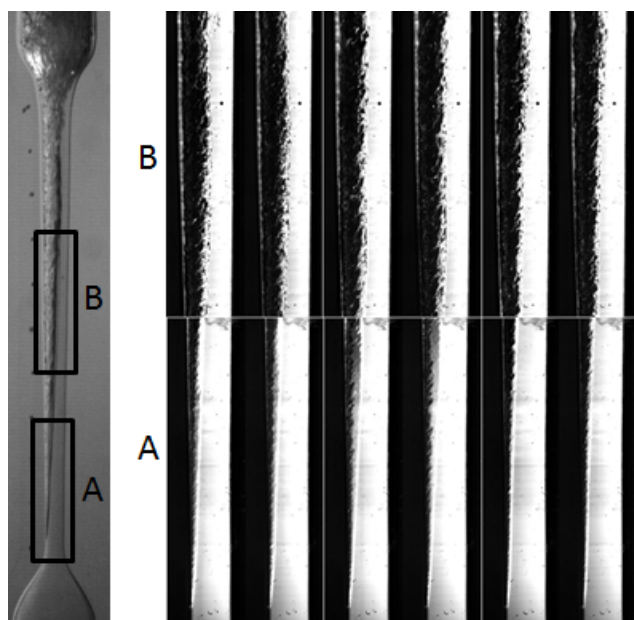
Table 9 shows the four operating conditions that were tested using Nozzle 2. Three conditions are at an inlet temperature of 30 °C and mass flow rates of 48, 84, and 98 grams/second; shown in Figure 4.16, Figure 4.17, and Figure 4.18 respectively. These all had two sets of PLIF images, 0-15 mm and 20-35 mm downstream of the throat. The fourth test condition was 84 g/s at 50 °C, shown in Figure 4.19. There was an additional overlapping image at 10-25 mm from the throat.

	Figure #	Inlet (°C)	Mass Flow (g/s)	Inlet Pressure(psia)
Nozzle 2	4.16	30	48	15
Nozzle 2	4.17	30	85	42
Nozzle 2	4.18	30	97	55
Nozzle 2	4.19	50	84	43

**Table 9 Flow Conditions for Nozzle 2.**



**Figure 4.16 Nozzle 2, 48 g/s, 30 °C.**



**Figure 4.17 Nozzle 2, 85 g/s, 30 °C.**

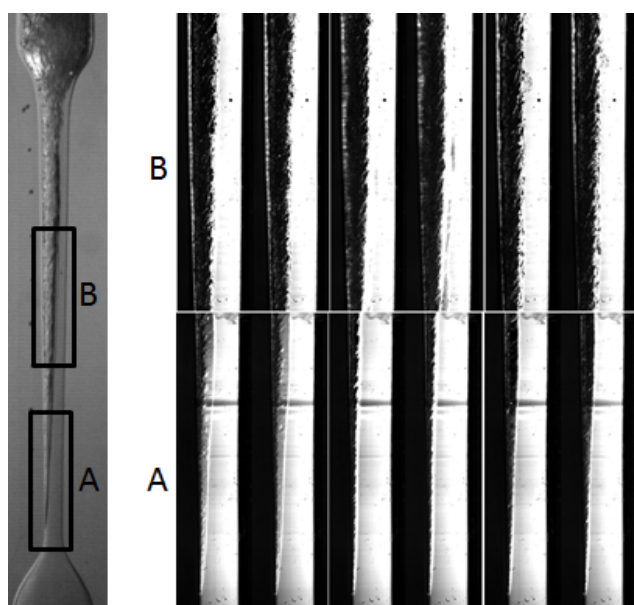


**Figure 4.18 Nozzle 2, 95 g/s, 30 °C.**



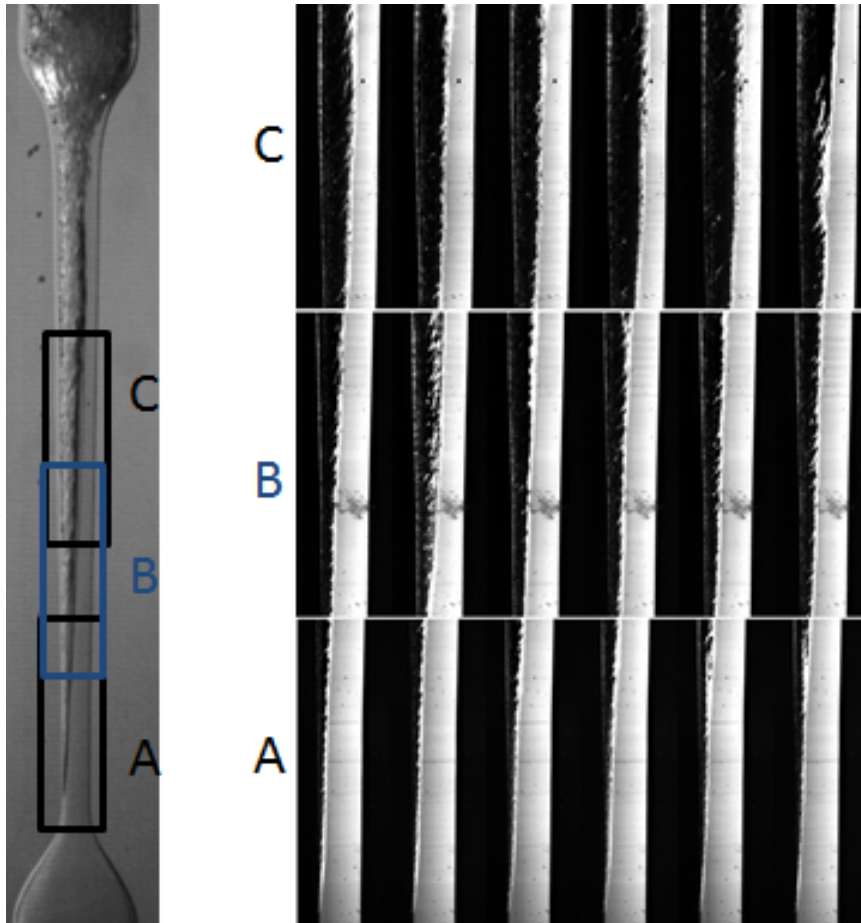


**Figure 4.19** Nozzle 2, 84 g/s, 50 °C.

For all of these test conditions, which varied the mass flow rate and the inlet temperature, the images appeared to have very similar attached wall cavitation. The measurements, Figure 4.20, confirm the visual observation. The void fraction in attached wall cavitation was not dependent on the mass flow rate, nor was it dependent on the inlet temperature.

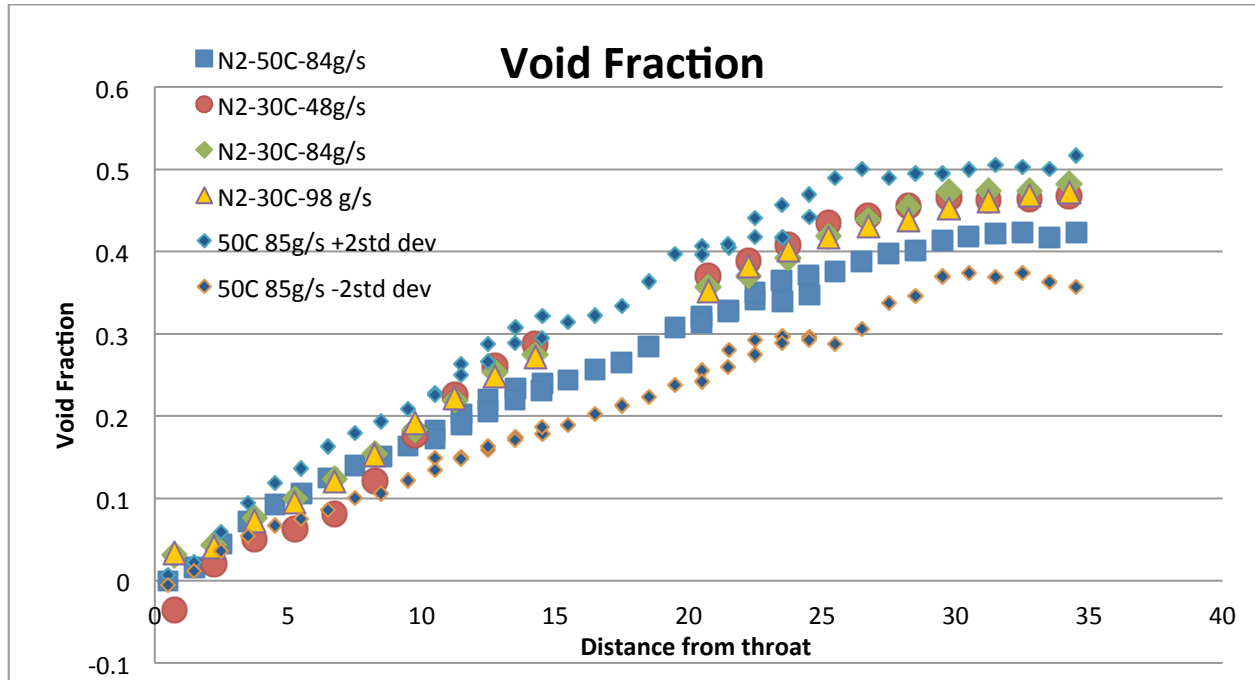


**Figure 4.20 Nozzle 2, void fraction results.**

## 4.2 Velocity Measurements

In order to obtain accurate velocity measurements, distinct movements must be clearly visible. In many single phase flows, seed particles are used to track the fluid movement. The seed particles are illuminated, tracked, and the velocities are measured by observing the particle displacements. In the case of cavitation, seed particles could not be used due to the possibility that they would interfere with the cavitation flow. Therefore, measurement of the velocity relied on finding the distance travelled on features of the cavitation structure it. The predominate cavitation feature measured was the vapor- liquid interface. This velocity of the vapor- liquid interface was assumed to be the vapor velocity.

### 4.2.1 Preliminary Testing

Unlike measuring the void fraction, measuring the velocity can make use of images captured with different lighting methods; laser or diffuse light. The dual Yag laser enabled two synchronous images to be captured, with an adjustable time interval between them. The main advantage of using the laser light was that the images that were used for the void fraction measurement could also be used for the velocity measurements. The laser light pulses are also

very short duration (around 5  $\mu$ s), giving similar results as a fast shutter speed on the camera, which resulted in a sharply defined image. The disadvantage of using the laser light was that the dual Yag laser pulsed every 30 Hz, which resulted in many blank frames between pulses in the captured video. By using diffuse light, a large set of sequential images could be captured, with no blank images, which decreased the processing time. However, the diffuse light images could not be used for void fraction measurements and were also not as sharp. Thus, the laser was used as the light source for the velocity measurements.

With the dual YAG laser illuminating the cavitation, the pixel shift of the cavitation features, the vapor-liquid boundary, was measured. This pixel shift was converted to the distance (in meters) travelled by the cavitation features. The velocity (m/s) was calculated by dividing the distance travelled by the time between the images. Assuming that the velocity of the liquid and the vapor are not the same, the vapor-liquid boundary velocity could be either the liquid or the vapor. In this thesis the vapor-liquid velocity was assumed to be the vapor velocity.

To measure the pixel shift, a Matlab code, given in Appendix B, was developed to use a linear correlation method. With the Matlab code, the quality of the image was critical, and background noise needed be reduced. Figure 4.21 shows two sequential PLIF images, 14.3  $\mu$ s apart. A graph of the Matlab cross correlation result is shown on Figure 4.22. The cross correlation coefficient peak shows the similarity and the location gives the relative shift between the two images. The x axis is the relative pixel shift. The y axis is the strength of the correlation, 0.00 being no correlation and 1.00 being a perfect correlation. With these images the maximum correlation peak was near zero, which was a result of the two images being very similar. In order to refine the results the images had to be cropped down, reducing the background noise to focus on the feature shift. The results are shown in Figure 4.23. By focusing on the cavitation the correlation peak appeared at 40 pixels, with a correlation coefficient of about 0.5. While this was a weak correlation, it did correspond to the 39 and 40 pixel shift manually measured. By further cropping the image, Figure 4.24, the peak correlation coefficient rose to about .57, which was well above adjacent peaks.

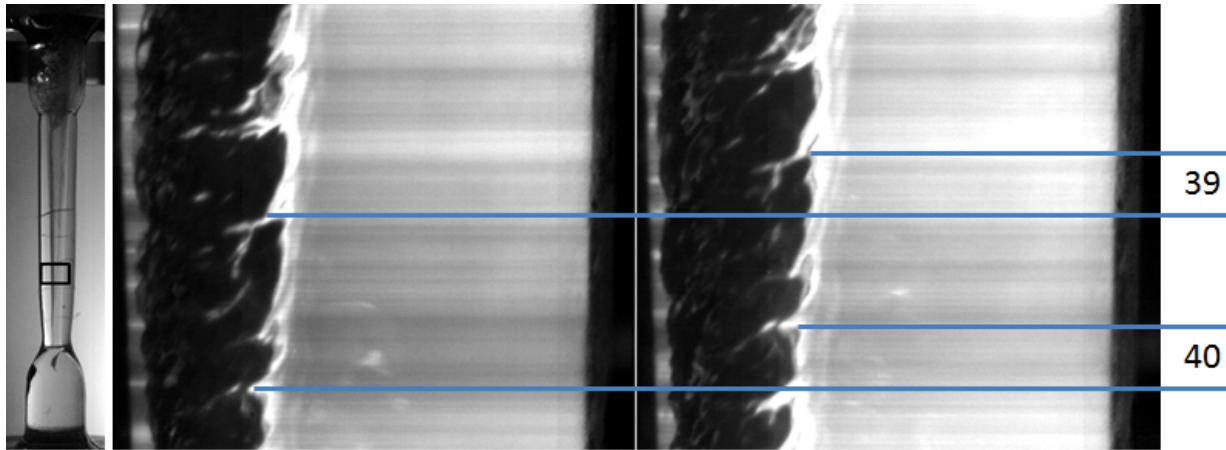


**Figure 4.21 Nozzle 1; PLIF; 70,000 frames / second**

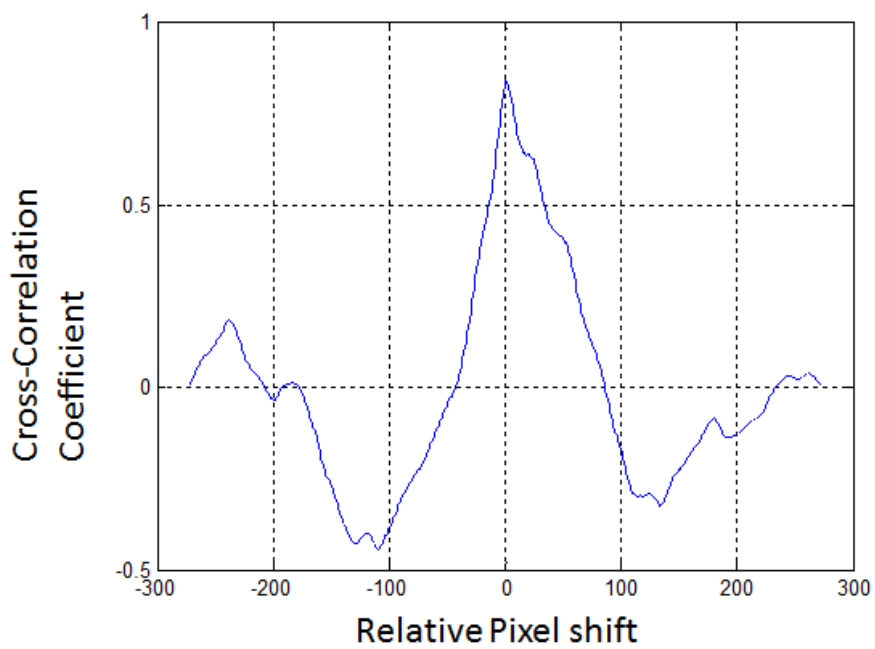


**Figure 4.22 Correlation coefficients of images from Figure 4.21.**

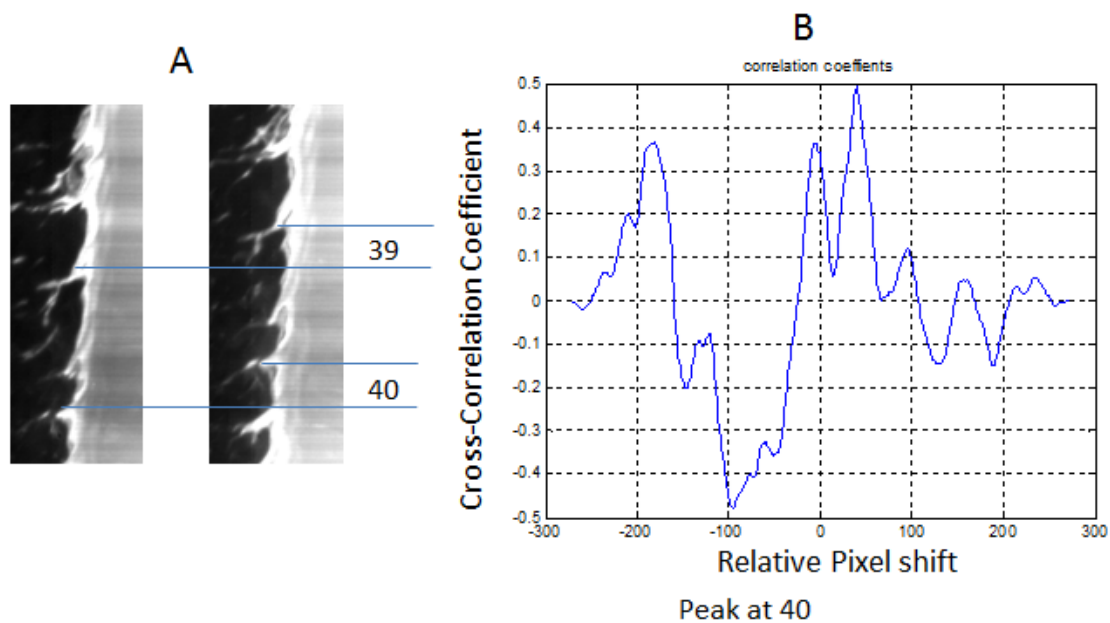


**Figure 4.23 (A) Cropped Images, (B) Correlation graph.**

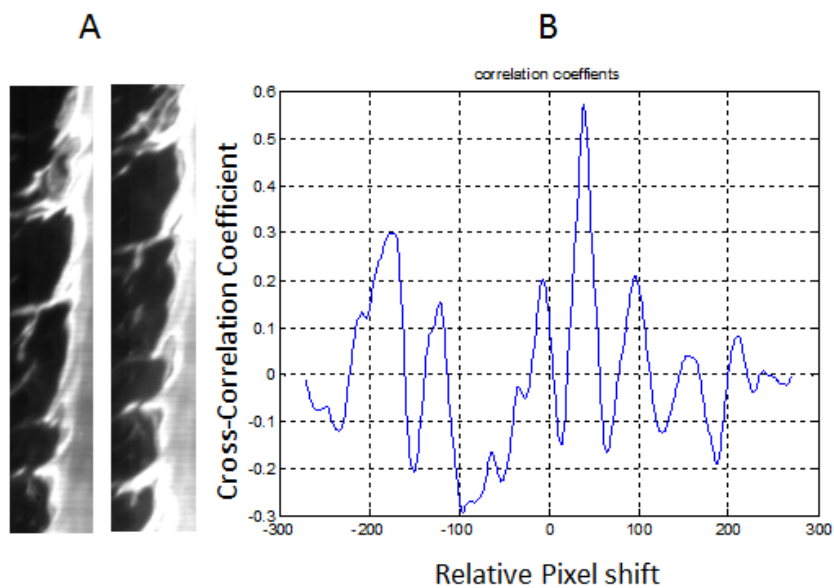


**Figure 4.24 (A) Further Cropped Images, (B) Correlation graph.**

### 4.2.2 Nozzle 1

With the proper method in place, batch images were taken and processed to measure the vapor velocity. Vapor velocities were measured for the three conditions: laser induced 30 °C, 30 °C, and 40 °C. Figure 4.11 shows a sample of the image pairs from the laser induced flow condition. These images were taken at 70,000 frames per second with mass flow of 39.5 g/s and inlet temperature of 30 °C. The average velocities are shown in Figure 4.25, with upper and lower bands of two standard deviations. The throat velocity was 10.46 m/s. When the vapor formed it had a velocity of about 23.4 m/s. Downstream, the vapor velocity decreased to about 19.6 m/s.

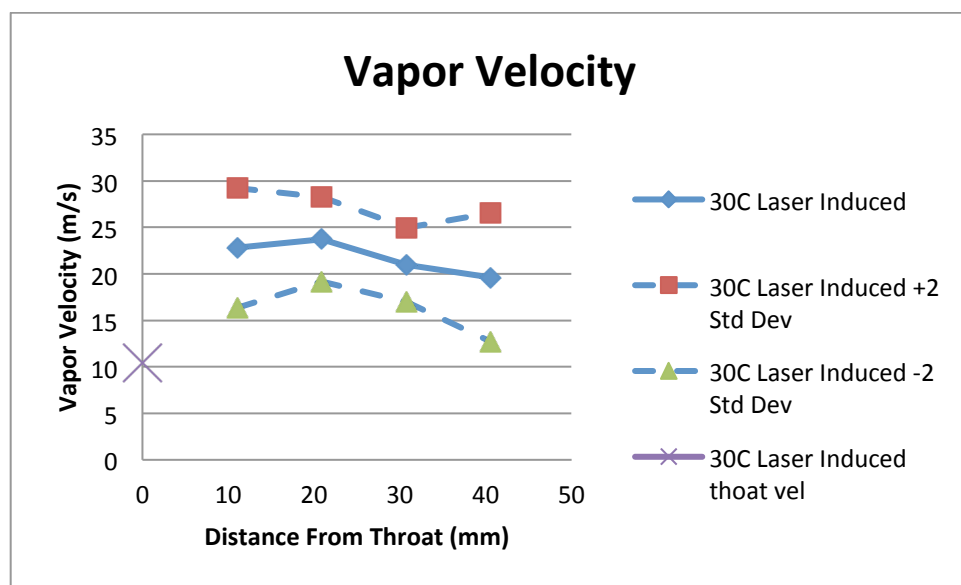


**Figure 4.25 Nozzle 1, Laser Induced Cavitation Vapor Velocity.**

A sample of images with an inlet temperature of 30 °C and a mass flow rate of 45.3 g/s are shown in Figure 4.26. These images were taken at 70,000 frames per second. The velocity results are shown in Figure 4.27. The throat velocity was 11.97 m/s. The vapor velocity of the cavitation started around 19.3 m/s and decreased to around 17.1 m/s.

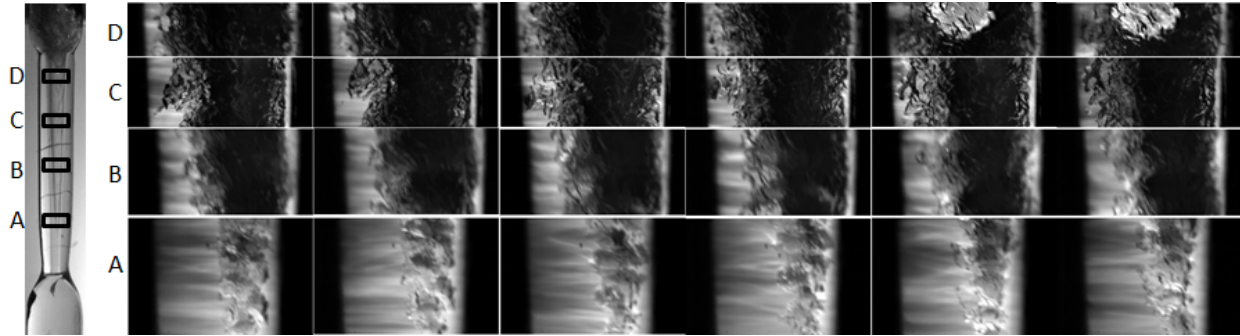


**Figure 4.26 Nozzle 1, 30 °C, PLIF**

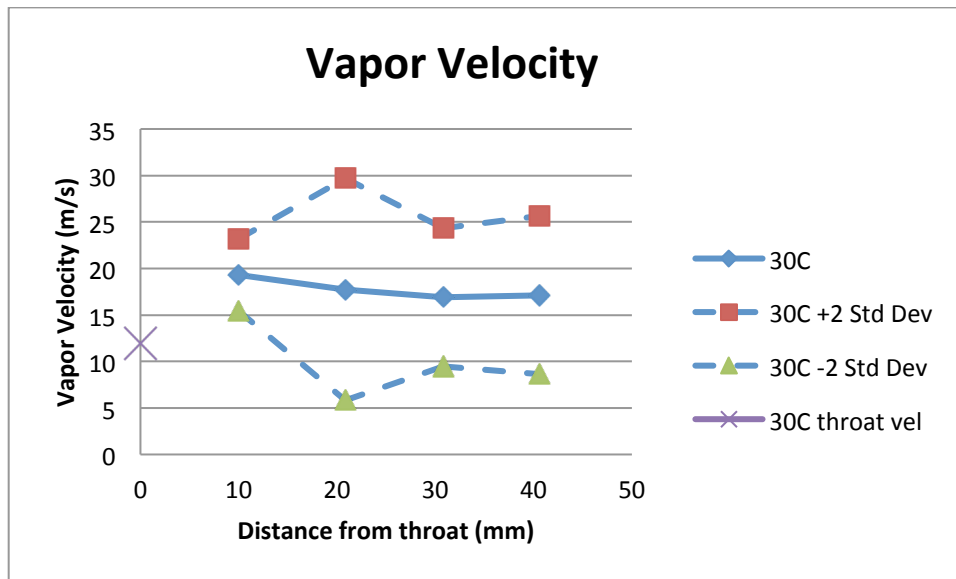


**Figure 4.27 Nozzle 1, 30 °C Vapor Velocity.**

The images of the last flow condition, taken with a temperature inlet of 40 °C and a mass flow rate of 42.3 g/s, are shown in Figure 4.12. These images are also captured at 70,000 frames per second. The profile of the 40 °C cavitation was similar to the laser induced 30 °C profile. The velocity profile is shown in Figure 4.28. The throat velocity was 11.22 m/s. The vapor velocity of the cavitation started around 22.8 m/s and decreased to around 19.0 m/s. The combined vapor velocities are shown in Figure 4.29. All of them had similar results, with a vapor velocity larger than the inlet velocity. As the vapor travelled downstream it decreased by small amounts.

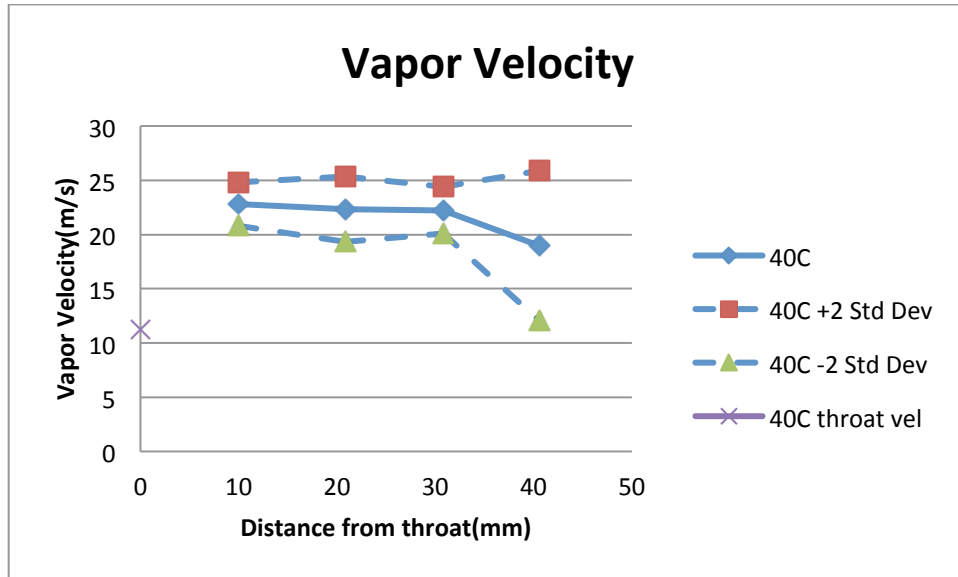


**Figure 4.28 Nozzle 1, 40 °C Vapor Velocity.**

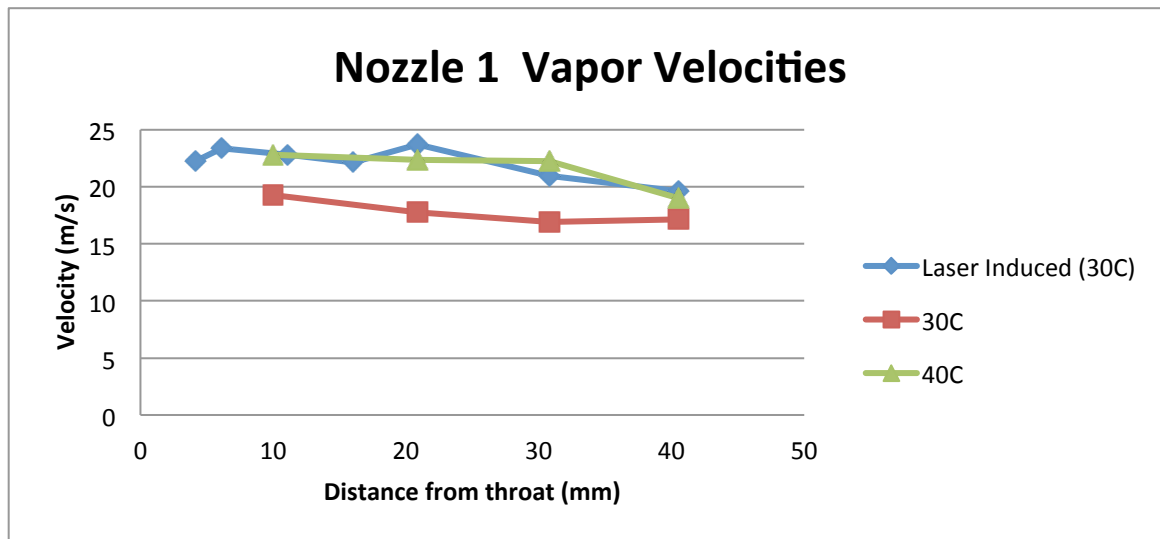


**Figure 4.29 Nozzle 1, Combined Vapor Velocities.**

### 4.2.3 Nozzle 2

Vapor velocity measurements were taken at three different mass flow rates using Nozzle 2. Sample images are shown in Figure 4.16, Figure 4.17, and Figure 4.18 for the test conditions with an inlet temperature 30 C and 48, 85, and 95 g/s respectively. These are the same set of images used for the void fraction calculations. In all of the flow conditions the vapor velocity was larger than the inlet velocity. The vapor velocity remained fairly constant throughout the



nozzle. There was a direct correlation between the mass flow rate and the vapor velocity, an increase in the mass flow rate increased the vapor velocity.

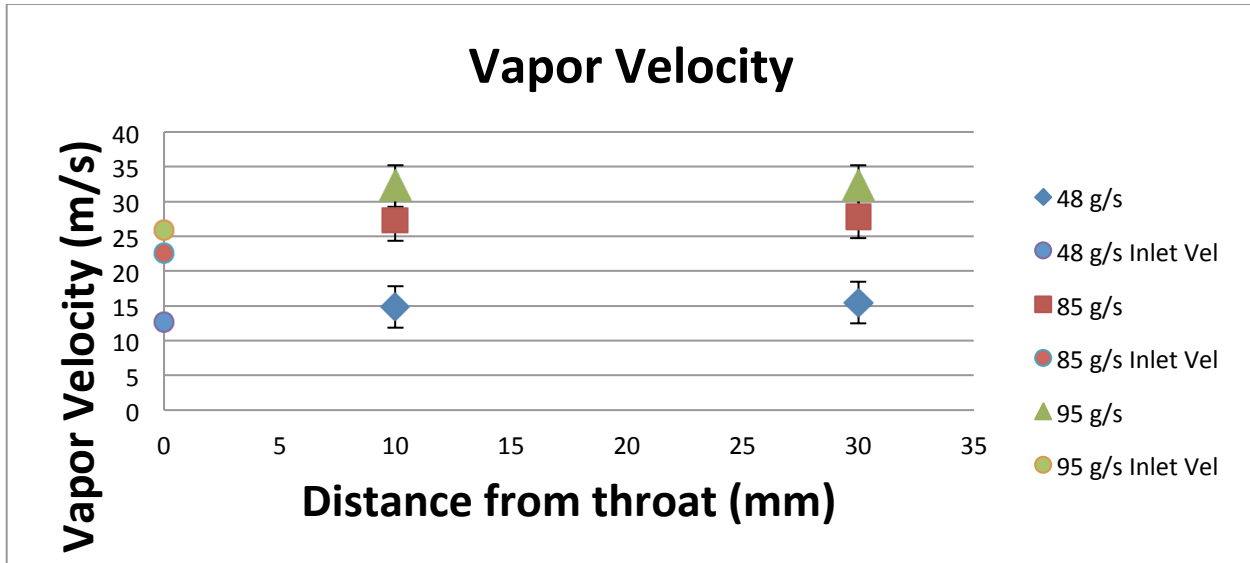


Figure 4.30 Nozzle 2, Combined Vapor Velocities.

### 4.3 Flow Quality

The quality of a fluid mixture is the ratio of the mass of the vapor divided by the total mass of the fluid. Equation 4.1 is a simple energy balance that assumes that the heat to turn the liquid into vapor comes from the remaining liquid. The energy required by the vapor is the mass flow rate of the vapor multiplied by the latent heat of vaporization. The energy provided by the surrounding liquid is the mass flow rate of the liquid multiplied by the specific energy and the temperature difference. In order to have a significant temperature drop, there has to be a significant mass flow rate of vapor, which is signified by a significant flow quality.

$$\dot{m}_v L = \dot{m}_l c_{pl} \Delta T \quad (4.1)$$

Calculating the quality in a static system is a fairly straight forward proposition. In a closed system, with known densities of the liquid and gas, the volumetric fraction is easily converted to the mass fraction, or quality. However, in an open system the two phases can be traveling at different velocities, complicating the flow quality calculations. Equations 4.2- 4.5 shows the basic calculations involved in the measurement of flow quality. The variables  $\dot{m}$ ,  $x$ ,  $\rho$ ,  $v$  and  $\alpha$  are

the mass flow rate, flow quality, density, velocity, and void fraction respectively. The subscripts  $l$ ,  $v$ , and  $t$  are used for liquid, vapor, and total. The combination of the mass flow rate of the liquid and the mass flow rate of the velocity must equal the total mass flow rate. The flow quality can be solved using either the mass of the vapor or the mass of the liquid. The velocity was measured from the surface features on the liquid-vapor boundary, and it was assumed that this was the void velocity. Therefore, the flow quality was measured using the approximate mass flow rate of the vapor. The total mass flow rate was measured by the mass flow sensor. The density was a function of the inlet temperature. The vapor velocity and void fraction were calculated through the methods described in the previous chapters. The cross sectional area at the measurement location was calculated using the diameter at the middle of the image field.

$$\dot{m}_t = \dot{m}_l + \dot{m}_v \quad (4.2)$$

$$\dot{m}_v = x\dot{m}_t = \rho_v v_v A_v = \rho_v v_v \alpha A_t \quad (4.3)$$

$$\dot{m}_l = (1 - x)\dot{m}_t = \rho_l v_l A_l = \rho_l v_l (1 - \alpha) A_t \quad (4.4)$$

$$\therefore x = \frac{\dot{m}_v}{\dot{m}_t} = \frac{\rho_v v_v \alpha A_t}{\dot{m}_t} \quad (4.5)$$

#### 4.3.1 Nozzle 1

The flow quality was measured in Nozzle 1 using the data from image set 2. The conditions used were laser induced cavitation 30 °C and 40 °C. The sample of images is shown in Figure 4.11 and Figure 4.12. The results of the void fraction for image set 2 are shown in Figure 4.13. The results of the vapor velocity are shown in Figure 4.29, where the two profiles were nearly identical. Figure 4.31 shows the results of the flow quality. As both the void fraction and the velocity were nearly identical up to 30 mm downstream from the throat, the flow quality results were nearly identical up to that point. The laser induced cavitation 30 °C case had a recirculation region that drastically lowered the void fraction, thus lowered the flow quality. The key result of this is that the flow quality never reached  $10 \times 10^{-5}$  (.01%), so very little of the fluid was turned into vapor. This negligible mass of vapor will result in a negligible temperature drop.

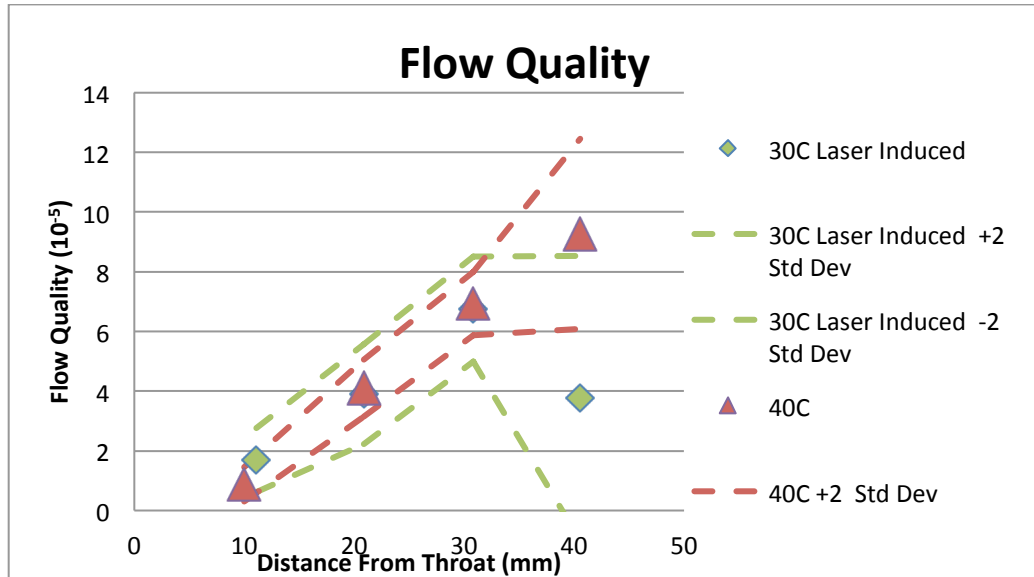


**Figure 4.31 Nozzle 1, Flow Quality Results.**

#### **4.3.2 Nozzle 2**

The data for the flow quality for Nozzle 2 are from the images found in Figure 4.16, Figure 4.17, and Figure 4.18 for the 48, 85, and 95 g/s flow conditions. The void fraction profile is shown in Figure 4.20 with the velocity profile in Figure 4.30. The flow quality is shown in Figure 4.32. For formulation, the velocities found from 0-20 mm and from 20-40 mm represent averages around their respective zones. For these conditions, the void fractions were similar, while the velocities were different. However, the increase in measured velocities was a result of an increase of the mass flow rate. Therefore, the measured flow qualities were nearly identical and did not exceed  $2 \times 10^{-5}$  (.002%). This nozzle also had a negligible flow quality, thus would have negligible temperature drop.

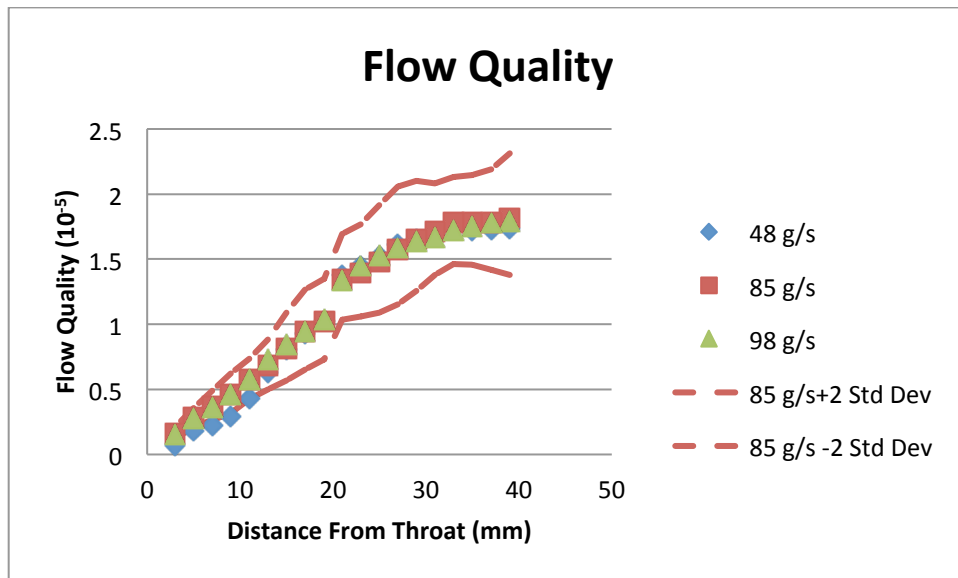


**Figure 4.32 Nozzle 2, Flow Quality Results**

## **Chapter 5 - Flow Visualization Summary, Conclusion, and Recommendations**

### **5.1 Summary and Conclusions**

All of the tests during this research involved water, temperatures between 30-50 °C, inlet pressure 50 psia or lower, and with nozzles that had a throat diameter between 2 and 4mm. The flows described in this paper have been categorized and studied with the intention of providing a basis to predict the cavitation flow structure of these nozzles.

The cavitation flows were categorized into five categories: attached, shear, mixed, swirl, and travelling bubble cavitation. Attached wall cavitation typically occurred in venturi nozzles, although it also occurred with the ogive to constant diameter nozzle. These nozzles all had a small expansion angle. Attached wall cavitation typically nucleated downstream of the minimum area throat, most likely where a separation region developed. This cavitation started attached to the wall and laminar. As it flowed downstream it detached from the wall, became turbulent, and the void fraction grew.

How the cavitation formed in attached wall cavitation was dependent on one of two things: the presence of nuclei, or the separation region. The presence of nuclei was the dominant variable, whether the nuclei were in the water, travelling bubble cavitation, or on the surface, Nozzle 1 and Nozzle 4. While there were exceptions, the travelling bubble cavitation suppressed the attached wall cavitation. With certain flow conditions, the discontinuity on the surface of Nozzle 1 suppressed any other cavitation. The small scratch on Nozzle 4 did not suppress all other cavitation, although it suppressed it in the area surrounding it. When no nuclei were present the separation region dictated where the cavitation formed.

In shear cavitation, an orifice jet, a turbulent mixture of liquid and vapor, formed from the water flowing through a rapid expansion. The shear forces from the orifice jet and the surrounding water caused vapor to form, called shear cavitation. The shear cavitation was affected by the inlet to the throat. In the nozzles with a converging inlet, the vapor cloud developed a cyclical pattern of forming and collapsing around the orifice jet. In the nozzles with a constant diameter inlet, the vapor cloud permanently developed around the orifice jet.

When the expansion angle was small near the throat and then increased downstream, mixed cavitation formed. At the low expansion angles attached wall cavitation formed, however,

at larger expansion angles the flow turned into shear cavitation. In Nozzle 5, with a rapid expansion, a new cavitation was observed by rotating the flow prior to entering this nozzle. This was swirl cavitation, where the orifice jet expanded outwards, turning to vapor. Travelling bubble cavitation was formed when there were entrained gasses in the water. These gasses were nuclei, causing vapor to form on these gasses.

The results of measuring the void fraction and the velocity were similar for both of the glass venturi nozzles. Once the cavitation initiated, the void fraction increased. The velocity measurements showed that the features on the liquid-vapor interface, assumed to be vapor velocity, were higher than the velocity of the liquid at the throat. In Nozzle 1 the vapor velocity decreased slightly downstream, where as in Nozzle 2 the vapor velocity remained fairly constant. Out of all of the measurements, the highest quality was .01%, which was simply too small to create a drop in the temperature.

## **5.2 Recommendations and Future Work**

### ***5.2.1 Cavitation***

Now that the fundamentals of cavitation formation have been explored, the direction of research can now be directed toward achieving cooling. To achieve cooling, two objectives are considered: a measurable temperature drop and a large overall heat transfer rate. The first objective is to create a measurable temperature drop, which can only come by increasing the flow quality. Water requires a very high void fraction to result in a significant flow quality. In the quantitative results from Nozzle 1, at 40 °C, the void fraction increased to 50%, which only resulted in a .01% flow quality. The only cavitation that was observed to have a large void fraction was the swirl cavitation, using Nozzle 5 and the IFM. However, in the first half of the nozzle there was stagnant vapor around the cavitation, which would not be conducive for the second objective, heat transfer. The nozzle geometry could be explored further to minimize the stagnant vapor around the swirl cavitation while not affecting the cavitation itself.

In addition to the nozzle geometry, there are other possible ways to change the cavitation. It might be possible to add acoustic cavitation to induce nucleation sites. These nucleation sites could result in a higher void fraction. Another change to the system could be changing how the flow is driven. In the research by Sato, Hachino, and Saito [5], they observed travelling bubble cavitation, sheet cavitation (attached wall cavitation), and a transition between the two. These

types of cavitation are similar to the cavitation on the hydrofoil by Frac [2]. However, the dissertation by Davis [4] showed cavitation that was not similar to the attached wall cavitation. This could be a result of how the fluid was driven. In the Sat, Hachino, and Saito research the fluid is driven by a pump, while in the Davis dissertation the fluid was driven by decreasing the outlet pressure in a blow down system. Therefore, the effects of how the fluid is driven could be explored.

### ***5.2.2 Measurement Method***

Overall the technique for finding the void fraction is effective. The main issue is that the vertical laser sheet method only captures the middle of nozzle, not a true cross sectional area. The tilted laser sheet works to resolve this issue, however the images generally were blurry and difficult to analyze. There are two possible reasons for this. The first is that the laser light sheet is too thick, distorting the view. To solve this issue, the laser light sheet can be adjusted to be as thin as possible. The second reason is that, due to the cylindrical nature of the nozzle, the laser light gets refracted around. By using an index matching fluid the outer wall of the nozzle will not bend the laser light. A simple index matching solution is found in Appendix C.

There is another method for finding velocity, Particle Image Velocimetry (PIV). This method uses laser light to illuminate tracer particles, which are then measured to find a velocity field. It has not been used in the research in this thesis due to the concern that the tracer particles would affect the formation of the cavitation. Further research can be performed to examine the effect that tracer particles have on the cavitation. If tracer particles do not affect the cavitation significantly, then the liquid velocities can be measured. If they do influence the cavitation then that effect can be studied.

## References

- [1] S. Charamko, K. Debus and T. Gielda, "Cooling System Utilizing a Reciprocating Piston". United States Patent US 2012/0260673, 18 October 2012.
- [2] J.-P. Franc, "Physics and Control of Cavitation," *Design and Analysis of High Speed Pumps*, pp. 2.1-2.36, 2006.
- [3] E. Goncalves and R. F. Patella, "Numerical Simulation of Cavitating Flows With Homogeneous Models," *Computers & Fluids*, pp. 1682-1696, 2009.
- [4] M. P. Davis, *Experimental Investigation of the Cavitation of Aviation Fuel in a Converging-Diverging Nozzle*, Notre Dame, Indiana: Graduate Program in Aerospace and Mechanical Engineering, 2008.
- [5] K. Sato, K. Hachino and Y. Saito, "Inception and Dynamics of Traveling-Bubble-Type Cavitation in a Venturi," in *Proceedings of ASME FEDSM*, Honolulu, Hawaii, 2003.
- [6] B. Schneider, A. Kosar, C.-J. Kuo, C. Mishra, G. S. Cole, R. P. Scaringe and Y. Peles, "Cavitation Enhanced Heat Transfer in Microchannels," *Journal of Heat Transfer*, vol. 128, 2006.
- [7] A. Sou, S. Hosokawa and A. Tomiyama, "Effects of Cavitation in a Nozzle on Liquid Jet Atomization," *International Journal of Heat and Mass Transfer*, pp. 3575-3582, 2007.
- [8] A. Predin and I. Bilus, "Cavitation Swirl in the Inlet Pipe of the Radial Pump," in *Proceedings of the 2nd IASME/ WSEAS International Conference on Water Resources, Hydraulics & Hydrology*, Portoroz, Slovenia, 2007.
- [9] V. Belova, D. A. Gorin, D. G. Shchukin and H. Mohwald, "Controlled Effect of Ultrasonic Cavitation on Hydrophobic/ Hydrophilic Surfaces," *ACS Applied Material Interfaces*, vol. 3, pp. 417-425, 2011.
- [10] E. Goncalves and R. F. Patella, "Numerical study of cavitating flows with thermodynamic effect," *Computers & Fluids*, pp. 99-113, 2010.



# Appendix A - High Speed Camera

## Specifications

Below are the specifications for the SA-5 Photron High Speed Camera. This camera has the 8 GB option. The camera can run at 7,000 frames per second at its maximum resolution of 1,024 x1,024 pixels. At lower frame rates the camera can run for a much longer time span. At higher levels of frame rates the maximum resolution decreases. In any video the resolution can be set below the maximum resolution, increasing the recording duration.

FRAME RATE (fps)	MAXIMUM RESOLUTION		MAXIMUM SHUTTER SPEED	RECORD DURATION (12-BIT)					
	Horizontal	Vertical		TIME (Sec.)			FRAMES		
				8GB	16GB	32GB	8GB	16GB	32GB
1,000	1,024	1,024	1µs 1/1,000,000 sec	5.46	10.92	21.84	5,457	10,918	21,841
2,000	1,024	1,024		2.73	5.46	10.92	5,457	10,918	21,841
4,000	1,024	1,024		1.36	2.73	5.46	5,457	10,918	21,841
5,000	1,024	1,024		1.09	2.18	4.37	5,457	10,918	21,841
7,000	1,024	1,024		0.78	1.56	3.12	5,457	10,918	21,841
7,500	1,024	1,000		0.75	1.49	2.98	5,588	11,180	22,365
9,300	1,024	800		0.75	1.50	3.01	6,985	13,975	27,956
10,000	1,024	744		0.75	1.50	3.01	7,511	15,027	30,061
15,000	960	528		0.75	1.51	3.01	11,289	22,587	45,182
20,000	832	448		0.77	1.54	3.07	15,352	30,716	61,443
30,000	768	320		0.78	1.55	3.11	23,284	46,586	93,189
50,000	512	272		0.82	1.64	3.29	41,090	82,211	164,452
75,000	320	264		0.90	1.81	3.61	67,737	135,523	271,097
100,000	320	192		0.93	1.86	3.73	93,138	186,345	372,758
150,000	256	144		1.03	2.07	4.14	155,230	310,575	621,264
300,000	256	64		1.16	2.33	4.66	349,269	698,794	1,397,845
420,000	128	64		1.66	3.33	6.66	698,538	1,397,589	2,795,690
525,000	128	48	1.77	3.55	7.10	931,384	1,863,452	3,727,587	
775,000	128	24	2.40	4.81	9.62	1,862,769	3,726,904	7,455,175	
930,000	128	16	369 ns	3.00	6.01	12.02	2,794,154	5,590,357	11,182,762
1,000,000	64	16	1/2,712,000 sec	5.59	11.18	22.37	5,588,309	11,180,714	22,365,525
OPTION SUBJECT TO EXPORT LICENSE CONTROL RESTRICTIONS WHERE APPLICABLE									

<b>Sensor</b>	12-bit ADC (Bayer system color, single sensor) with 20 µm pixel
<b>Shutter</b>	Global electronic shutter from 16.7ms to 1 µs independent of frame rate
<b>Lens Mount</b>	Interchangeable F-mount and C-mount using supplied adapters
<b>Extended</b>	Selectable in twenty steps (0 to 95% in 5%

<b>Event Markers</b>	Ten user entered event markers mark specific events within the image sequence in real time. Immediately accessible through software
<b>Dual Speed Recording</b>	Enables the recording speed to be changed up or down by a factor of 2, 4 or 8 during a recording
<b>Trigger Modes</b>	Start End Center Manual Random

<b>Dynamic Range</b>	increments) to prevent pixel over-exposure		Random Reset, Random Center, Random Manual and Duals Speed Recording
<b>Memory</b>	8GB (standard: 5,457 frames @ maximum resolution)	<b>Saved Image Formats</b>	JPEG, AVI, TIFF, BMP, RAW, PNG, MOV and FTIF. Images can be saved with or without image or comment data
<b>Video Outputs</b>	Live and playback video thorough Dual HD-SDI or single RS-170 (NTSC /PAL) outputs. Ability to zoom, pan and tilt within image via keypad.	<b>Data Display</b>	Frame Rate, Shutter Speed, Trigger Mode, Date or Time, Status (Playback /Record), Real Time, Frame Count and Resolution
<b>Camera Control</b>	Through optional keypad with integrated viewfinder and Gigabit Ethernet or RS-422	<b>Partitioning</b>	Up to 64 memory segments for multiple recording in memory
<b>User Preset Switches</b>	Four user selectable camera function controls mounted on the camera's rear panel	<b>Data Acquisition</b>	Supports Photron MCDL and DAQ
<b>Low Light Mode</b>	Low light mode drops the frame rate and shutter time to their maximum values, while maintaining other set parameters, to enable users to position and focus the camera	<b>Cooling</b>	Actively cooled
<b>Triggering</b>	Selectable positive or negative TTL 5Vp-p or switch closure	<b>Operating Temperature</b>	0 - 40 degrees C (32 - 104 degree F)
<b>Trigger Delay</b>	Programmable delay on selected input and output triggers, 100ns resolution	<b>Mounting</b>	1 x 1/4 - 20 UNC, 1 x 3/8 - 16 UNC, 6 x M6
<b>Timing</b>	Internal clock or external source	<b>Dimensions</b>	165mm (6.50")H×153mm (6.02")W×242.5mm (9.55")D *excluding protrusions
<b>Phase Lock</b>	Enables cameras to be synchronized precisely together to a master camera or external source, such as IRIG/GPS time codes	<b>Weight</b>	6.2 kg (13.67 lbs)
		<b>Power Requirements</b>	100V-240V AC ~ 1.5A, 50-60Hz DC operation 18-36 V DC, 100VA

## First Time Guide to using the Camera

1. Hook up the power to the high speed camera, and the Ethernet cord between the high speed camera and the computer.
2. Set the IP address on the computer to 192.168.000.001, and the subnet mask to 255.255.255.000 (the computer should automatically fill in the subnet mask). To learn how to do this, read the document: "GigabitEthernet Interface Connection Manual".
3. Turn on the High Speed Camera. Once the "IF LINK/TRANS" light turns on, the camera should be communicating with the computer.
4. Activate the PFV software. The default setting for the software is to automatically open the camera. If a view area appears, but is black, the camera is operating; however, it is not focused on an area with sufficient light. If no view area appears there is a problem between the camera and the computer. Here is a list of known errors and solutions:
  - a. The firewall is blocking the connection. Either temporarily disable the firewall, or add PFV as an exception.
  - b. The IP connection is incorrect. Set the correct one and restart application.

- c. A larger packet size is selected in the auto selection. In PFV go to configuration-> network configuration setup -> Start with the Safety Size. If the safety size selection fixes the problem, go through the manually selected sizes to get the maximum packet size. This issue has been observed specifically in HP laptops.
- 5. When using the software, the 'camera' tab on the right hand side allows you to select the setting on the camera for your video. Once the video is captured, through the 'record' button, the 'data save' tab is used to save the image. The playback box, in the lower right corner, the image can be cut to the desired size. Previous clips can be manipulated using the 'file view' tab.
- 6. When done, close the PFV application. Once the application has shut down it is safe to turn off the camera.
- 7. For expand use, there are four manuals:
  - a. Photron FASTCAM Viewer User's Manual
  - b. FASTCAM SA5 Hardware Manual
  - c. Gigabit Ethernet Interface
  - d. Remote Controller with LCD User's Manual

## Appendix B - Matlab Code

### Void Fraction Code

The scrip file for the void fraction reads in a sequence of images. In the script file the inputs are the name of the image, name of the no flow image, the distance from the throat to the top and bottom of the image (mm), the threshold value, and how many sections the image will be broken into. The script file then runs a for loop, sending every image file through the function, and then saving a new copy of the black and white image. The function takes in the data from the script file and then splits the image into the individual sections. The for loop takes each section and converts that section image from grayscale into binary and finds the void fraction. The if statement was created to find the distance from the throat to the top and bottom of the section (mm). At the end, the function saves all of the void fraction data for the sections in “percent”, and saves the average distance each section is from the throat “distance”. The script then saves the distance, and compiles all of the void fraction data onto one matrix “tpercent”.

#### Script file:

```
I = imread('image_01.bmp');
p = which('image_01.bmp');
filelist = dir([fileparts(p) filesep 'image_*.bmp']);
fileNames = {filelist.name}';

I = imread(fileNames{1});
[mrows, ncols] = size(I);
nImages = length(fileNames);

VoidSequence = zeros(mrows,ncols,nImages,class(I));

lower = 30; % input for distance from the throat
upper = 31.6128;

thresh = 100 /255; % defining the threshold for the images processed
sections = 4; % defining the number of sections to split the image into
noflow = imread('image_noflow.bmp');

for k = 1:nImages
    Void1 = imread(fileNames{k});
    [bw1,bwnoflow,percent,distance] =
voidfunctII(Void1,noflow,thresh,sections,lower,upper);
    filename3=(['image2_(k)',num2str(k),'.bmp']);
    imwrite(bw1,filename3);
    tpercent(k,:)=percent;
    distance;
```

end

### Function code:

```
function [bw1,bwnoflow,percent,distance] =  
voidfunctII(imagel,noflow,thresh,sections,lower,upper)  
  
totaldistp = 0;  
threshno=150/255; % defines thresh for no flow image  
bw1 = im2bw(imagel,thresh);  
bwnoflow = im2bw(noflow,threshno);  
[mrows,ncols] = size(bw1);  
se = (mrows+1)/sections;  
  
ser = fix(se)-1;  
totalbw = bwarea(bw1);  
totalbwno = bwarea(bwnoflow);  
mp = (upper-lower)/mrows; %finds distance in mm per pixel  
  
percent = zeros(1,sections);  
distance = zeros(1,sections);  
  
for n = 0:sections-1  
    m= n+1;  
    sen = fix(se*m);  
  
    if m == 1  
        imageflow = imcrop(bw1,[0 0 ncols ser]);  
        imagenoflow = imcrop(bwnoflow,[0 0 ncols ser]);  
  
        endpoint = 0 +ser;  
        ser = ser+1;  
        distp = ser;  
  
    elseif m == sections  
        final = mrows-ser;  
  
        imageflow = imcrop(bw1,[0 ser ncols final]);  
        imagenoflow = imcrop(bwnoflow,[0 ser ncols final]);  
  
        distp = final;  
        endpoint = ser +final;  
    else  
  
        change = sen - ser;  
        imageflow = imcrop(bw1,[0 ser ncols change]);
```

```

        imagenoflow = imcrop(bwnoflow,[0 ser ncols change]);
        endpoint = ser + change;
        distp = change;
        ser = ser+change+1;

end
averagedistp = (distp)/2;
averagedistp = fix(averagedistp);
locationp = endpoint-averagedistp;
locationp = mrows- locationp;
locationmabs = locationp*mp +lower;

totalbw1 = bwarea(imageflow);
totalbwno1 = bwarea(imagenoflow);
perc = 1 - totalbw1/totalbwno1;
compare(m) = bwarea(imageflow);
percent(1,m) =perc;
distance(1,m) =locationmabs;

end

percent;
distance;
compare= sum(compare);

```

## Velocity Code:

This code reads in two images (they need to be sequential). The two images can then be cropped. The line “sum(image1')'” creates a 1 by x matrix, where x is the number of vertical pixels, where the value in the matrix is the sum of the horizontal pixel values. The CentralizedImage variables take the image minus the mean value of the image. This creates two images with the same overall intensity. The function “xcorr” is a linear correlation function found in the signal processing toolbox of Matlab. The correlation is then graphed.

```

clear

image1 = imread('region1_27.bmp');
image2 = imread('region1_28.bmp');

image1 =image1(:,100:200); % carve slice
image2 =image2(:,100:200);

figure, imshow(image1);
figure, imshow(image2);

```

```

image1=sum(image1')';
image2=sum(image2')';

[vsize hsize]=size(image1);

CentralizedImage1=image1-mean(image1);
CentralizedImage2=image2-mean(image2);

[XC,lags]=xcorr(CentralizedImage1,CentralizedImage2,'coeff');
figure,plot(lags,XC); grid; title('correlation coefficients')

[peak loc]=max(XC);
lags(loc)

```

## **Appendix C - Measurement Instrument Specifications**

The water testing rig, shown in Figure 2.1, used a mass flow sensor, two pressure transducers, and a thermocouple. The mass flow sensor, P1, and T1 measured the inlet conditions are referenced in this paper. Before every experiment a vacuum pump decreased the pressure (to the vapor pressure of water) in the water testing rig. P2 was used to measure this pressure.

### **Mass Flow Sensor**

- Micro Motion Coriolis Flow Meter (CMF025)
- Range: 5 g/cm<sup>3</sup> to 5000 kg/m<sup>3</sup>
- Accuracy:  $\pm 0.10\%$  of rate
- Repeatability:  $\pm 0.05\%$  of rate

### **Pressure Transducer (P1)**

- Setra 280E Pressure Transducer
- Range: 0-100 psia
- Accuracy:  $\pm 0.11\%$  FS

### **Pressure Transducer (P2)**

- OmegaDyne Inc FX309-005A5V Pressure Transducer
- Range: 0-5 psia
- Accuracy: 0.25% FS

### **Thermocouple (T1)**

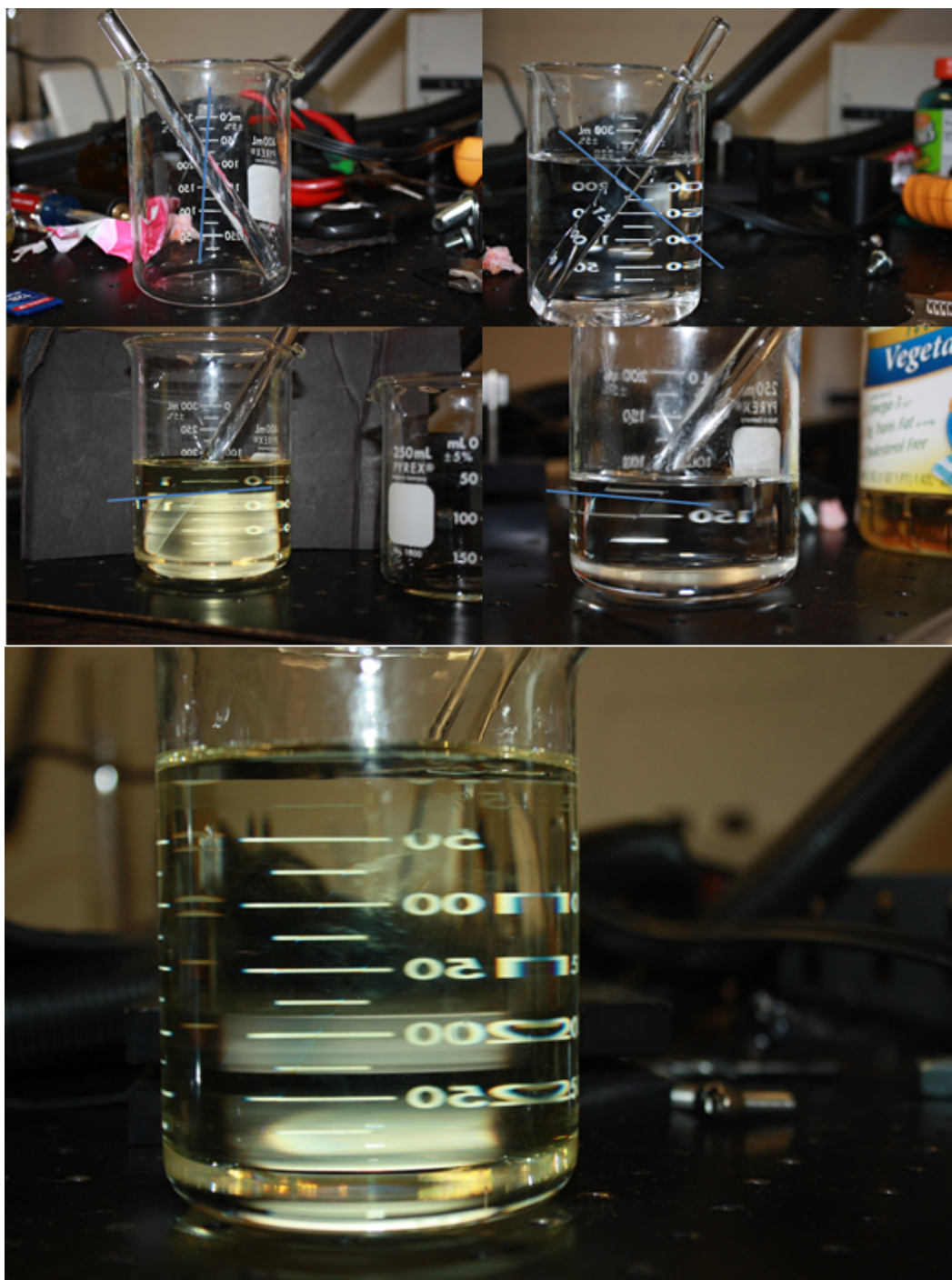
- Omega Thermocouple Type K
- Range: -200 to 1250 °C
- Accuracy: above 0 °C- 0.75%; below 0 °C – 2.0%



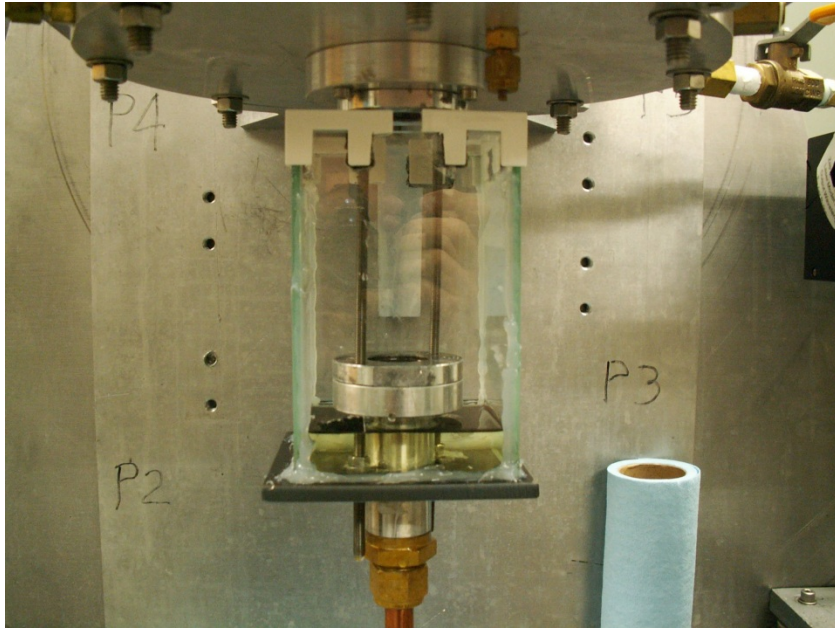
## **Appendix D - Index Matching**

Figure D.1 shows the effects of differing fluids on the refraction of light through a beaker with a Pyrex rod in the middle. The purpose of this is to create a fluid that matches the index of refraction of the rod, which was the same material as the nozzle. The first image was with no liquid in the beaker. This resulted in the horizontal lines on the beaker being bent into nearly vertical lines. With water, the lines are still bent, although they are closer to a 45 degree angle. Water and air both have an index of refraction lower than the Pyrex. The baby oil and the vegetable oil show that the baby oil had a slightly lower index of refraction, while the vegetable oil has a slightly larger index of refraction than the Pyrex. By mixing the two fluids a mix was achieved to essentially make the rod optically disappear. This mix was four parts vegetable oil, one part baby oil. The reason that these two materials were used was that they are able to mix into a homogeneous solution, as opposed to mixing a water based product with an oil based product.

The containment, shown in Figure D.2, was designed to simply be a metal base supporting four glass rectangles. The white corner pieces held the glass in place while silicone sealant was applied. The oil is applied through the top of the container and there is a screw on the bottom to drain it. The sealant took about 4 hours to dry, leaks would only be apparent after applying the oil, and leaks could only be patched once the hole was dried. This resulted in a process that was only beneficial when studying a single nozzle intensively.



**Figure D.1 Index Matching fluids. These images have a pyrex rod inside of a cylinder. Top Row, Left: Air; Top Row, Right: Water; Middle Row, Left: Vegetable Oil; Middle Row, Right: Baby Oil; Bottom Row: 200ml vegetable oil, 150ml baby oil.**



**Figure D.2 Containment for the fluid.**